SEISMIC REHABILITATION OF COLUMN TO PIER CAP ACCELERATED BRIDGE CONSTRUCTION CONNECTIONS AND ACOUSTIC EMISSION MONITORING ASSESSMENT

by

Joel Edgar Parks

A thesis submitted to the faculty of
The University of Utah
in partial fulfillment of the requirements for the degree of

Master of Science

Department of Civil and Environmental Engineering

The University of Utah

May 2014

The University of Utah Graduate School

STATEMENT OF THESIS APPROVAL

The following faculty members served as the supervisory committee chair and members for the thesis of **Joel Edgar Parks**.

Dates at right indicate the members' approval of the thesis.

Chris Pantelides, Chair	**11/26/13** Date Approved
Luis Ibarra, Member	**11/26/13** Date Approved
Lawrence D. Reaveley, Member	**11/26/13** Date Approved

The thesis has also been approved by **Michael Barber**

Chair of the Department/School/College of Civil and Environmental Engineering

and by David B. Kieda, Dean of The Graduate School.

ABSTRACT

A repair technique for damaged precast reinforced concrete bridge column to pier cap joints constructed with grouted splice sleeve connections has been developed using plastic hinge relocation. Undamaged column to pier cap specimens constructed with grouted splice sleeve connections were tested to failure using quasi-static cyclic loads applied in the horizontal direction at the top of the column. The column's plastic hinge region was subsequently repaired using prefabricated carbon fiber-reinforced polymer shells, epoxy anchored headed mild steel bars, and nonshrink or expansive concrete to increase the moment of inertia at the column base and relocate the plastic hinge in the column to a region with minor damage. Follow up quasi-static cyclic tests of the repaired specimens were performed to verify the effectiveness of the repair technique. Analytical strut and tie models of both the original and repaired specimens were developed and verified using the test results.

In addition to destructive tests, acoustic emission monitoring of grouted splice sleeves, the original specimens, and the repaired specimens were performed to correlate acoustic emissions to damage. To obtain an appropriate damage assessment of grouted splice sleeve connections using acoustic emissions monitoring, the acoustic emission characteristics of two different grouted splice sleeve systems were obtained by performing tension tests of the sleeves to failure. The acoustic emission monitoring system was then implemented on the original and repaired specimens to demonstrate the effectiveness of relating acoustic emissions to damage.

TABLE OF CONTENTS

CHAPTER 1

INTRODUCTION

Repair of damaged bridge elements following an earthquake is a beneficial alternative to replacement of the damaged members. The benefits include cost savings, reduction in construction time, and decreased interruption for emergency services and the general public. The objective of bridge repair is to rehabilitate the damaged bridge elements to a performance level similar to the original performance by restoring strength and displacement capacity. Due to the current bridge design philosophy, which protects the superstructure and allows repairable damage to occur at the columns, the postseismic repair studied is focused on column repair. In the past, repair techniques for damaged bridge columns included the use of externally bonded carbon fiber reinforced polymer (CFRP) sheets (*1*), steel jacketing (*2*), and concrete jacketing (*3*). However, until recently it has been assumed that when longitudinal bars within the column buckle or fracture, the column must be replaced (*4*).

Accelerated Bridge Construction (ABC) is gaining acceptance because of reduced construction time and minimal traffic interruption. Recently, grouted splice sleeves have gained attention as a possible precast concrete connection method for ABC in seismic regions. Research is currently being conducted to investigate the performance of grouted splice sleeve connections for bridges built in moderate to high seismic regions (*5*,*6*). The use of grouted splice sleeve connections in seismic regions is anticipated and a practical postearthquake repair is needed to accompany this technology. Findings from this research indicate that columns connected using grouted splice sleeve connections concentrate the column damage and decrease the effective plastic hinge length compared to traditional monolithic construction. Both of these damage characteristics are advantageous for repair purposes, leaving a relatively undamaged column

above the plastic hinge. The repair uses materials that are readily available and easy to install including epoxy anchored headed bars, CFRP shells, and nonshrink or expansive concrete. The result is a very cost effective and rapid repair procedure, which could be completed in a few days.

To improve future designs of the repair as well as gain a better understanding of the load paths within the repaired region, strut and tie models of both the original and repaired specimens were developed. The strut and tie models are compared to test results in order to verify their accuracy.

A structural health monitoring system using acoustic emissions (AE) was used to monitor specimens during testing in order to evaluate the damage. AE monitoring has not been used on bridge elements that use grouted splice sleeve connections, but it has shown an ability to monitor the health of various bridge elements (*7*,*8*). In order to get an appropriate damage assessment of the grouted splice sleeve connections using AE, the AE characteristics of the grouted splice sleeves are needed. To obtain these characteristics, two different grouted splice sleeve systems were tested to failure in tension while being monitored by an AE monitoring system. An AE monitoring assessment was then performed on both splice sleeve systems to determine any AE characteristics which could be related to the damage state of the grouted splice sleeves.

The AE monitoring system was then implemented on the repair as well as two precast reinforced concrete (RC) bridge column specimens with different grouted splice sleeve systems subjected to quasi-static cyclic loading. An AE monitoring assessment was then performed on both the RC column and the repaired specimens in an attempt to correlate AE with damage in the column.

1.1 Literature Review

1.1.1 Repair of Column Plastic Hinges

The basic concepts behind plastic hinge relocation for new RC construction have been around for some time (*9*,*10*). It was not until recently, however, that the concept of plastic hinge relocation was used to repair severely damaged bridge columns. Rutledge et al. studied the use of plastic hinge relocation to repair circular RC columns which had bucked or fractured bars (*4*).

In their research, they used carbon fiber sheets that were oriented in the vertical and horizontal direction to confine the original plastic hinge. Postinstalled carbon fiber anchors were then installed which were embedded into the footing and developed onto the vertical carbon fiber sheets to increase the moment capacity of the original plastic hinge region, relocating the plastic hinge up the column to a section that remained essentially elastic. Also in one of their experiments, they added additional transverse layers of carbon fiber sheets to the section just above the repair in an attempt to increase the deformation capacity of that section. This attempt was unsuccessful at relocating the plastic hinge since the additional carbon fiber layers increased the strength of the new plastic hinge so much that a carbon fiber anchor failed before the new plastic hinge could form.

While there is no existing literature on strut and tie models for the repair procedure developed, there is literature for different components of the repair. Hong et al. developed a strut and tie model for the development of headed bars in exterior beam-column joints (*11*), Lehman et al. developed a strut and tie model for a repair procedure that idealized the force transfer mechanism of a RC jacket (*12*), and Xiao et al. developed a strut and tie model that showed the force resisting mechanisms of a retrofitted footing at the column flexural strength (*13*).

1.1.2 Acoustic Emission Monitoring

AE monitoring of RC elements has been investigated in the past, but most authors focus on just one material or a single element (i.e., beams) (*14*, *15*). Very little research has been done on beam to column assemblies. Benavent-Climent et al. performed an AE monitoring damage assessment of a RC exterior beam-column subassembly which was subjected to cyclic loading (*16*). In their research, they found that in monolithic construction of beam column joints, AE monitoring was very effective for assessing the damage of the joint and that the hysteretic strain energy was strongly correlated to the AE energy. Based on these findings, a tentative formula was proposed for predicting the level of damage and the closeness to failure of the connection.

1.2 Grouted Splice Sleeve Descriptions

1.2.1 NMB Splice Sleeve

NMB splice sleeves were provided by Splice Sleeve North America, Incorporated. This sleeve type is used to splice mild steel bars and is grouted with Nissco SS Mortar at both ends. The size of the splice sleeve is determined by the size of bar being spliced. Since #8 bars (1 in. diameter) are being spliced, an 8U-X type NMB splice sleeve was used. A drawing showing the dimensions of the splice sleeve along with a photograph of the sleeve is shown in Figure 1.

1.2.2 Lenton Interlock Splice Sleeve

Lenton Interlock splice sleeves were provided by Erico for these tests. The Lenton Interlock splice sleeves use a threaded bar to fasten it on one end of the splice sleeve while the other bar is grouted with HY10L grout at the other end. Like the NMB Splice Sleeves, the size of the splice sleeve is also determined by the size of bar being spliced. Since #8 (1 in. diameter) bars are being spliced, an LK8 type splice sleeve was used. A drawing showing the dimensions of the splice sleeve along with a photograph of the sleeve is shown in Figure 2.

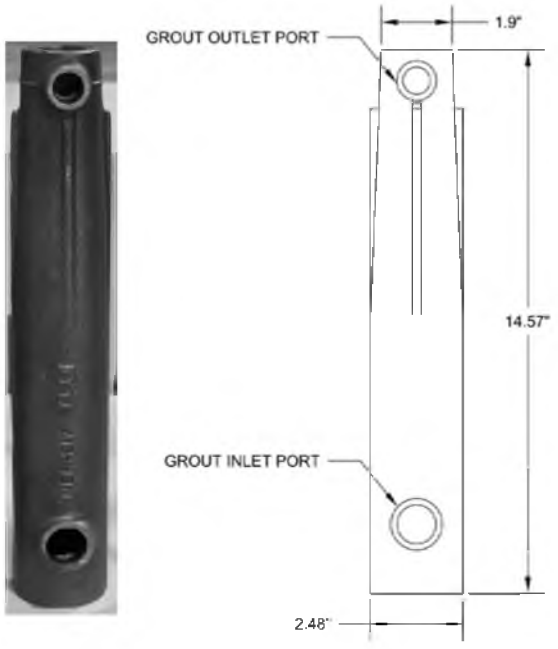

Figure 1. NMB Splice Sleeve

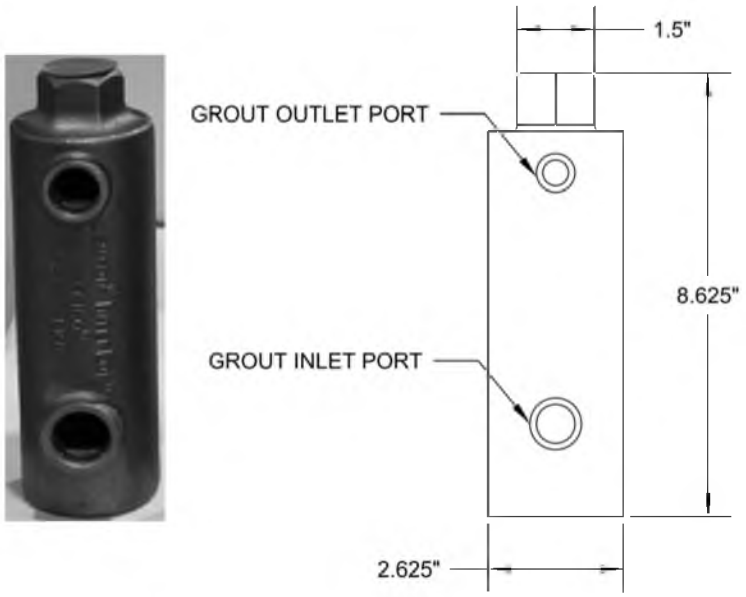

Figure 2. Lenton Interlock Splice Sleeve

1.3 Acoustic Emission Background

Acoustic emission (AE) monitoring is a nondestructive testing technique which uses sensors that detect transient elastic waves produced by a rapid redistribution of stress in a material. AE sensors are transducers that convert the mechanical waves in a material into electrical signals. Thus, information about the existence and location of possible damage sources is obtained. This is similar to seismicity, where seismic waves reach a station placed on the earth's surface.

In the tests being performed, these waves were generated by cracking, plastic deformations, friction due to aggregate interlock, and deboning of aggregate and mortar (15). Figure 3 shows a wave that corresponds to one AE event and the recorded wave's characteristics. For a wave to be recorded as an event, the amplitude of the wave has to be larger than the threshold. The energy of the event is calculated as the area above the threshold and the envelope of the wave. This value is given in ue (energy units; 1ue = ln(Volts*seconds)), where "ln" is the natural logarithm. The Appendix gives an overview of the AE system used for this research.

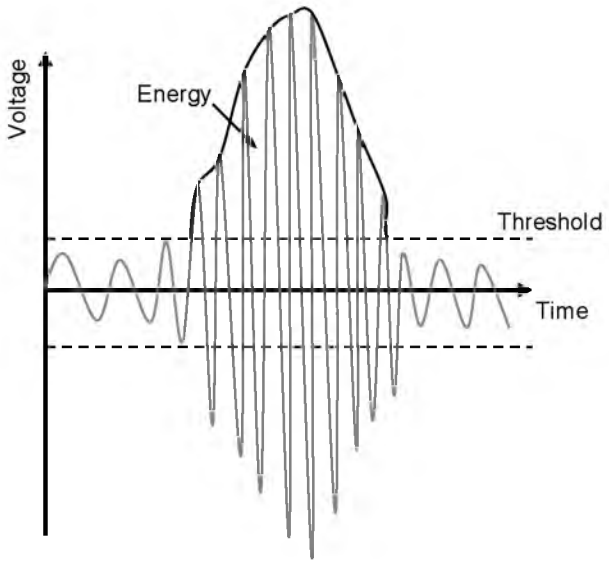

Figure 3. AE Event and Characteristics

CHAPTER 2

GROUTED SPLICE SLEEVE TENSION TEST

To appropriately assess the damage of grouted splice sleeve connections using acoustic emissions, the AE characteristics of the grouted splice sleeves is needed. To obtain these characteristics, two different grouted splice sleeve systems, NMB and Lenton Interlock, were tested to failure in tension while being monitored with AE sensors located at the top and bottom of the sleeve. An AE monitoring assessment is then performed on both splice sleeve systems to determine any AE characteristics which could be correlated to the damage state of the grouted splice sleeves.

2.1 Grouted Splice Sleeve Tension Test Setup

2.1.1 NMB Splice Sleeve Setup

2.1.1.1 NMB Test Specimen Dimensions

To determine the bar length to be spliced, the NMB Splice Sleeve System User's Manual along with ASTM Standards were used. The NMB Splice Sleeve System User's Manual specifies the minimum and maximum lengths for the factory dowel, length of bar inside the narrow end of the sleeve, and the field dowel, length of bar inside the wide end of the sleeve. The factory dowel is required to have a minimum length of 6.5 in. and a maximum length of 6.69 in. While assembling the splice sleeves, the factory dowel bars were inserted all the way to the rebar stop in the sleeve to achieve the maximum length of 6.69 in., as shown in Figure 4.

The field dowel has a larger range of allowable lengths with a minimum length of 6.5 in. and a maximum length of 7.5 in. For the testing of the splice sleeves, it was decided to use the average dowel length of 7 in. shown in Figure 4.

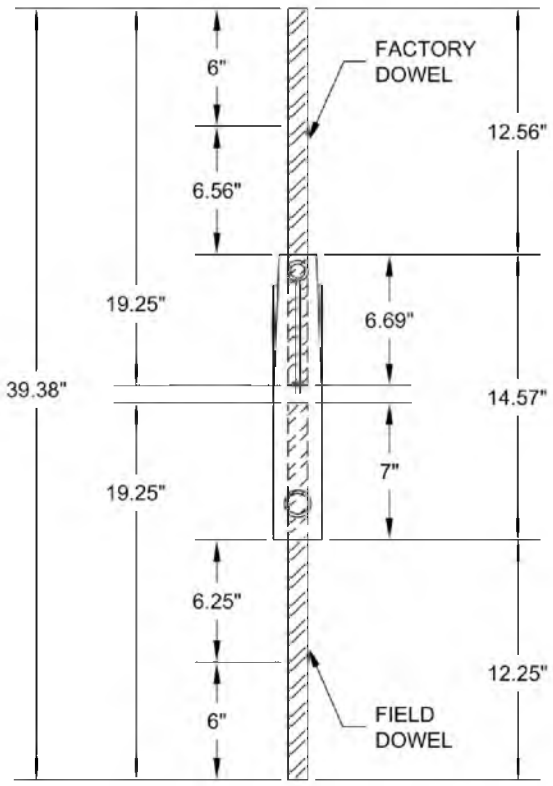

Figure 4. NMB Splice Sleeve Dimensions

The total length of the bars was determined so that there would be enough length to satisfy the dowel length requirements, allow 6 in. to grip the bar, and leave enough free length to allow the bar to strain properly. According to ASTM A370-09a (17), the free length needed between the grips to allow the bar to strain properly is 12 in. for a #8 bar. From these criteria, a bar length of 19.25 in. was chosen which left a free length between the sleeve and grips of 6.25 in. on the field dowel side and 6.56 in. on the factory dowel side.

2.1.1.2 NMB Construction Apparatus

To minimize eccentric loading during the tension tests, a wooden apparatus was constructed to center the bars in the sleeve and keep them as close to vertical as possible. The wooden apparatus is shown in Figure 5 with the NMB splice sleeves in place.

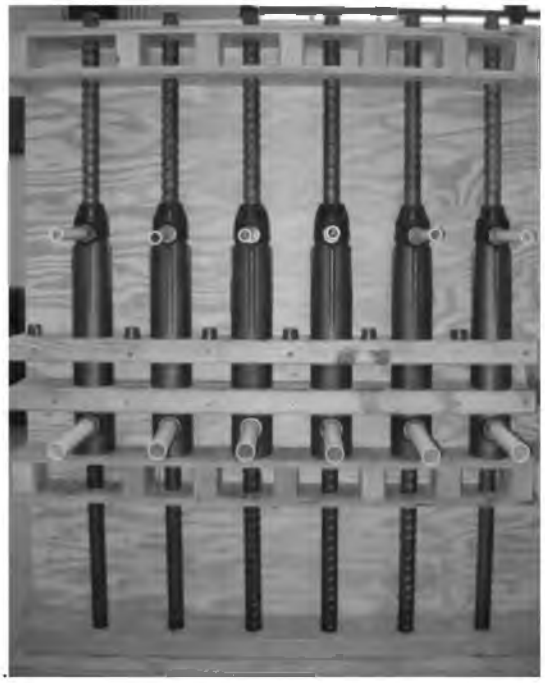

Figure 5. Wooden Construction Apparatus NMB

2.1.1.3 Mixing of Nissco SS Mortar

With the splice sleeves secured in the construction apparatus, Nissco SS Mortar was mixed. Nissco SS Mortar is a nonmetallic, nonshrink, high strength grout used for the NMB splice sleeve system.

Before adding the dry grout, 0.98 gallons of potable water was added to a metal 5 gallon bucket. With the water in the 5 gallon bucket, one 55 lb bag of grout was gradually added while mixing. To mix the grout, an electric mixer was used along with a jiffler type mixing paddle, which is recommended by the manufacturer. A picture of the electric mixer and mixing paddle is shown in Figure 6. After adding all the grout to the 5 gallon bucket, the grout was mixed thoroughly for an additional 2.5 minutes.

Once mixed, a flow test was performed following the procedure described in the NMB Splice Sleeve System User's Manual. This test is performed to confirm that consistency of the grout is correct. The final diameter of the grout puddle after the test should fall between 6 in. and 9.25 in. The result from the flow test of the mixed grout is shown in Figure 7 with an acceptable puddle diameter of 6.5 in.

Figure 6. Electric Mixer and Mixing Paddle

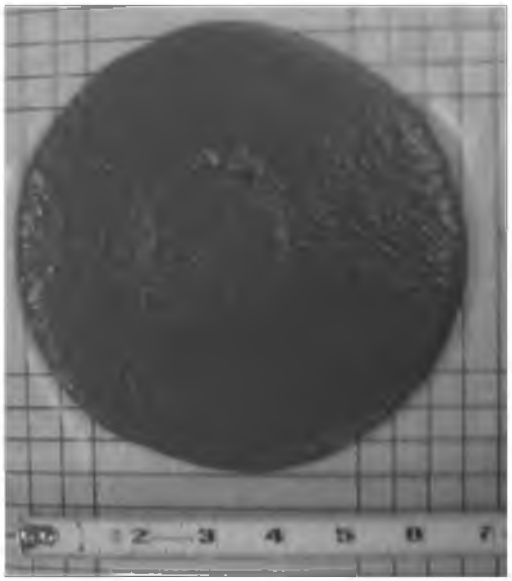

Figure 7. Nissco SS Mortar Flow Test

2.1.1.4 NMB Sleeve Grouting

A Kenrich model GP-2HD hand operated grout pump, shown in Figure 8, was used to pump the grout into the splice sleeves. Before adding the grout to the hopper, the pump was first primed with water to lubricate the parts and clean out any debris. The mixed grout was then added to the pump and operated to remove the excess water. The water and grout slurry that initially comes out of the pump is discarded and not used in the splice sleeves. Once a solid stream of grout came out of the nozzle, it was inserted into the grout inlet tube, as shown in Figure 9.

The grout was continuously pumped until it could be seen coming from the outlet tube in a solid flow and sealed with a stopper. The nozzle was then withdrawn from the inlet tube while

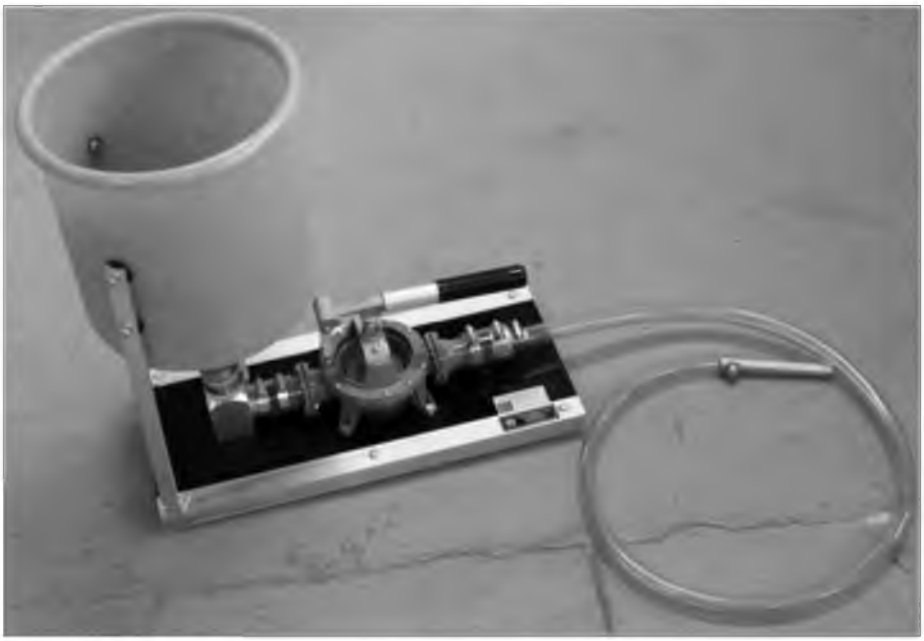

Figure 8. Kenrich Model GP-2HD Hand Operated Grout Pump

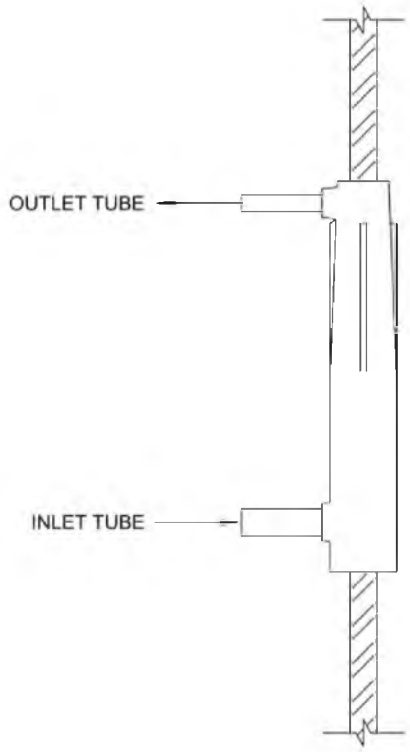

Figure 9. NMB Inlet and Outlet Tubes

continuing to pump to ensure the entire length of the inlet tube was full of grout and sealed with a stopper. Figure 10 shows the grouted and sealed NMB splice sleeves. The sleeves were left to cure in the wooden construction apparatus for 26 days before removal.

2.1.1.5 Nissco SS Mortar Cubes

Grout cubes were made following ASTM C109 (18) from the same grout in the splice sleeves and cured in a humid room at the University of Utah Concrete Lab until testing. The compressive strength of the grout was tested at 7, 14, 21, and 28 days. The results from these tests are presented in section 2.2.1.2.

2.1.1.6 NMB Splice Sleeve Instrumentation

Strain gages and AE sensors were used to monitor the specimens as they were loaded in tension to failure. Figure 11 is a drawing showing the location of all the strain gages and AE sensors. In Figure 11, the strain gages and AE sensors are denoted as SG and AE, respectively.

Figure 10. Grouted and Sealed NMB Splice Sleeves

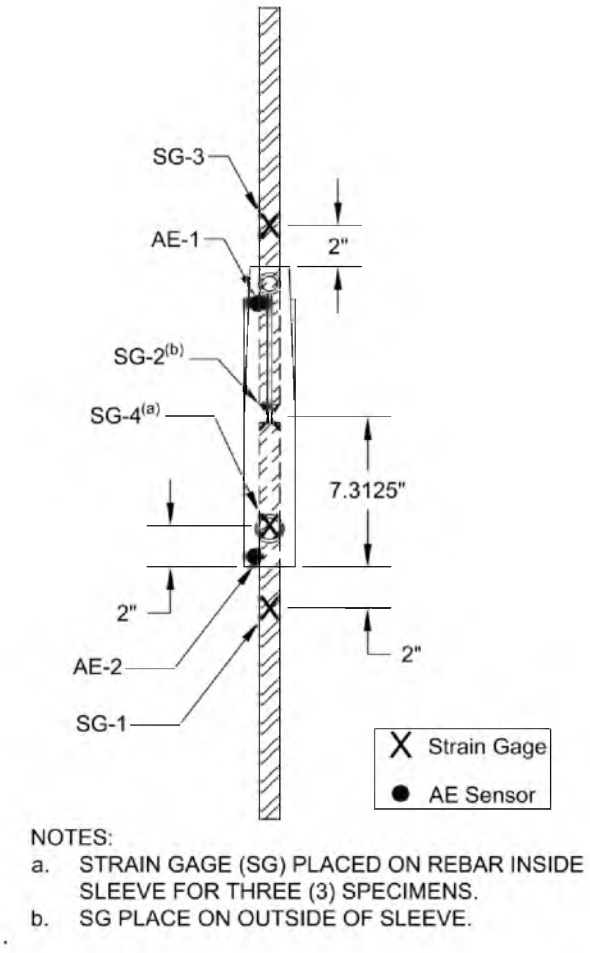

Figure 11. NMB Strain Gage and AE Sensor Locations

All six sleeves had a typical strain gage layout with the gages applied on the field dowel (SG-1), middle of the splice sleeve (SG-2), and on the factory dowel (SG-3). For three of the sleeves, however, an additional strain gage was added to the field dowel inside the splice sleeve (SG-4). The six sleeves were also equipped with 2 AE sensors. These sensors were located at the top (AE-1) and bottom (AE-2) of the sleeve.

2.1.1.7 NMB Tension Test Procedure

To obtain the tensile performance and AE characteristics of the NMB splice sleeves, tension tests were performed using an Instron Satec Series testing apparatus equipped with mechanical bar grips. Figure 12 shows the test setup for the NMB splice sleeve tension tests. A

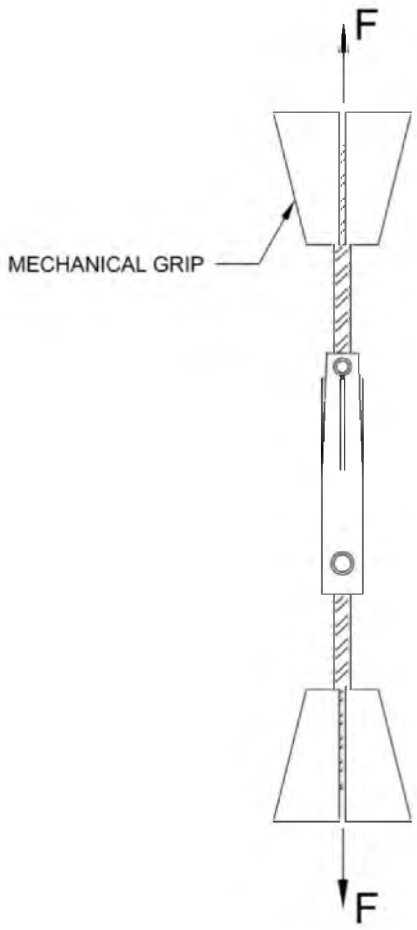

Figure 12. NMB Splice Sleeve Test Setup

total of six specimens were tested at two different load rates. Three of the sleeves were loaded at a rate of 0.4 in./min. and three were loaded at a rate of 4.0 in./min. This rate is measured as the speed at which the two heads of the testing apparatus move apart.

Table 1 summarizes the different parameters for each test. Each sleeve ID has a particular component that corresponds to different parameters. The first letters represent the sleeve type being tested. The number corresponds to the test sequence number. The final letter corresponds to the load rate. For example, sleeve NMB-3-S was an NMB splice sleeve loaded at a slow load rate and was the third sleeve tested.

Table 1. NMB Splice Sleeve Specimen ID

Sleeve ID	Load Rate (in/min)	Strain Gage In Splice Sleeve
NMB-1-F	4.0	No
NMB-2-F	4.0	No
NMB-3-S	0.4	No
NMB-4-S	0.4	Yes
NMB-5-S	0.4	Yes
NMB-6-F	4.0	Yes

2.1.2 Lenton Interlock Splice Sleeve Setup

2.1.2.1 Lenton Interlock Test Specimen Dimensions

To determine the required bar length to be spliced, the Lenton Interlock Instruction Manual along with ASTM Standards were used. The Lenton Interlock Instruction Manual specifies the minimum and maximum length for the field dowel, which is the grouted bar. The field dowel is required to have a minimum length of 6 in. and a maximum length of 7 in. To maintain consistency between the two splice sleeve systems, a field dowel length of 7 in. was chosen.

The total length of the bars followed the same criteria described for the NMB splice sleeves. From these criteria, a bar length of 19.25 in. was chosen which left a free length between the sleeve and grips of 6.25 in. on the field dowel side. For the threaded bar, it was determined to make this 19.25 in. long as well in order to keep the two bars being spliced the same overall length. Figure 13 shows dimensions of the Lenton Interlock test specimen.

2.1.2.2 Lenton Interlock Construction Apparatus

To minimize eccentric loading during the tension tests, a wooden apparatus was constructed to center the bars in the sleeve and keep them as close to vertical as possible. The wooden apparatus is shown in Figure 14 with the Lenton Interlock splice sleeves in place.

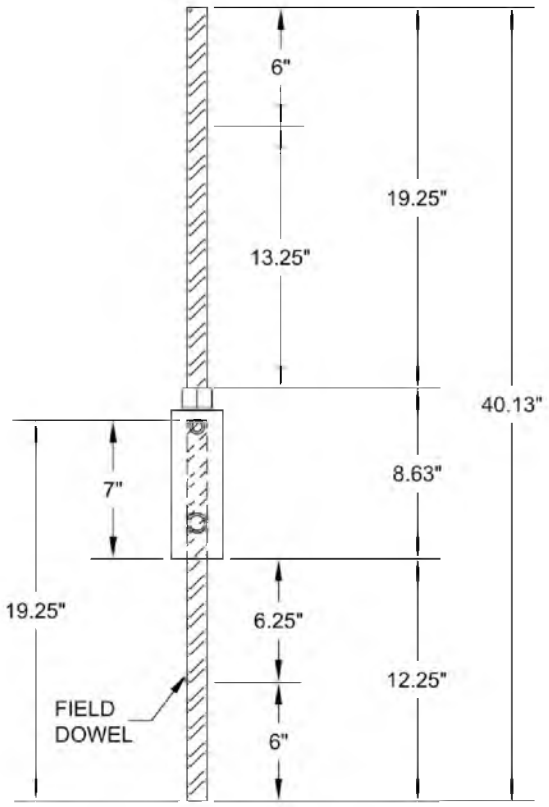

Figure 13. Lenton Interlock Splice Sleeve Dimensions

Figure 14. Wooden Construction Apparatus Lenton

2.1.2.3 Mixing of HY10L Grout

With the splice sleeves secured in the construction apparatus, HY10L grout was mixed. HY10L grout is a specially formulated, ready to use mix, designed exclusively for use with the Lenton Interlock splicing system.

Before adding the dry grout, 0.53 gallons of potable water was added to a metal 5 gallon bucket. With the water in the 5 gallon bucket, one 50 lb bag of grout was gradually added while mixing. To mix the grout, the electric mixer and jiffler type mixing paddle shown in Figure 6 was used. After adding all the grout to the 5 gallon bucket, the grout was mixed thoroughly for an additional 5 minutes.

Once mixed, a flow test was performed following the procedure described in the Lenton Interlock Instruction Manual. This test is performed to confirm that the consistency of the grout is correct. The final diameter of the grout puddle after the test should be between 5 in. and 6.5 in. The result from the first flow test of the mixed grout is shown in Figure 15 with a puddle diameter of 2 in. With an unacceptable flow, an additional 0.08 gallons of water was added and mixed. The addition of the water resulted in an acceptable puddle diameter of 6.5 in. shown in Figure 16.

2.1.2.4 Lenton Interlock Sleeve Grouting

A Kenrich model GP-2HD hand operated grout pump, shown in Figure 8, was used to pump the grout into the splice sleeves. Before adding the grout to the hopper, the pump was first primed with water to lubricate the parts and clean out any debris. The mixed grout was then added to the pump and operated to remove the excess water. The water and grout slurry that initially comes out of the pump is discarded and not used in the splice sleeves. Once a solid stream of grout came out of the nozzle, it was inserted into the grout inlet tube, as shown in Figure 17.

The grout was continuously pumped until it could be seen coming from the outlet tube in a solid flow and sealed with a stopper. The nozzle was then withdrawn from the inlet tube and sealed with a stopper. For three of the splice sleeves, pumping was not continued while removing the nozzle from the inlet tube. After the pumping of these three was completed, it was noticed that

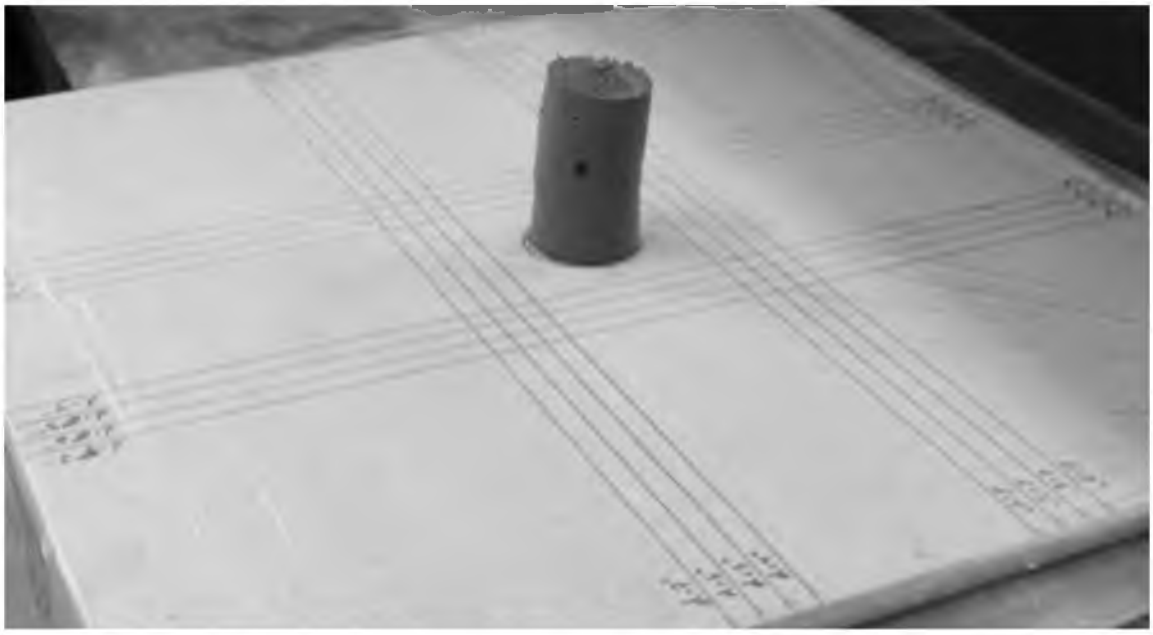

Figure 15. HY10L Flow Test 1

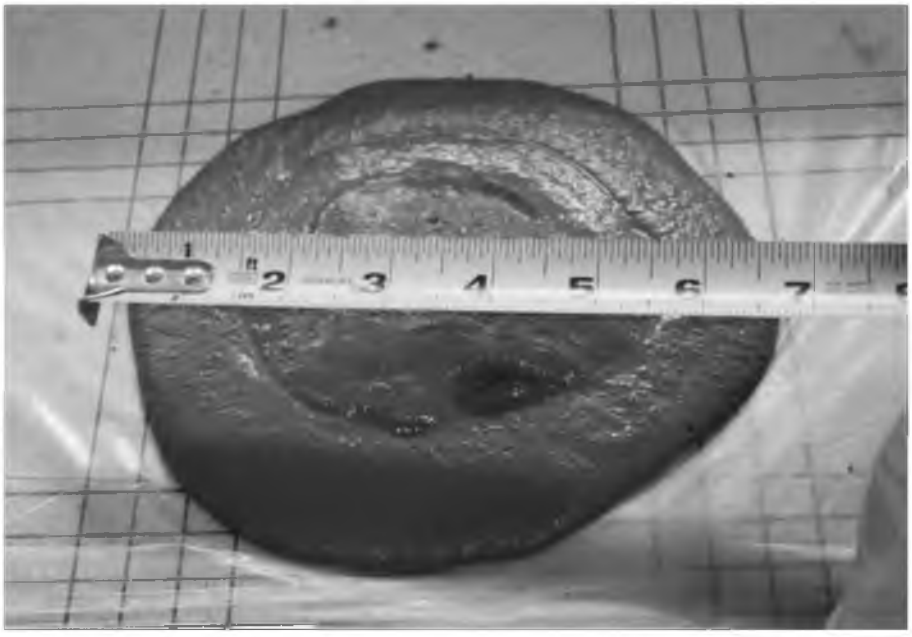

Figure 16. HY10L Acceptable Puddle Diameter

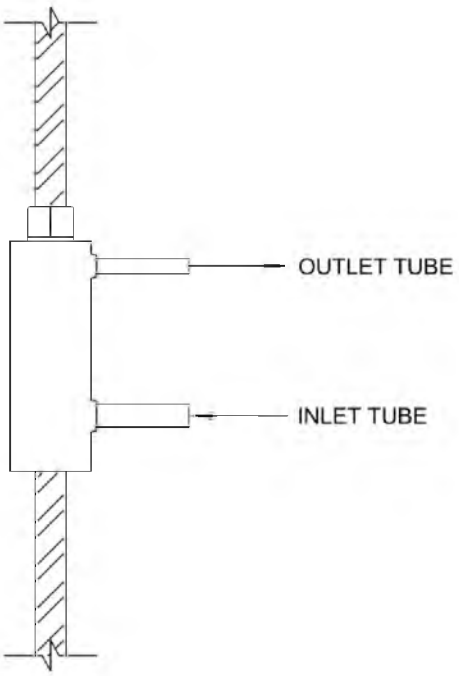

Figure 17. Lenton Interlock Inlet and Outlet Tubes

a void was being left in the inlet tube and for the remainder of the sleeves, pumping continued while the nozzle was being removed. Figure 18 shows the grouted and sealed Lenton Interlock splice sleeves. The sleeves were left to cure in the wooden construction apparatus for 26 days before removal.

Upon removing the Lenton Interlock splice sleeves from the construction apparatus, the inlet and outlet tubes were removed to inspect the three sleeves that did not have the inlet tube completely filled with grout. This inspection revealed a small void at the very top of the sleeve. The void found is shown in Figure 19 for the three splice sleeves.

2.1.2.5 HY10L Grout Cubes

Grout cubes were made following ASTM C109 (18) from the same grout in the splice sleeves and cured in a humid room at the University of Utah Concrete Lab until testing. The compressive strength of the grout was tested at 7, 14, 21, and 28 days. The results from these tests are presented in section 2.2.1.3.

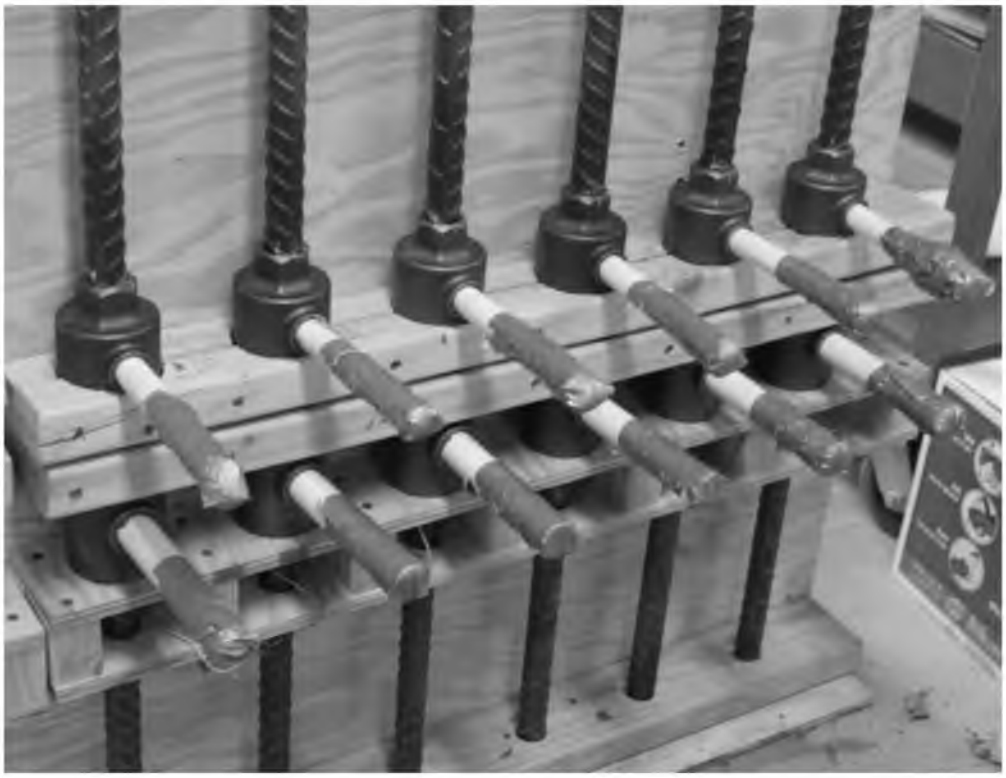

Figure 18. Grout and Sealed Lenton Interlock Splice Sleeves

Figure 19. Void at Top of Splice Sleeve

2.1.2.6 Lenton Interlock Splice Sleeve Instrumentation

Strain gages and AE sensors were used to monitor the specimens as they were loaded to failure. Figure 20 is a drawing showing the location of all the strain gages and AE sensors. All six sleeves had a typical strain gage layout with one gage applied to the field dowel (SG-1) and to the middle of the splice sleeve (SG-2), while the threaded bar had two gages(SG-3 and SG-4). For three of the sleeves, an additional strain gage was added to the field dowel inside the splice sleeve (SG-5). The six sleeves were also equipped with 2 AE sensors. These sensors were located at the top (AE-1) and bottom (AE-2) of the sleeve.

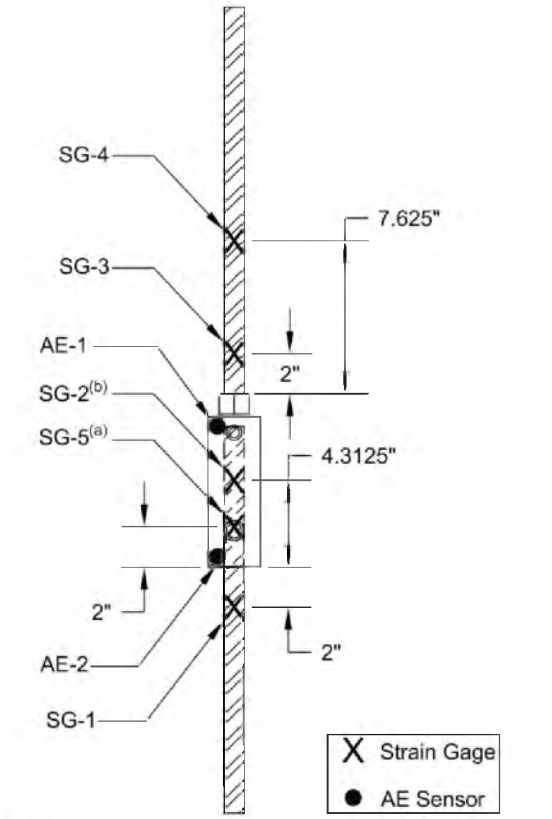

Figure 20. Lenton Interlock Strain Gage and AE Sensor Locations

2.1.2.7 Lenton Interlock Tension Test Procedure

To obtain the tensile performance and AE characteristics of the Lenton splice sleeves, tension tests were performed using an Instron Satec Series testing apparatus equipped with mechanical bar grips. Figure 21 shows the test setup for the Lenton splice sleeve tension tests. A total of six specimens were tested at two different load rates. Three of the sleeves were loaded at a rate of 0.4 in./min. and three were loaded at a rate of 4.0 in./min.

Table 2 summarizes the different parameters for each test. Each sleeve ID has a particular component that corresponds to different parameters. The first letter represents the sleeve type being tested. The number corresponds to the test sequence number. The final letter

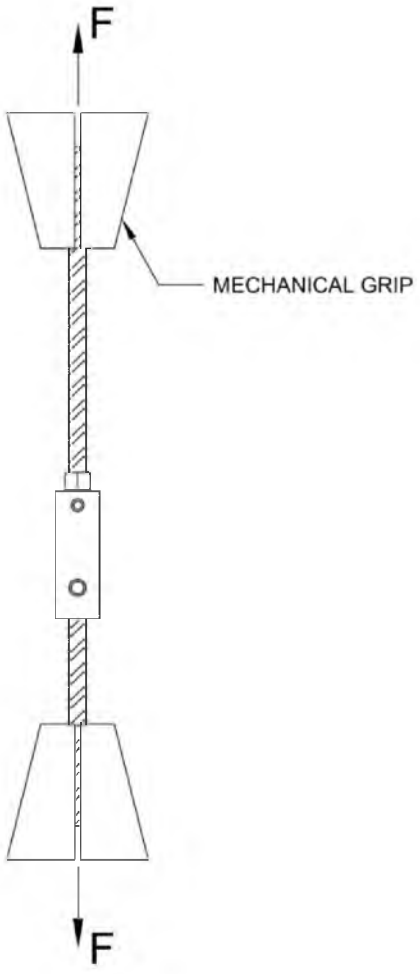

Figure 21. Lenton Interlock Splice Sleeve Test Setup

Table 2. Lenton Interlock Splice Sleeve Specimen ID

Sleeve ID	Load Rate (in/min)	Strain Gage in Splice Sleeve	Void in Grout at Top of Sleeve
Lenton-1-F	4.0	No	Yes
Lenton-2-F	4.0	No	Yes
Lenton-3-S	0.4	No	Yes
Lenton-4-S	0.4	Yes	No
Lenton-5-S	0.4	Yes	No
Lenton-6-F	4.0	Yes	No

corresponds to the load rate to which the sleeve was subjected. For example, sleeve ID Lenton-2-F was a Lenton Interlock splice sleeve loaded at a fast load rate and was the second sleeve tested.

2.2 Grouted Splice Sleeve Tension Test Results

2.2.1 Material Properties

2.2.1.1 Bar Tensile Properties

Grade 60 #8 (1 in. diameter) bars were used for all of the splice sleeve tension tests. Tension tests of the bars used were performed following ASTM A370-09a (17) at load rates of 4.0 in/min and 0.4 in./min. Each bar was instrumented with one strain gage located in the middle of the bar to determine its mechanical properties. The results from these tests are shown in Table 3. The bar properties shown in Table 3 were obtained by averaging three separate tensile tests for each load rate. It should be noted that due to the deformations on the bars, the yield strain and modulus of elasticity are slightly skewed. However, since all the strain gages are placed on the bar in the same manner for these tests as well as the concrete subassembly tests, it is reasonable to use these values when analyzing the results.

Table 3. Bar Properties for Splice Sleeve Tension Tests

Rebar	Load Rate (in/min)	F_y (ksi)	ε_y (in/in)	E (ksi)	F_u (ksi)	ε_u (in/in)
Slow Load	0.4	75.30	0.0031	24190	102.51	0.1458
Fast Load	4.0	76.64	0.0027	28763	103.91	0.1458

2.2.1.2 Nissco SS Mortar Compressive Strength

The compressive strength of the Nissco SS Mortar was tested at 7, 14, 21, and 28 days following the testing procedure in ASTM C109 (18). The specimens were compressed to failure with an Instron Satec Series testing apparatus at a loading rate of 300 lbs/s. Table 4 shows the results from the compression tests. It should be noted that the 28-day compressive strength of the Nissco SS Mortar is the compressive strength of the grout for the NMB splice sleeve tension tests.

2.2.1.3 HY10L Grout Compressive Strength

The compressive strength of the HY10L Grout was tested in the same way as the Nissco SS Mortar. Table 5 shows the results from the compression tests. It should be noted that the 28-day compressive strength of the HY10L Grout is the compressive strength of the grout for the Lenton Interlock splice sleeve tension tests.

Table 4. Nissco SS Mortar Compressive Strength

Days	Cube 1 f'c (ksi)	Cube 2 f'c (ksi)	Cube 3 f'c (ksi)	Average f'c (ksi)
7	12.36	12.46	13.05	12.62
14	15.2	14.75	14.46	14.80
21	16.16	16.59	14.94	15.90
28	14.79	12.698	13.97	13.82

Table 5. HY10L Grout Compressive Strength

Day	Cube 1 f'c (ksi)	Cube 2 f'c (ksi)	Cube 3 f'c (ksi)	Average f'c (ksi)
7	7.96	8.47	8.37	8.27
14	10.3	10.44	10.33	10.36
21	8.12	10.03	10.54	10.29
28	9.93	9.17	9.15	9.42

2.2.2 NMB Tension Test Results

After allowing the SS Mortar to cure for 28 days, tension tests of the NMB splice sleeve assembly were performed. The tension tests consisted of two different load rates. NMB-1-F, NMB-2-F, and NMB-6-F were loaded at a rate of 4.0 in./min, while NMB-3-S, NMB-4-S, and NMB-5-S were loaded at a rate of 0.4 in./min. Table 6 shows the results of all six NMB splice sleeve tension tests. There was no apparent difference in performance between the sleeves loaded at 0.4 in./min. and 4.0 in./min. All six of the tension tests resulted in a tensile failure of either the field or factory dowel. Figure 22 shows the six NMB Splice sleeves and their failure mode.

According to the 2011 AASHTO LRFD Bridge Design Specifications (19), the resistance of a mechanical connection shall not be less than 125 percent of the specified yield strength of the bar. Since all NMB splice sleeves resisted between 164 and 172 percent of the specified yield strength of the bar, they meet this requirement. However, according to the 2011 AASHTO Guide

Table 6. NMB Splice Sleeve Tension Test Results

Sleeve ID	Load Rate (in/min)	Maximum Load (kips)	Maximum Rebar Stress (ksi)	$\%F_y$*	Failure Mode
NMB-1-F	4.0	81.17	103.35	1.72	Field Dowel Failure
NMB-2-F	4.0	80.65	102.69	1.71	Field Dowel Failure
NMB-3-S	0.4	80.09	101.98	1.70	Field Dowel Failure
NMB-4-S	0.4	79.91	101.74	1.70	Field Dowel Failure
NMB-5-S	0.4	79.55	101.29	1.69	Factory Dowel Failure
NMB-6-F	4.0	77.33	98.46	1.64	Field Dowel Failure

* F_y = specified yeild strength, 60 ksi

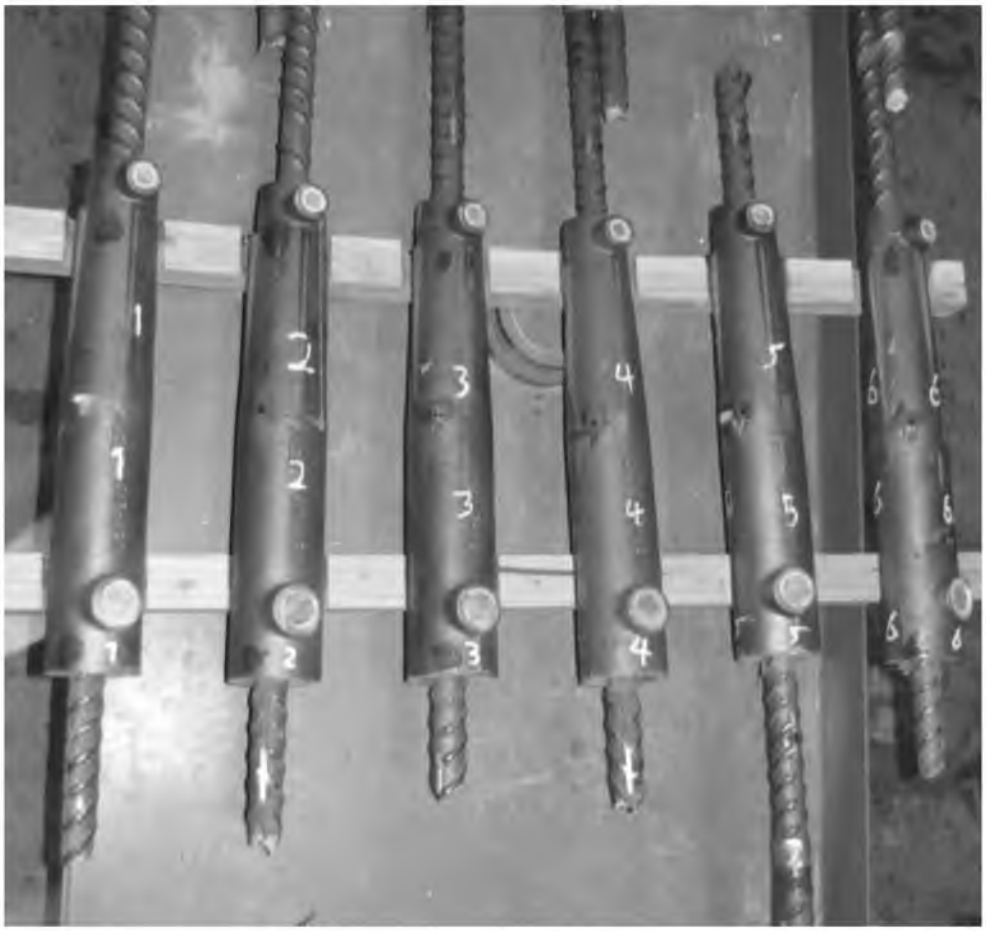

Figure 22. NMB Splice Sleeve Failure Mode

Specifications for LRFD Seismic Bridge Design (20), no mechanical splices are allowed in the plastic hinge zone of the column for seismic design categories C and D.

Furthermore, ACI 318-11 (21) classifies mechanical connections as either a Type 1 or Type 2 connection. A Type 1 connection is required to develop at least 125 percent the specified yield strength of the bar and is not allowed to be used within a distance of twice the member depth from sections where yielding of the reinforcement is likely to occur. While a Type 2 mechanical connection must develop, the specified tensile strength of the spliced bar and can be used at any location. According to ACI 550.1R-09 (22), the specified tensile strength of a reinforcing bar can be taken as 160 percent the specified yield strength of the bar for mechanical connections in plastic hinge areas. Since all NMB splice sleeves resisted between 164 and 172 percent of the specified yield strength of the bar and all the tests resulted in tensile failure of the

bar, they meet the requirements of a Type 2 mechanical connection.

2.2.2.1 NMB Tension Test Observations

While the NMB splice sleeve was being loaded, a small portion of the grout on the field dowel side broke out. This small amount of grout breakout was caused by necking of the bar and occurred after the field dowel yielded. Figure 23 (a) shows the grout breakout after failure of the splice sleeve occurred. By removing the broken grout, the depth of the grout cone can be observed and is shown in Figure 23 (b). The depth of grout cone ranged from 1/2 in. to 3/4 in.

After the tests were completed, the rubber end cap plug was removed from the factory dowel side of the sleeve to inspect the integrity of the grout. From the inspection, it showed there had been some necking of the bar at the factory dowel end of the sleeve as well. The necking of the factory dowel, however, caused less breaking of the grout on the field dowel side. Figure 24 shows the typical integrity of the grout on the factory dowel end. The depth of the broken grout on the factory dowel end of the sleeve ranged from 1/4 in. to 1/2 in.

2.2.3 Lenton Interlock Tension Test Results

After allowing the HY10L Grout to cure for 28 days, tension tests of the Lenton Interlock splice sleeve assembly were performed. The tension tests were carried out at two different load

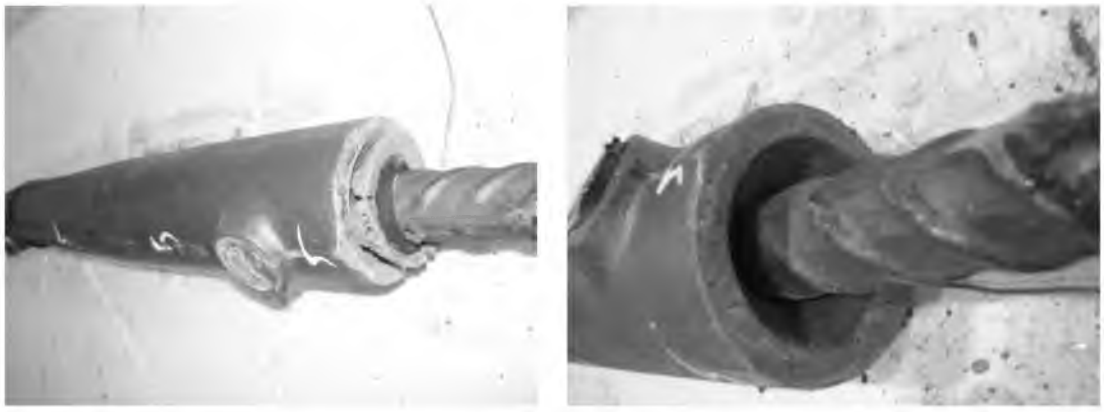

(a) (b)

Figure 23. NMB Splice Sleeve Grout Breakout: (a) with Grout Cone (b) with Grout Cone Removed

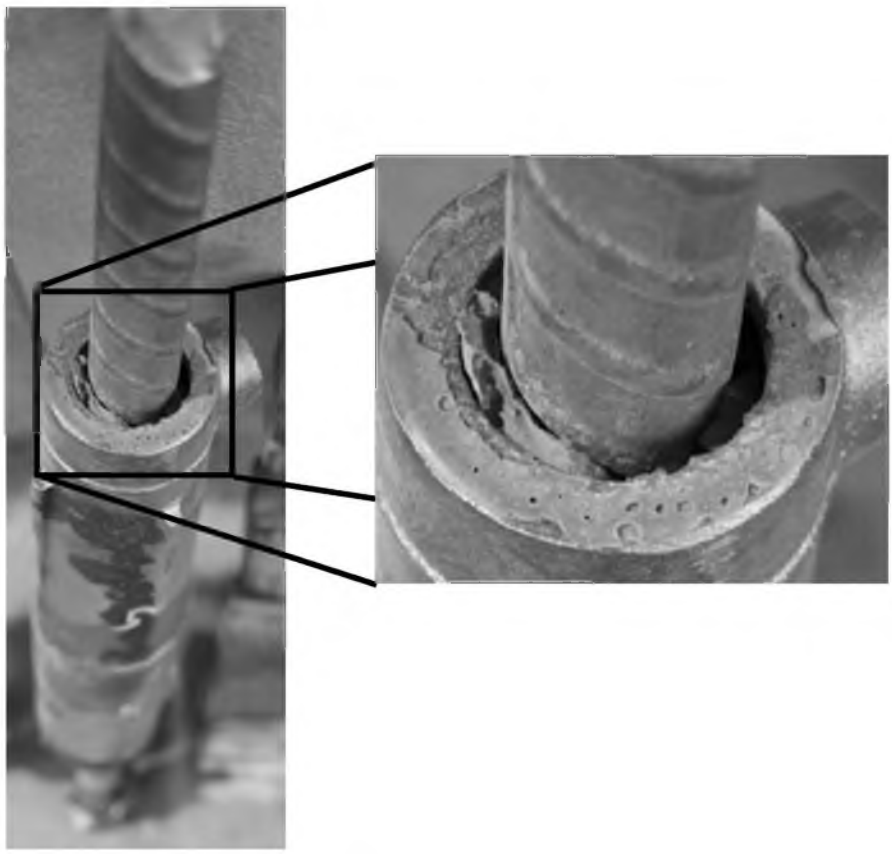

Figure 24. NMB Splice Sleeve Factory Dowel Grout Integrity

rates. Lenton-1-F, Lenton-2-F, and Lenton-6-F were loaded at a rate of 4.0 in./min, while Lenton-3-S, Lenton-4-S, and Lenton-5-S were loaded at a rate of 0.4 in./min. Table 7 shows the results of all six Lenton Interlock splice sleeve tension tests. Neither the load rate nor the void at the top of the sleeve seemed to affect the performance of the sleeves. All six of the tension tests resulted in the field dowel being pulled out of the grout. Figure 25 shows the six Lenton Interlock splice sleeves and their failure mode. During the test, the bar was not completely pulled from the sleeve, because once the bar began to pull out, the splice sleeve was unable to maintain the load and it was decided to stop the test. In Figure 25, there is a small ring of duct tape on the field dowel which marked the bottom of the sleeve. For the sleeves that do not have a grout cone left on the bar, the ring of duct tape can be a reference of how far the bar was pulled out. The pull out of the bar ranged from 3/4 in. up to 2 in.

Also, since all Lenton Interlock splice sleeves resisted between 137 and 152 percent of

Table 7. Lenton Interlock Splice Sleeve Tension Test Results

Sleeve ID	Load Rate (in/min)	Maximum Load (kips)	Maximum Rebar Stress (ksi)	$\%F_y$ *	Failure Mode
Lenton-1-F	4.0	69.72	88.77	1.48	Field Dowel Pull Out
Lenton-2-F	4.0	71.54	91.08	1.52	Field Dowel Pull Out
Lenton-3-S	0.4	66.39	84.53	1.41	Field Dowel Pull Out
Lenton-4-S	0.4	68.00	86.58	1.44	Field Dowel Pull Out
Lenton-5-S	0.4	64.61	82.27	1.37	Field Dowel Pull Out
Lenton-6-F	4.0	69.07	87.95	1.47	Field Dowel Pull Out

* F_y = specified yeild strength, 60 ksi

Figure 25. Lenton Interlock Splice Sleeve Failure Mode

the specified yield strength of the bar, they meet the requirements for mechanical connections according to the 2011 AASHTO LRFD Bridge Design Specifications. However, they do not meet the requirements for a Type 2 mechanical connection as defined by ACI 318-11 since the mechanical connection did not reach the specified tensile strength of the bar (160 percent the specified yield). Therefore, this would be considered a Type 1 mechanical connection and would not be allowed in locations where yield of the reinforcement is expected.

2.2.4 Tension Test AE Monitoring Assessment

While the splice sleeves were being loaded in tension, the sleeves were monitored by an AE monitoring system. This system consisted of ceramic AE sensors, preamplifiers, 8 channel FM box, and a computer. In the Appendix, a more detailed description of the AE data acquisition system, the system setting, and sensor information is given. The system records the time that an AE event occurred and what the energy of the event was. In the following sections, the AE event history and cumulative AE energy is compared between the splice sleeve tension tests to determine the AE characteristics.

While performing the tension test of NMB-6-F, the test was inadvertently started before the data acquisition systems were ready. Since the loading rate on this sleeve was so rapid, by the time the test was paused, the bars were well past yield. Instead of unloading the sleeve in order to start the systems simultaneously it was decided to continue the test and load the sleeve to failure without the data acquisition.

2.2.4.1 NMB AE Event History

Figures 26 to 30 are AE event history plots for all of the NMB splice sleeves with the load history superimposed. From these plots, it is clear that there are common characteristics between the five tests. The first characteristic is that sensor AE-2, located at the field dowel end of the sleeve, always records substantially more events than sensor AE-1, located at the factory dowel end of the sleeve. This can be attributed to the difference in the size of the opening on either end of the sleeve. Since the opening at the bottom of the sleeve is much larger than the opening at

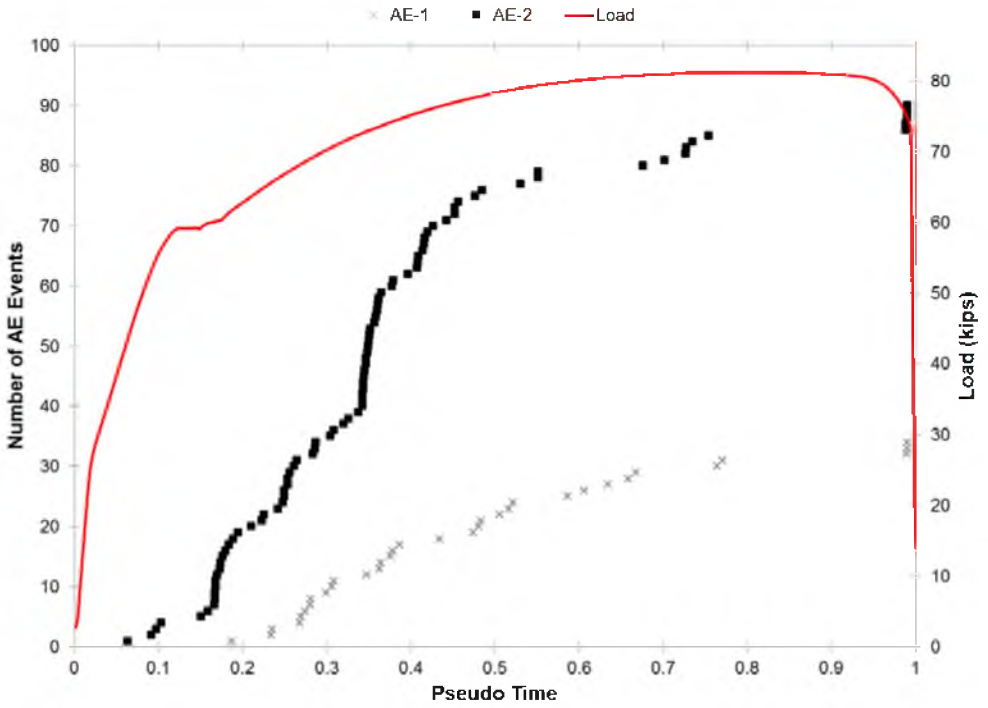

Figure 26. NMB-1-F AE Event History (With Load)

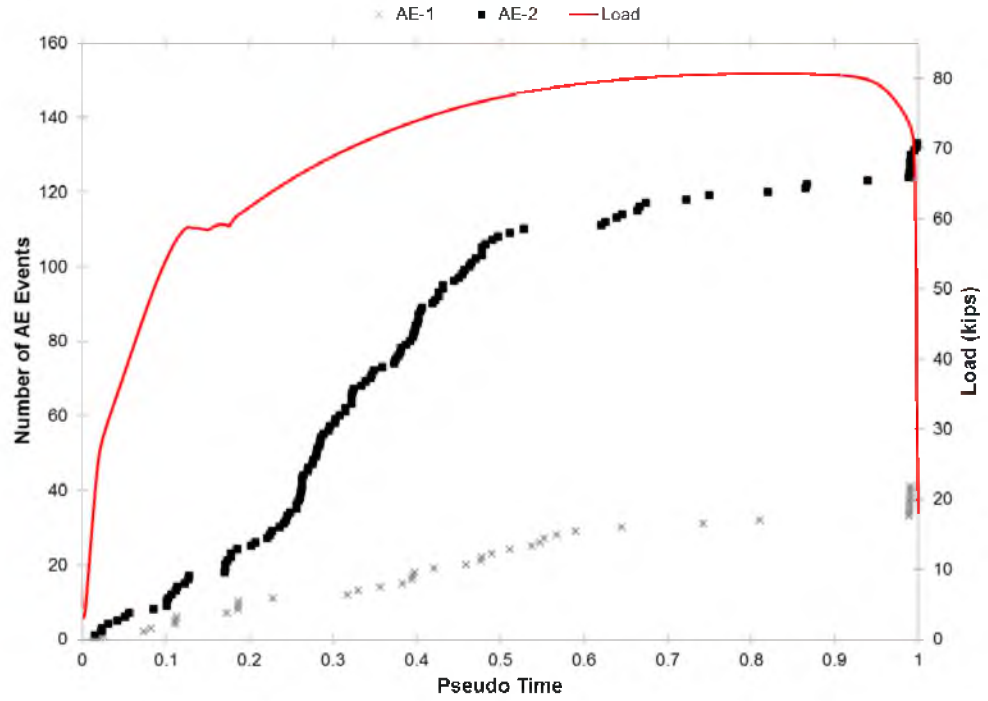

Figure 27. NMB-2-F AE Event History (With Load)

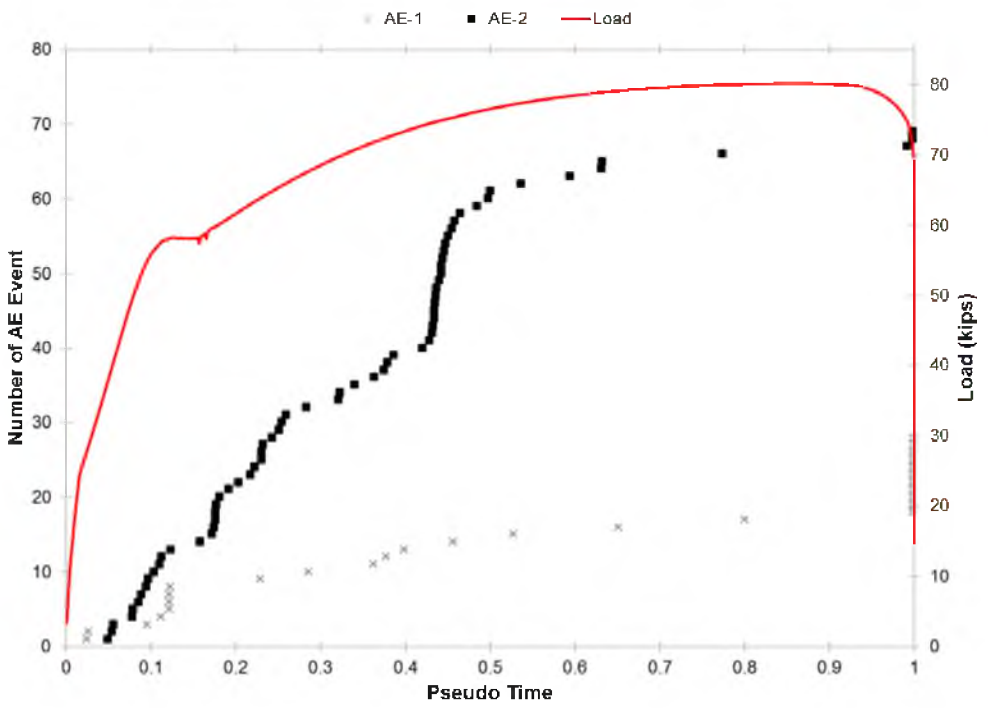

Figure 28. NMB-3-S AE Event History (With Load)

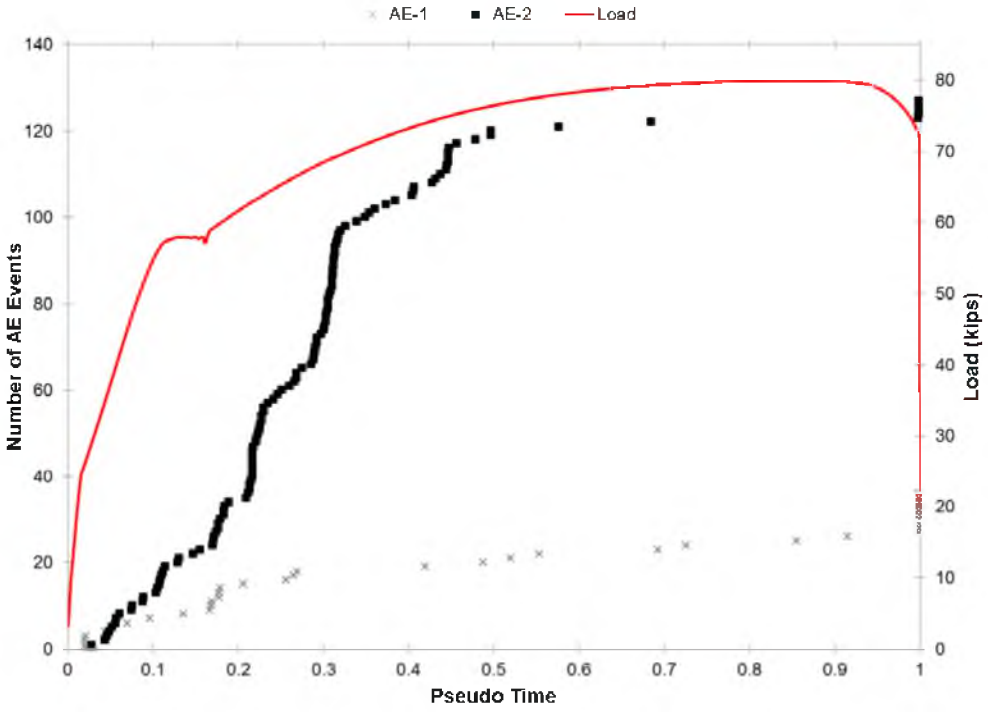

Figure 29. NMB-4-S AE Event History (With Load)

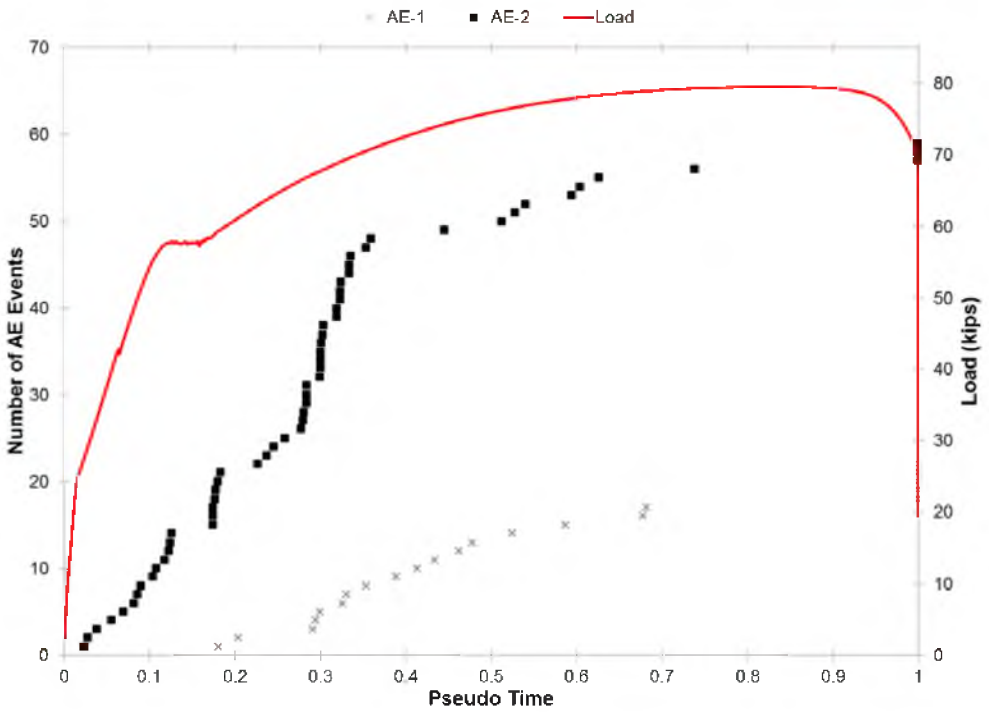

Figure 30. NMB-5-S AE Event History (With Load)

the top of the sleeve, more events are caused when necking of the bar begins to penetrate into the grout.

Another characteristic seen from the plots is that as the load reaches a plateau at the maximum load, the rate at which the AE events occur drastically decreases. This decrease in the rate of AE events in this region can be attributed to what is known as the Kaiser effect. The Kaiser effect occurs when the load is released or held constant in a structure; no AE event will occur until the load exceeds the previous maximum value (*16*). Since the load in this region remains nearly constant, the rate at which the AE events occur decreases, thus giving a sign that failure of the bar is imminent.

Figures 31 to 35 show the AE event history plots with the strain history superimposed. On these plots, a dotted line is placed at the average bar yield strain for the rate the sleeve was loaded. A common characteristic between these five plots is that while the bars are yielding, AE events do not occur and this leaves a small gap in the AE event history plot indicating when the bar yields. This small gap is attributed again to the Kaiser effect. Referring back to Figures 26 to

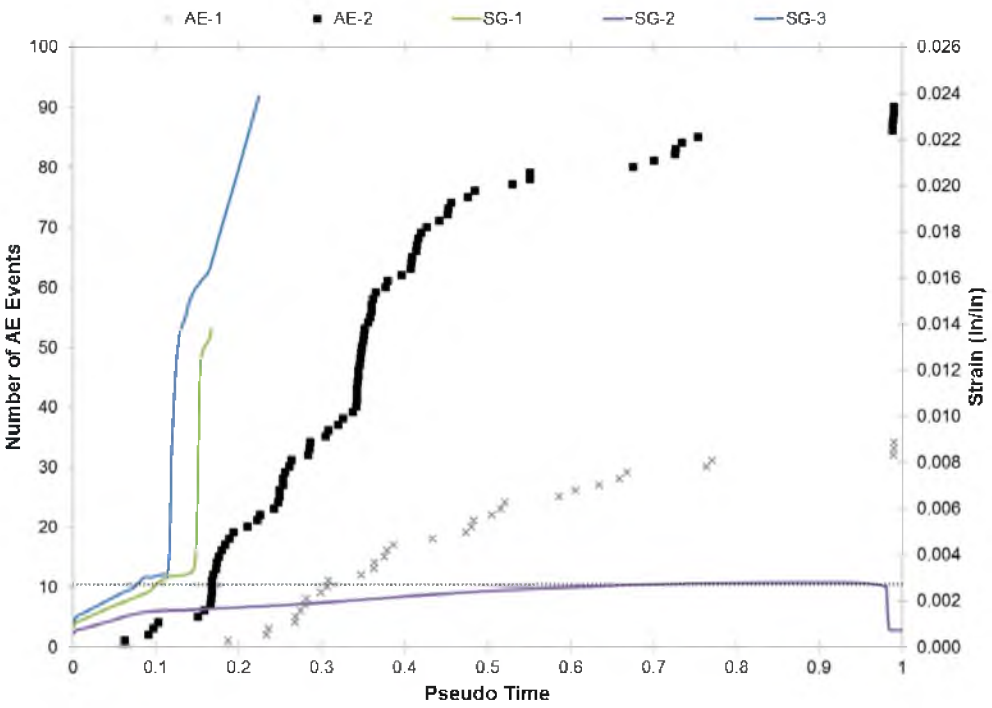

Figure 31. NMB-1-F AE Event History (With Strain)

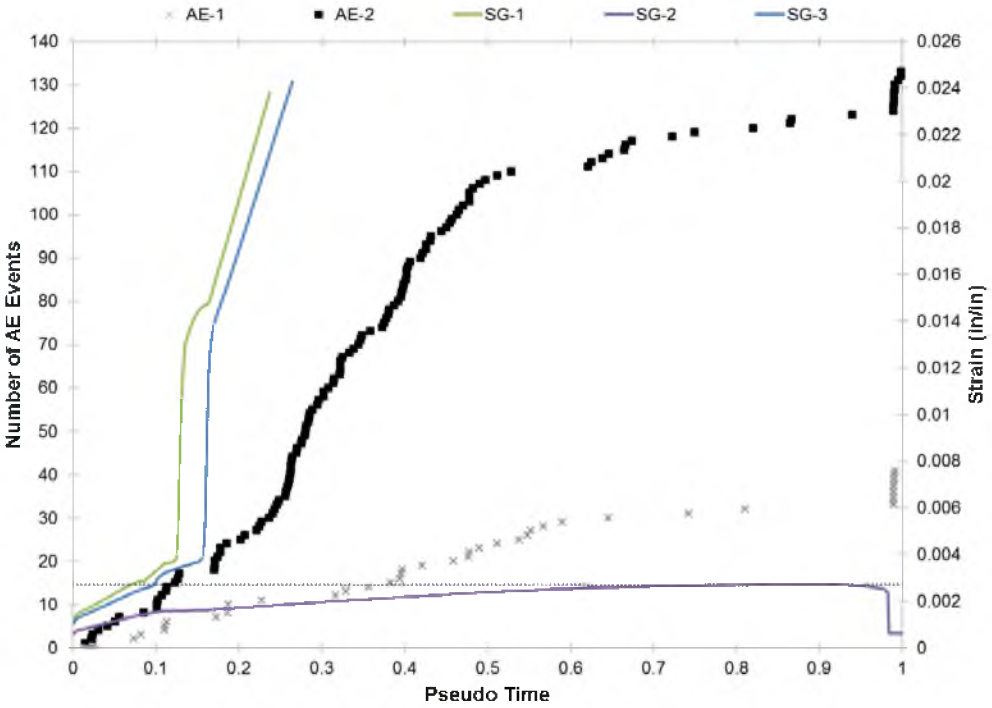

Figure 32. NMB-2-F AE Events History (With Strain)

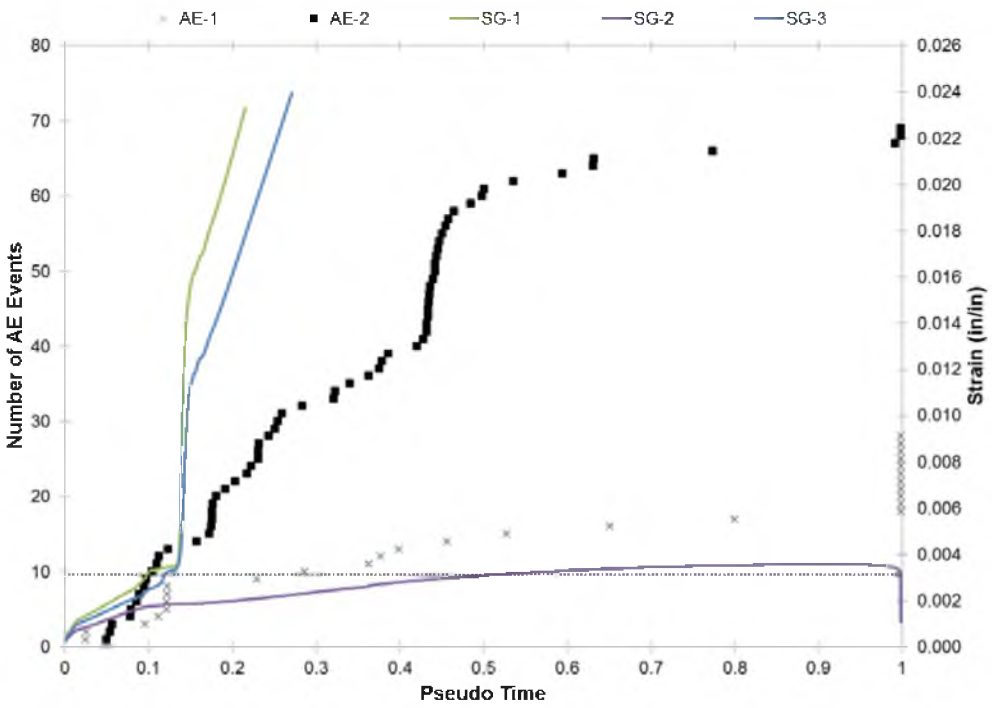

Figure 33. NMB-3-S AE Event History (With Strain)

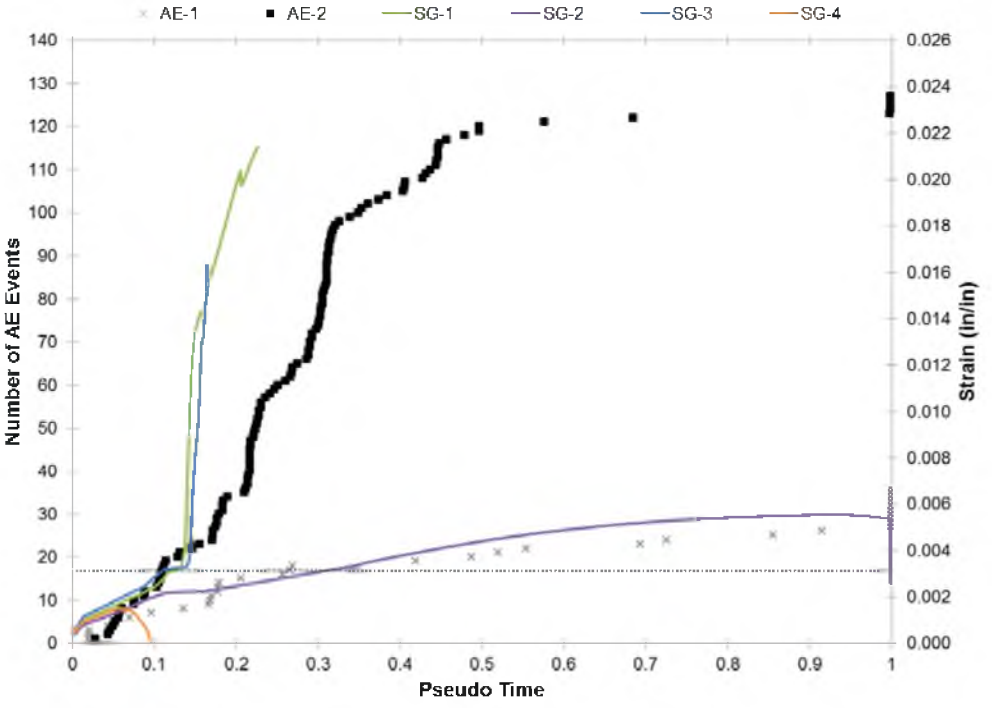

Figure 34. NMB-4-S AE Event History (With Strain)

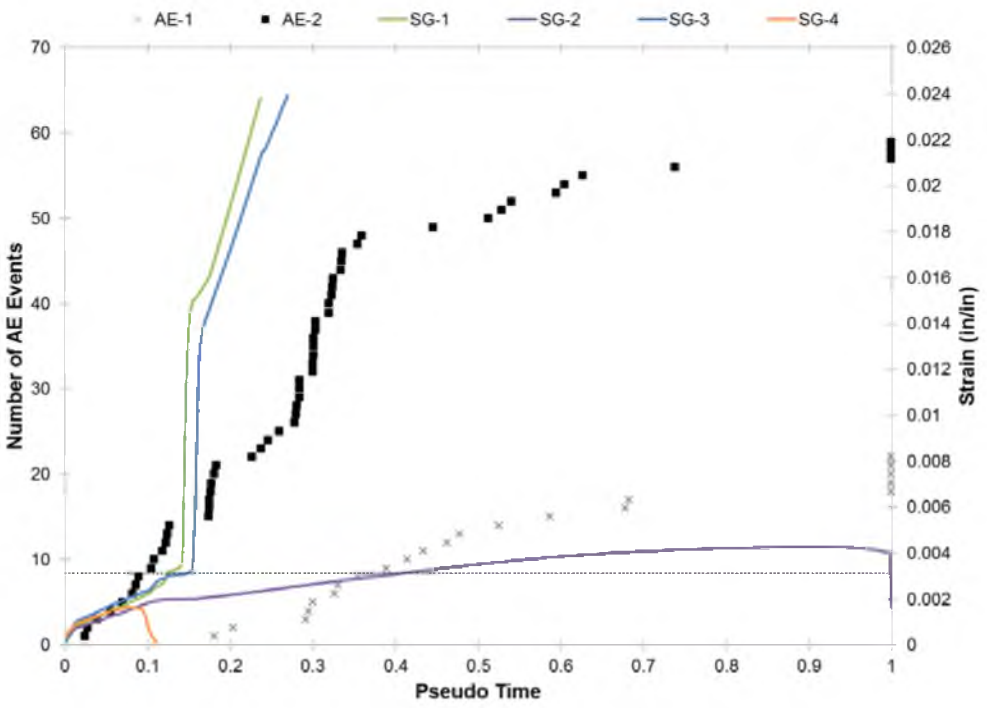

Figure 35. NMB-5-S AE Event History (With Strain)

30, it can be seen that the load is held constant during the time the bars are yielding, thus producing the Kaiser effect.

Figure 36 shows a comparison of the total number of AE events for each sensor from all five tests. From this figure, it can be seen that the total number of AE events recorded by sensor AE-1 is very similar for all five tests, while the total number of AE events recorded by sensor AE-2 varies more drastically from test to test. A reason for the variability in AE events recorded by AE-2 is that the bottom of the sleeve has a much wider opening than the top of the sleeve. Therefore, when the grout in the sleeve begins to break, a large cone breaks out of the bottom of the sleeve with lots of random events while on the top of the sleeve, only a small amount of the grout crushes with less variability.

2.2.4.2 NMB Cumulative AE Energy

Figure 37 shows a comparison of the cumulative AE energy for each sensor from all five tests. From this figure, it can be seen that there is not a strong correlation between the failure of

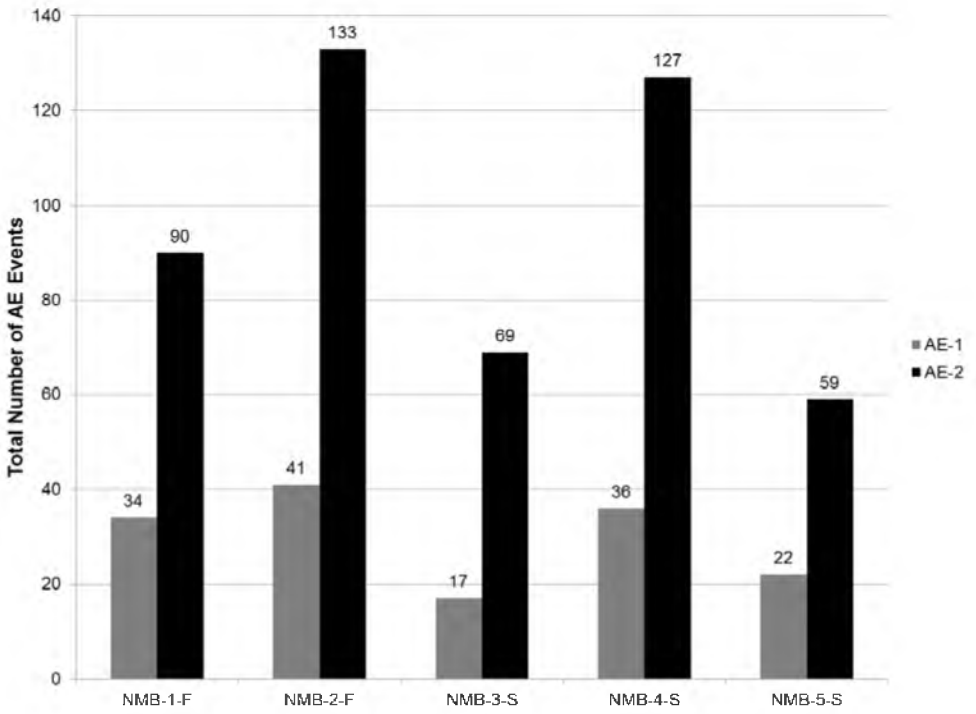

Figure 36. NMB Splice Sleeve Total AE Events Comparison

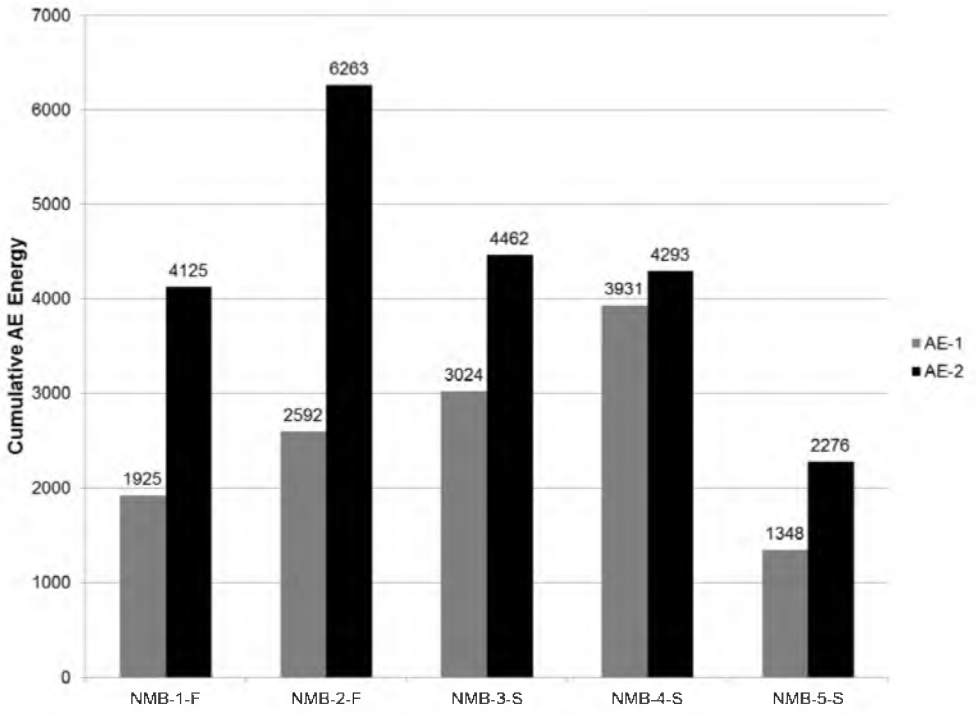

Figure 37. NMB Splice Sleeve Cumulative Energy Comparison

the splice sleeves and the amount of AE energy. This is most likely due to the randomness in which the grout cracks during the loading process releasing different amounts of AE energy.

2.2.4.3 Lenton Interlock AE Event History

Figures 38 to 43 are the AE event history plots for all of the Lenton Interlock splice sleeves with the load history superimposed. From these plots, it is obvious that there are common characteristics between the five tests. The first characteristic is that sensor AE-2, located at the field dowel end of the sleeve, always records substantially more events than sensor AE-1. This can be attributed to the field dowel being pulled out of the sleeve causing the majority of the events to occur near sensor AE-2.

There is also a very strong correlation between when the field dowel pulls out and an increase in the rate at which the AE events occur. In Figures 38 to 43, a vertical dashed line represents where the field dowel begins to pull out. In all of the tension tests, except Lenton-5-S, the vertical dashed line coincides very closely to where the rate of AE events begins to increase.

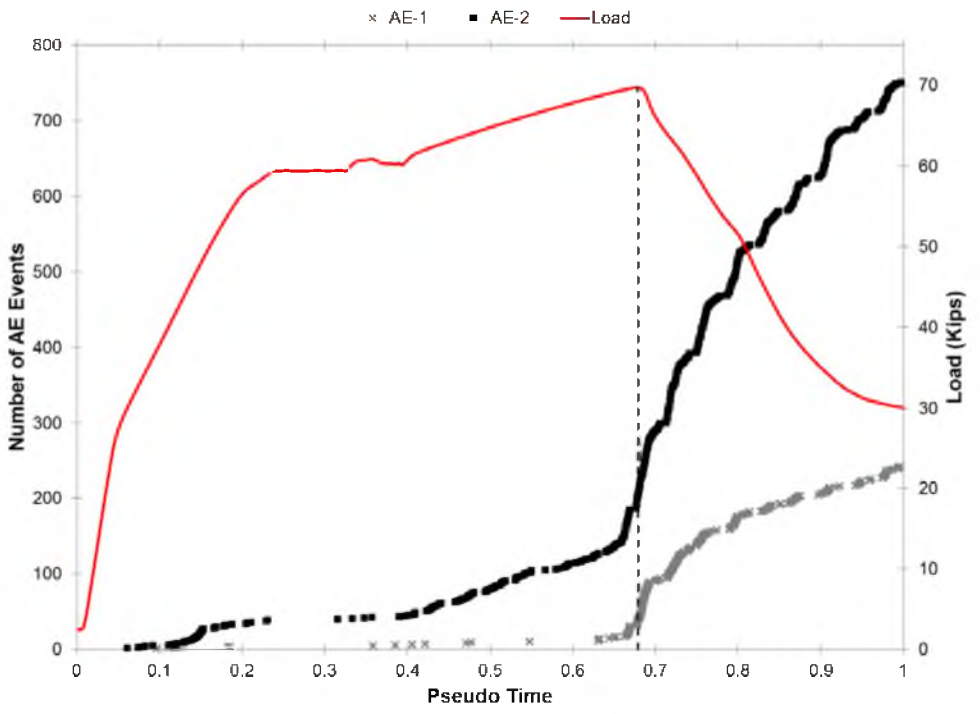

Figure 38. Lenton-1-F AE Event History (With Load)

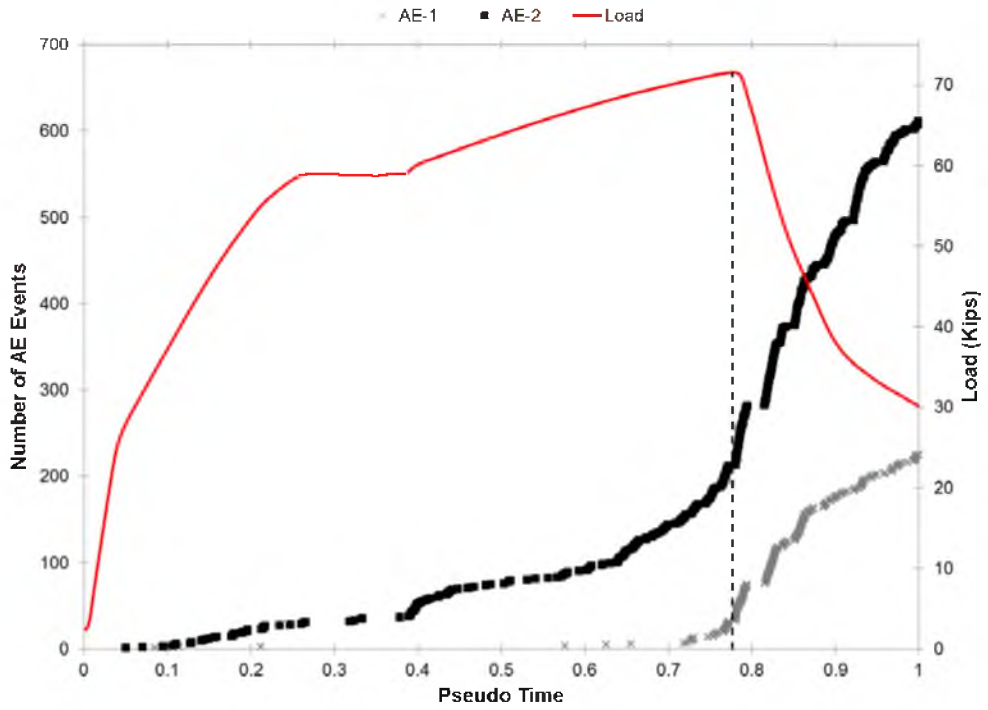

Figure 39. Lenton-2-F AE Event History (With Load)

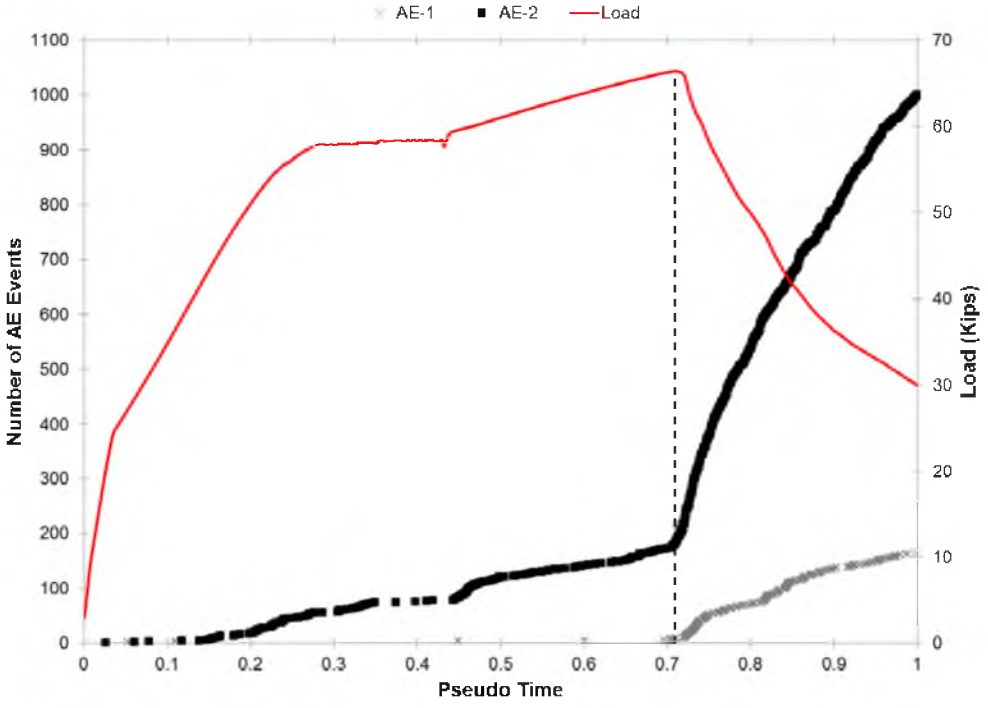

Figure 40. Lenton-3-S AE Event History (With Load)

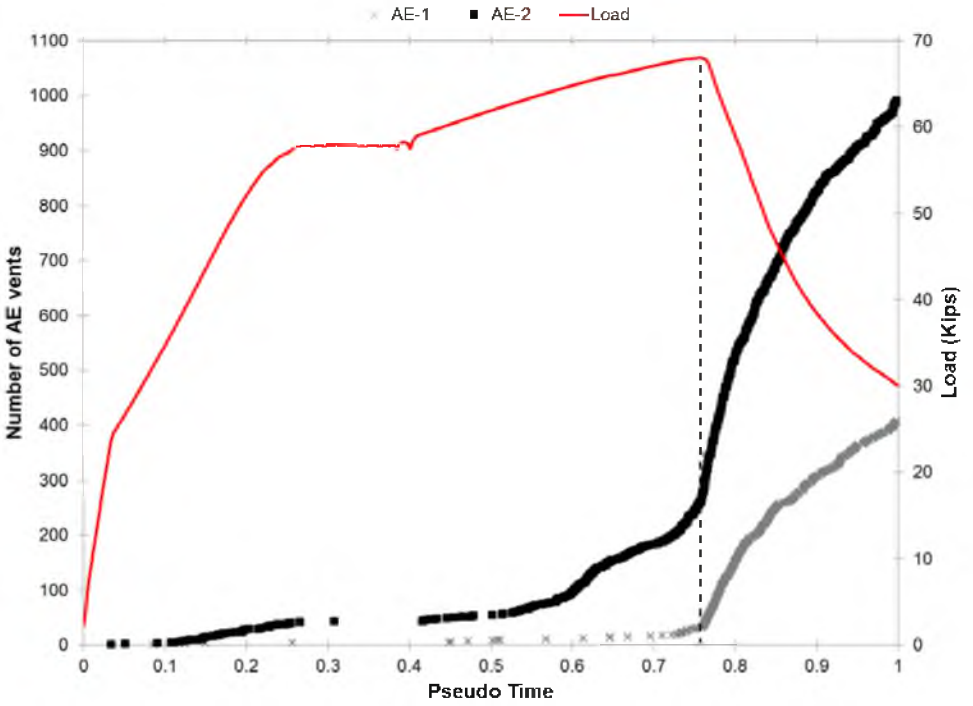

Figure 41. Lenton-4-S AE Event History (With Load)

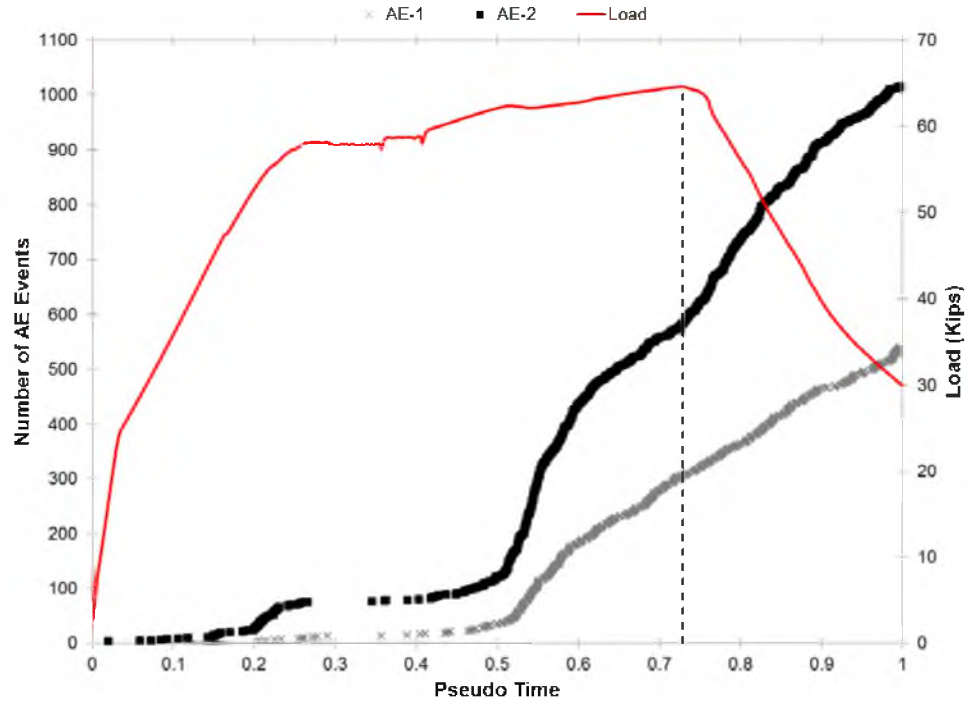

Figure 42. Lenton-5-S AE Event History (With Load)

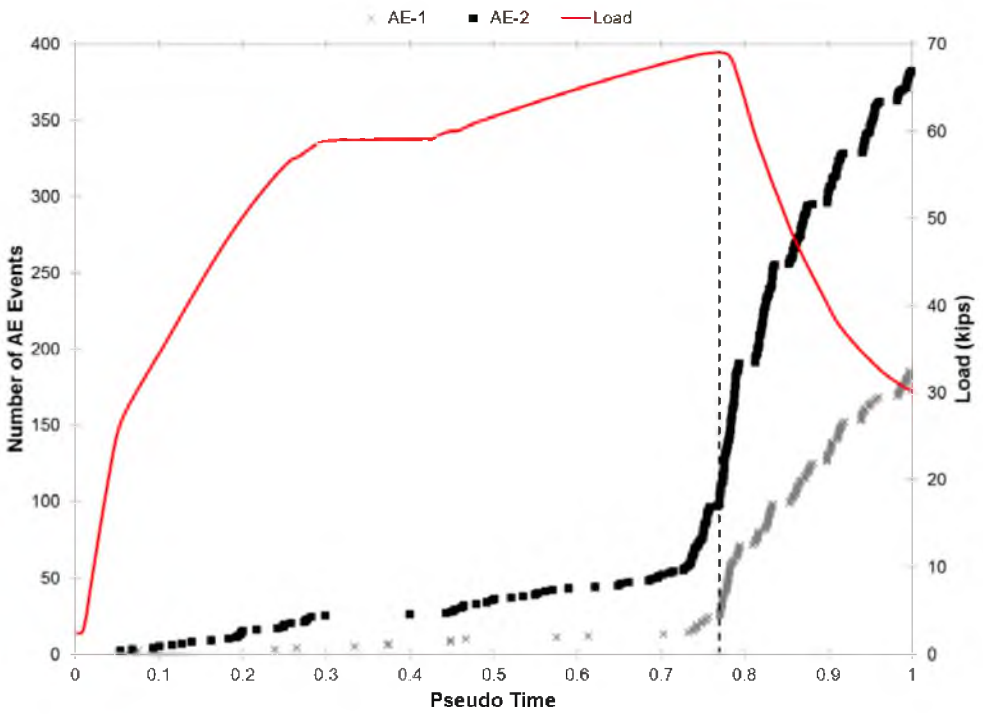

Figure 43. Lenton-6-F AE Event History (With Load)

This correlation can be used to indicate when the field dowel has begun to pull out and identify failure of the grouted splice sleeve.

On the AE event history plots, the strain history from the strain gages can be superimposed instead of the load history. Figures 44 to 49 show AE event history plots with the strain history superimposed. On these plots, a horizontal dotted line is placed at the average bar yield strain for the rate the sleeve was loaded and a vertical dashed line is placed at the time the field dowel begins to pull out. A common characteristic between these five plots is that while the bars are yielding, there are gaps that appear in the AE event history plots. These small gaps are attributed to the Kaiser effect. Referring back to Figures 38 to 43, it can be seen that the load is held constant during the time the bar is yielding, thus producing the Kaiser effect.

For splice sleeves Lenton-4-S and Lenton-6-F, shown in Figure 47 and Figure 49 respectively, the strain gage located on the field dowel in the sleeve, SG-5, is lost when the field begins to pull out. For splice sleeve Lenton-5-S, shown in Figure 48, SG-5 is lost at the exact time the AE events increase in rate, which from previous tests would mean the field dowel is pulling

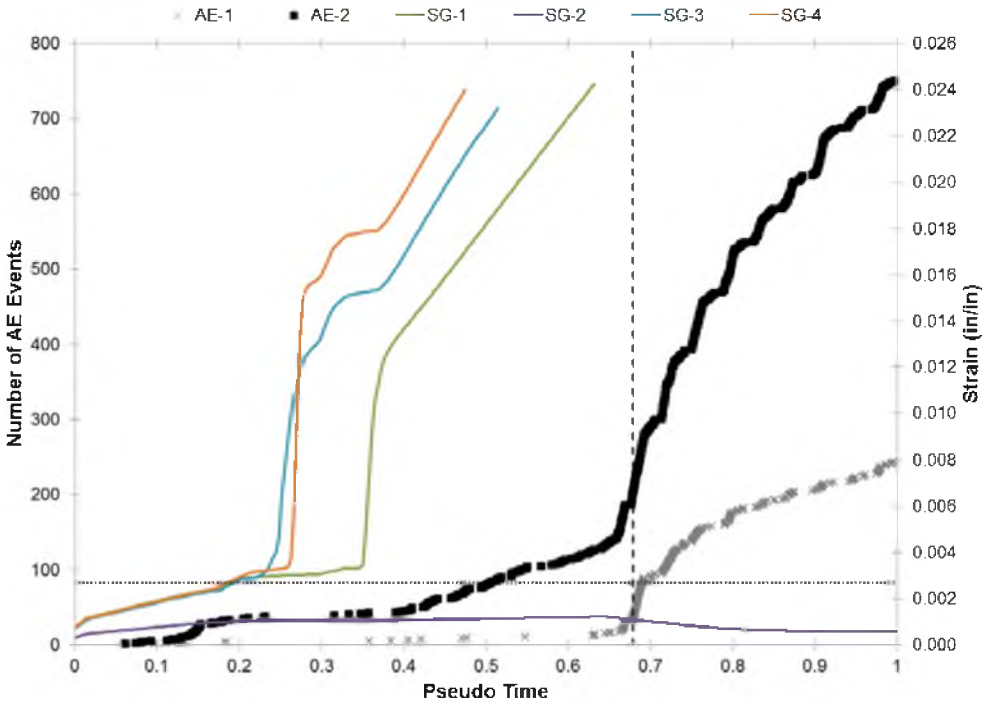

Figure 44. Lenton-1-F AE Event History (With Strain)

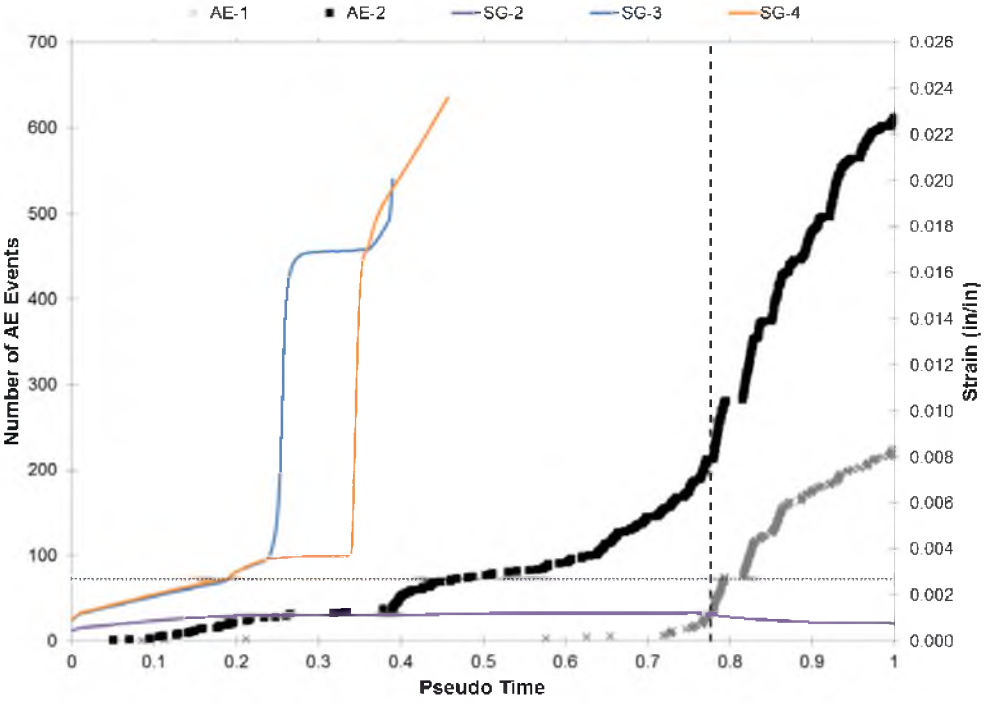

Figure 45. Lenton-2-F AE Event History (With Strain)

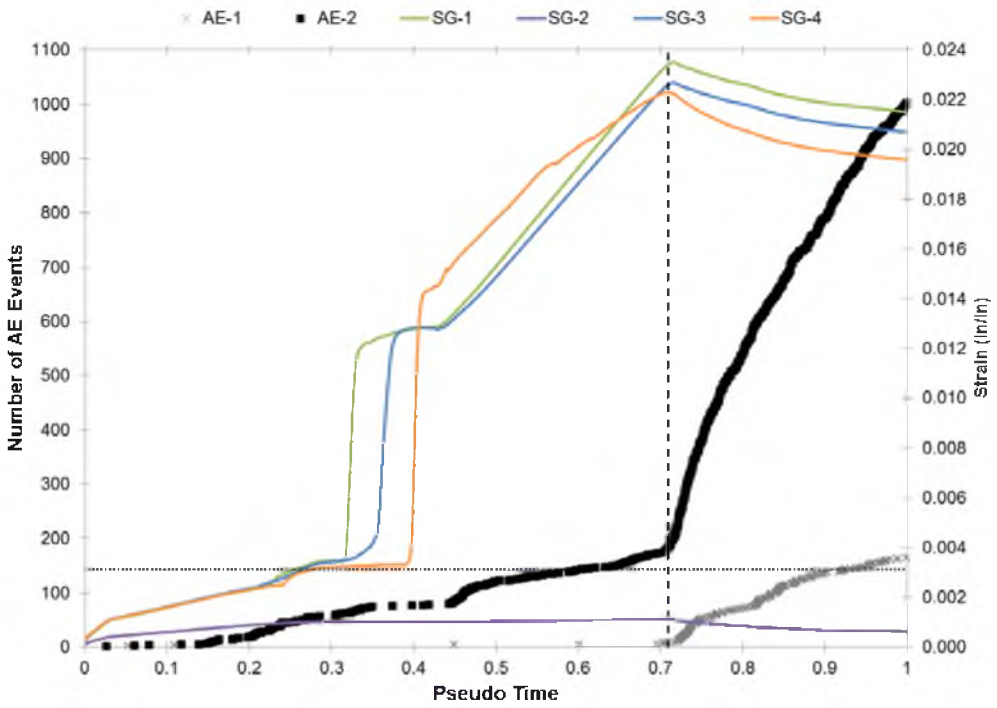

Figure 46. Lenton-3-S AE Event History (With Strain)

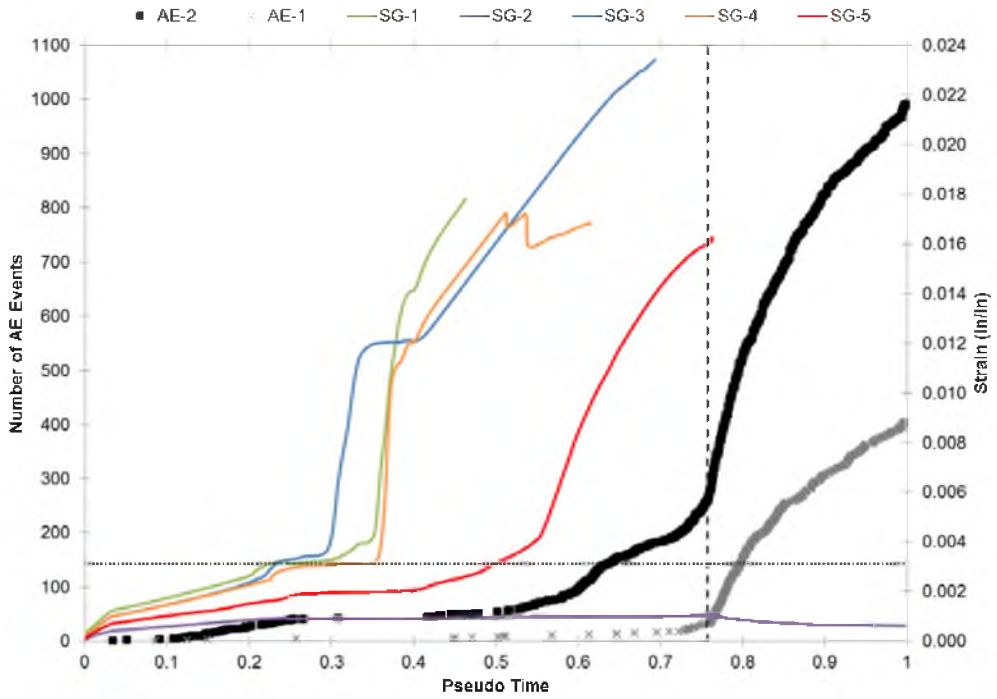

Figure 47. Lenton-4-S AE Event History (With Strain)

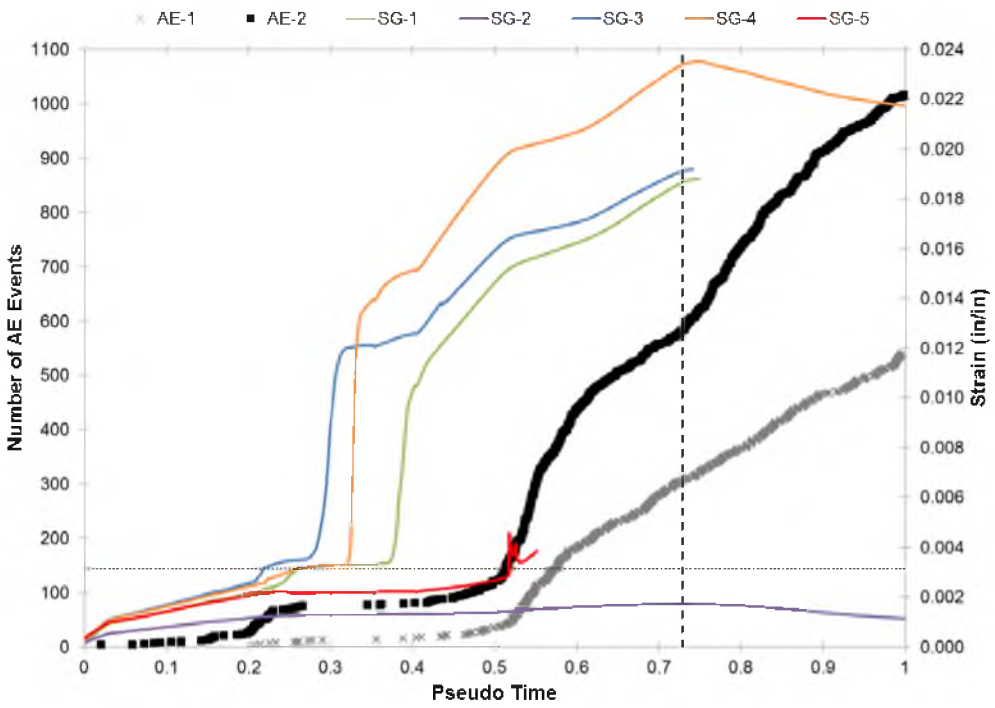

Figure 48. Lenton-5-S AE Event History (With Strain)

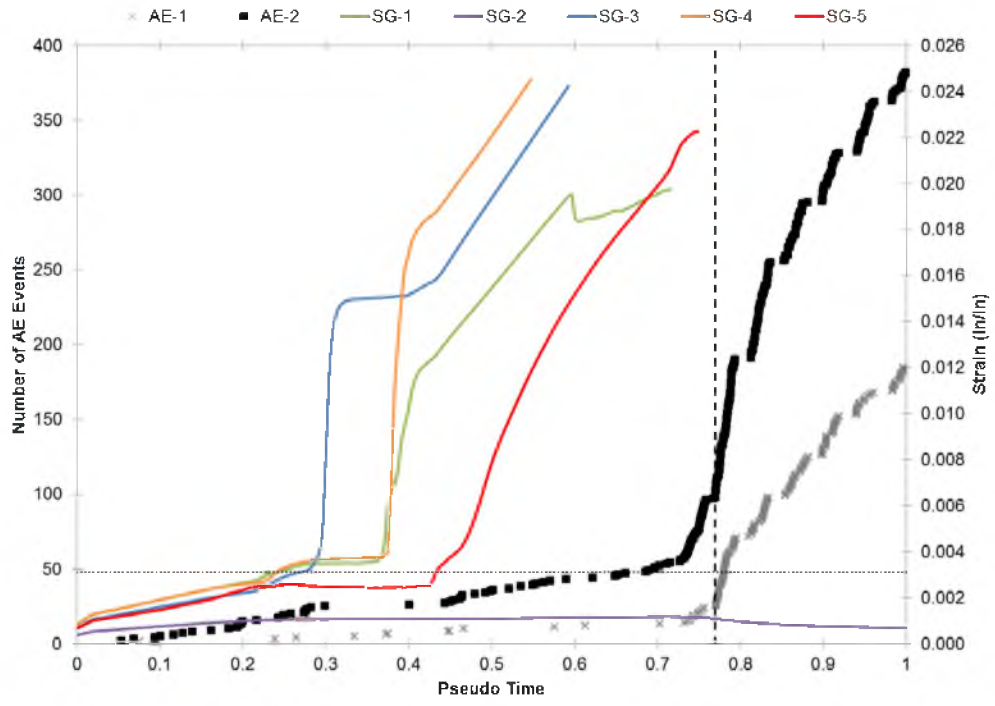

Figure 49. Lenton-6-F AE Event History (With Strain)

out, but the load keeps increasing in this case. In the case of Lenton-5-S, it appears that the field dowel began to slip at the pseudo time of 0.5, but was still able to resist some additional load until it ultimately failed at the pseudo time of 0.73.

Figure 50 shows a comparison of the number of AE events at the time of failure for each AE sensor. From this figure, it can be seen that there are similarities between the total number of AE events for Lenton-1-F, Lenton-2-F, Lenton-3-S, and Lenton-4-S. Lenton-5-S has a larger number of AE events at failure due to the bar slipping before it ultimately failed. If failure of Lenton-5-S is considered to be where the strain gage in the sleeve was lost and where the rate of AE events begins to increase, there would have been 57 AE events on sensor AE-1 and 179 AE events on sensor AE-2; which puts the total number of AE events at failure close to the numbers seen in the other four tests.

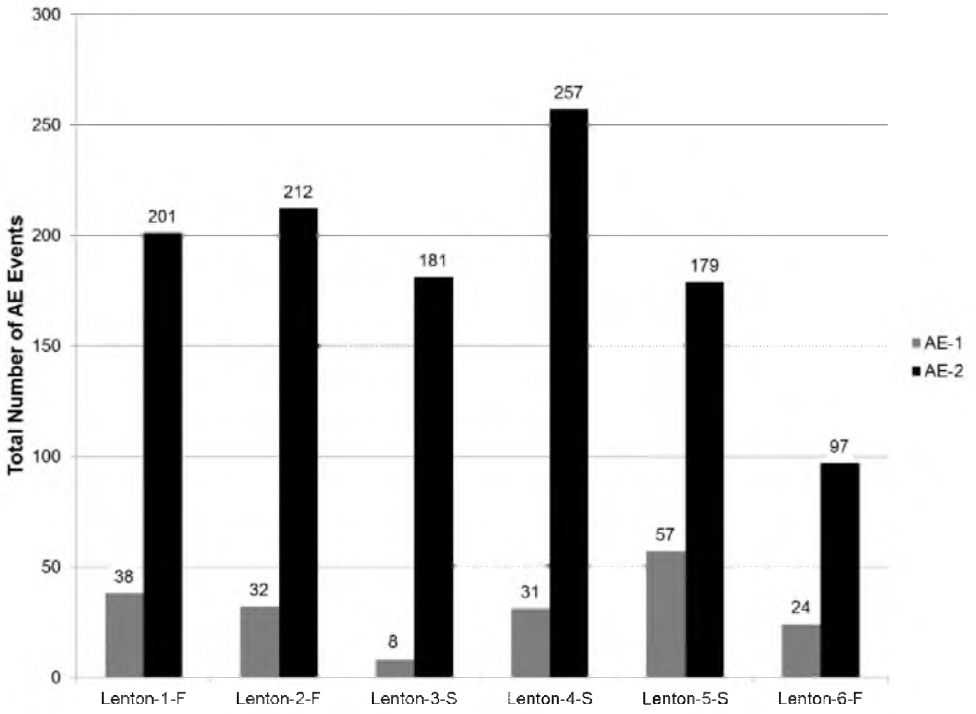

Figure 50. Lenton Interlock AE Events at Failure Comparison

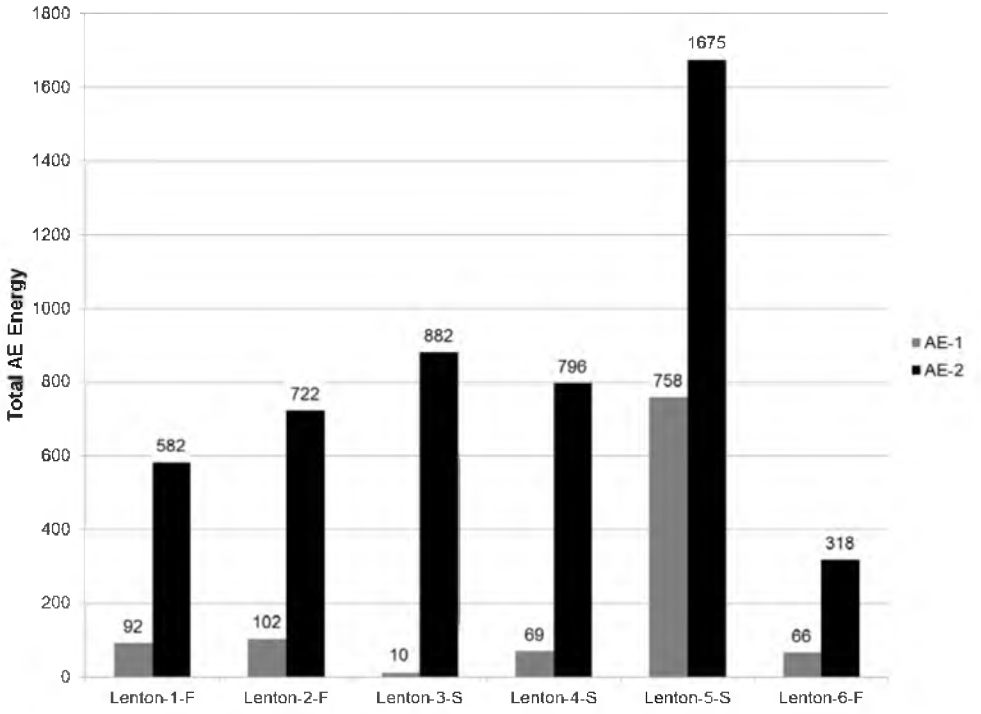

Figure 51. Lenton Interlock AE Energy at Failure Comparison

2.2.4.4 Lenton Interlock Cumulative AE Energy

Figure 51 shows a comparison of the cumulative AE energy at the time of failure for each AE sensor. From this figure, it can be seen that there are similarities between the total AE energy for Lenton-1-F, Lenton-2-F, Lenton-3-S, and Lenton-4-S at the time of failure. If Lenton-5-S is adjusted as stated in the previous section, the AE energy for sensor AE-1 would be 112 and the AE energy for sensor AE-2 would be 435, making it very similar to the other four tests.

2.3 Grouted Splice Sleeve Tension Test Summary

All six of the NMB splice sleeve tension tests resulted in fracture of the bars while resisting no less than 164 percent of the nominal yield strength of the bars. As the sleeves were loaded to failure, there was necking of the bar into the SS mortar on both ends of the sleeve. On the field dowel end, the necking depth ranged from 1/2 in. – 3/4 in. and on the factory dowel end, the necking depth ranged from 1/4 in. – 1/2 in. Reviewing the AE data for the NMB splice sleeves revealed that as the load plateaus near the maximum load, the rate at which the AE events occur

decreases drastically. This decrease in the rate of AE events could be used to identify that failure of the bar is imminent.

All six of the Lenton interlock splice sleeve tension tests resulted in the field dowel being pulled out of the HY10L grout while resisting no less than 137 percent of the nominal yield strength of the bars. Reviewing the AE data for the Lenton Interlock splice sleeves revealed that as the bar began to be pulled out, the rate at which the AE events occurred increased drastically. This increase in the rate of AE events could be used to identify that failure of the sleeve has occurred and the bar is being pulled out. Also, reviewing the total number of AE events and the total AE energy at failure, it was found that all of the sleeves had similar results.

CHAPTER 3

AE MONITORING ASSESSMENT OF PRECAST RC BRIDGE COLUMNS WITH GROUTED SPLICE SLEEVE CONNECTIONS

The AE monitoring system was implemented on two precast reinforced concrete (RC) bridge column specimens with different grouted splice sleeve systems that were subjected to quasi-static cyclic loading. An AE monitoring assessment is then performed on both RC column specimens in an attempt to correlate AE with damage in the column.

3.1 Precast RC Bridge Column Test Setup

Two precast reinforced concrete (RC) bridge column test specimens with different grouted splice sleeve systems were tested under quasi-static cyclic loads. One precast RC bridged column specimen utilized NMB grouted splice sleeves and was used to connect a RC footing and a RC column. This specimen is denoted as FCNMB-1 and the connection details are shown in Figure 52 (*6*). The second precast RC bridged column specimen utilized Lenton Interlock grouted splice sleeves and was used to connect a RC bridge pier cap to a RC column. This specimen is denoted as PCLEN-1 and the connection details are shown in Figure 53 (*6*). Both RC bridge column specimens were designed to simulate typical prototype bridges constructed in Utah, following the 2012 AASHTO LRFD Bridge Design Specifications (19), and the 2011 AASHTO Guide Specifications for LRFD Seismic Bridge Design (20), in accordance with capacity-based design procedures (*6*). The circular configuration of column longitudinal bars and the octagonal column cross-section is the method of choice for accelerated bridge

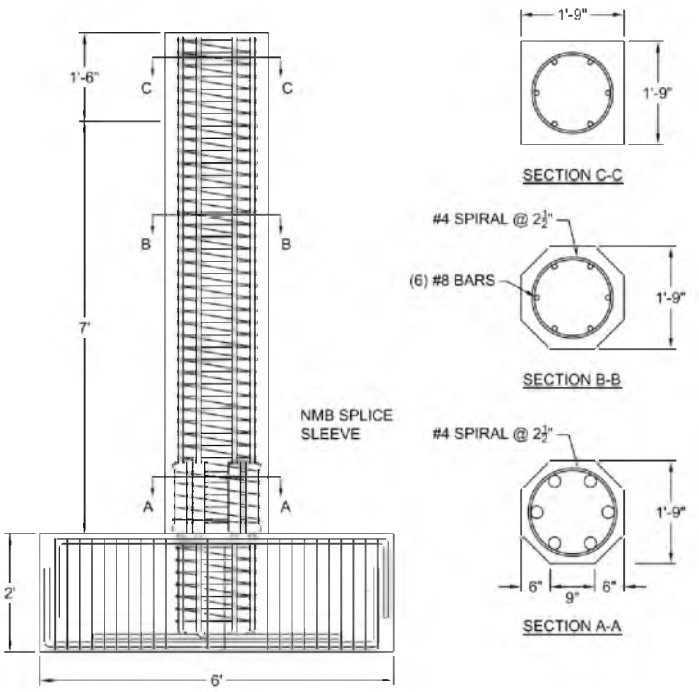

Figure 52. FCNMB-1 Connection Details. Data From (*6*)

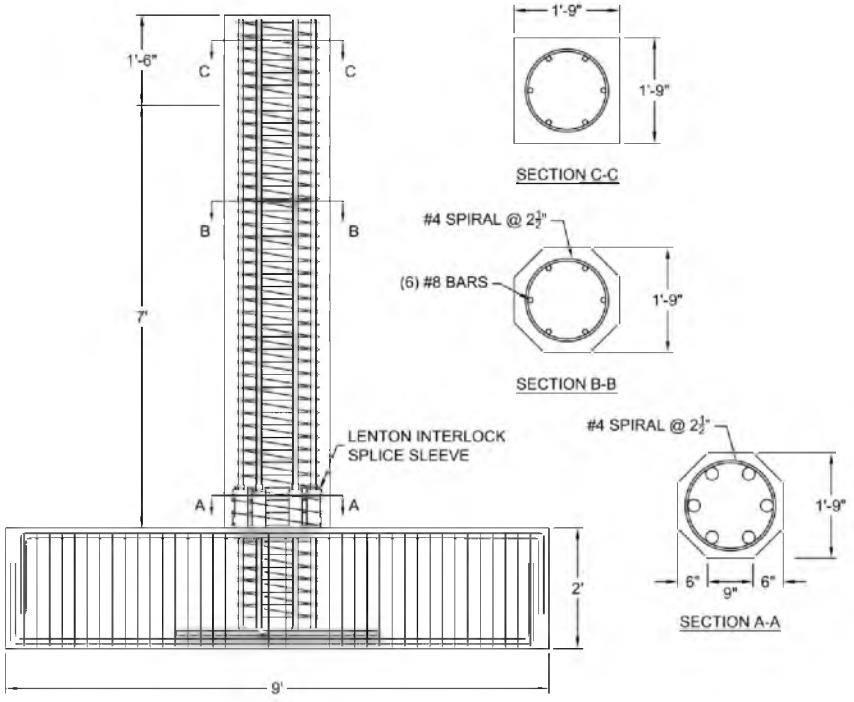

Figure 53. PCLEN-1 Connection Details. Data From (*6*)

construction methods in Utah.

3.1.1 Precast RC Bridge Column Test Procedure

In order to replicate the loading conditions that the precast RC bridge columns would experience during a seismic event, the specimens were installed in the testing apparatuses shown in Figure 54 and Figure 55 for FCNMB-1 and PCLEN-1, respectively. In both cases, all the connections between the test specimen and the testing apparatus were pinned. The ends of the footing and pier cap were fixed to the strong floor to prevent horizontal and vertical translations of the assemblies. A displacement controlled actuator was pinned to the top of the column from the reaction frame in order to apply quasi-static cyclic displacements.

Prior to applying the cyclic displacements, a constant axial load on the columns was simulated by means of two threaded rods along with a 500-kip actuator. The magnitude of axial load corresponded to 6 percent of the axial load capacity of the column. For both test specimens, this translates to a constant axial load of 110 kips.

Cyclic quasi-static horizontal displacements were induced by a 120-kip servo controlled actuator, following the loading protocol shown in Figure 56. Two cycles per displacement amplitude (drift step) were used and the amplitude was progressively increased until a 20 percent drop in the load was observed. This loading protocol follows the loading history procedure laid out by ACI 374.2-13 (23). Positive displacements of the column correspond to the column being pushed towards the east (i.e., to the right in Figures 54 and 55).

This loading protocol consists of a relatively small number of cycles; half of these cycles exceed the displacement amplitude attained in previous cycles. This results in the majority of the AE records being generated by new damage. This is unlike long-term loads, such as traffic or vibration, that act almost continuously throughout the lifetime of the structure which may cause a large number of cycles at small amplitudes, and cause the structure to respond in an elastic manner. The damage caused by these long-term loads is understood to be a problem of fatigue, and results in the majority of the AE records being generated by friction-based events from existing damage. On the other hand, seismic events generate a low number of cycles and occur

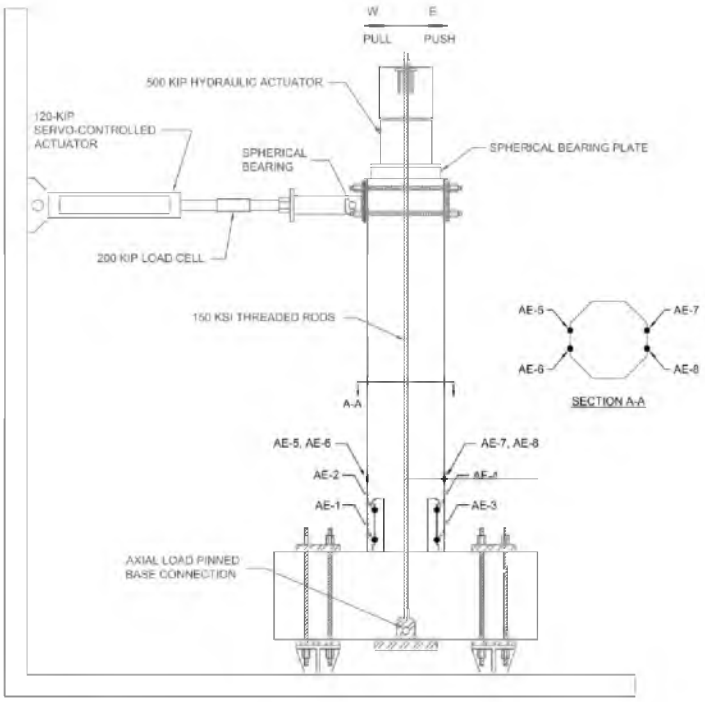

Figure 54. FCNMB-1 Test Setup

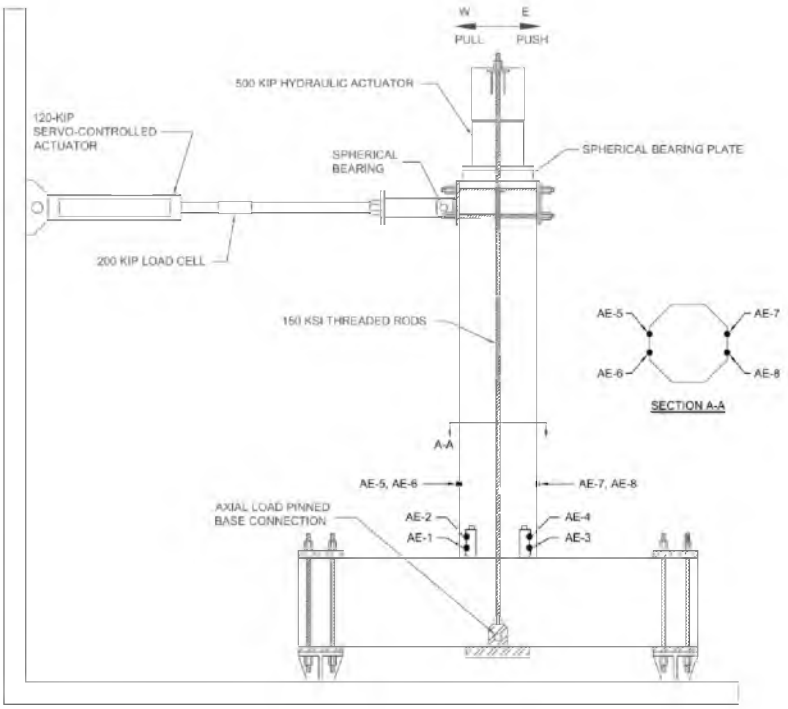

Figure 55. PCLEN-1 Test Setup

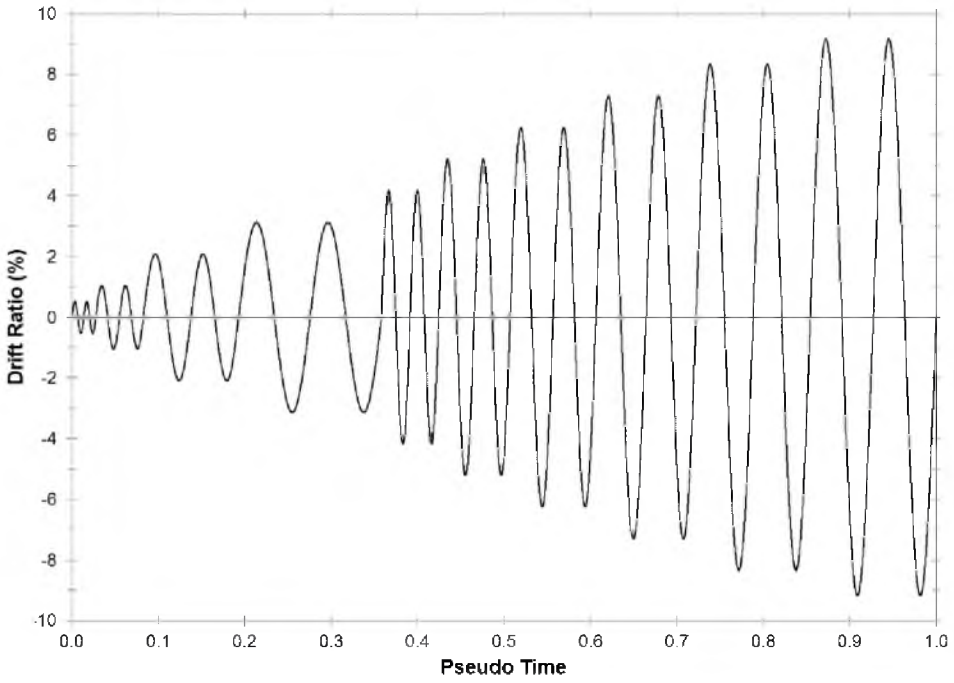

Figure 56. Precast RC Bridge Column Loading Protocol

over a short period of time compared to long-term loads. Moderate and severe seismic events produce plastic deformations, which are responsible for damage to the structure. The accumulation of plastic deformations occurs when the amplitude of a cycle exceeds that of a previous cycle, causing new damage. The AE record generated from the accumulation of plastic deformations is generally associated with the opening and propagation of cracks, as well as crushing of the concrete.

3.1.2 Precast RC Bridge Column AE Sensor Layout

The two RC bridge column assemblies had similar AE sensor layouts. The position of the AE sensors and the number used to identify them is shown in Figures 54 and 55 for FCNMB- 1 and PCLEN-1, respectively. AE sensors AE-1 to AE-4 are film sensors that were placed on the splice sleeves before casting the test specimens in concrete. Unfortunately, however, these four AE sensors did not work during the test. This could have been for a couple of reasons which include water getting into the sensor or the protective coating placed over the sensor affecting its

performance. The fact that these sensors did not work makes it impossible to use the AE characteristics found from the splice sleeve tension tests to determine failure of the splice sleeve connections.

AE sensors AE-5 to AE-8 are ceramic sensors that were located on the extreme east and west faces of the column. Theses sensors were placed 20 in. up the column from the column to footing or pier cap interface to reduce the risk of the concrete spalling off under the sensor. In the following sections, the AE events recorded by sensors AE-5 and AE-6 were combined in order to clarify the amount of AE being generated on the west side of the column. The combination of these two sensors is denoted as AE-W since this will represent the AE events on the west side of the column. The same was done on the east side of the column by combining the AE events recorded by sensors AE-7 and AE-8. The combination of the east side sensors is denoted as AE-E since this will represent the AE events on the east side of the column.

3.1.3 RC Precast Bridge Column Material Properties

Table 8 shows the average material properties for the steel, concrete, and grout used in the test specimens. The steel properties were obtained using ASTM A370-09a (17), the concrete properties were obtained from 4 in. diameter by 8 in. high concrete cylinders following ASTM C39 (24), and the grout properties were obtained using ASTM C109 (18).

Table 8. Precast Bridge Column Material Properties

Specimen	Bar Properties				Concrete Compresive Strength		Grout Compressive Strength	
	Longitudinal (No. 8)		Transverse (No. 4)					
	F_y (ksi)	F_u (ksi)	F_y (ksi)	F_u (ksi)	28-day (ksi)	Test-day (ksi)	28-day (ksi)	Test-day (ksi)
FCNMB-1	68	93	63	103	5.3	5.9	14.4	14.4
PCLEN-1	75	103	63	103	5.3	6.2	12.5	13.3

3.2 FCNMB-1 Damage and AE Monitoring Assessment

3.2.1 FCNMB-1 Hysteresis and Observed Damage

Figure 57 shows the hysteretic response for FCNMB-1 (*6*). The point corresponding to the maximum displacement reached by the first cycle of each drift ratio step is marked by a circle and numbered from 1 to 18. Points 19 and 20 indicate where the extreme column longitudinal bars fractured. Damage was concentrated in two key sections: specifically, the bed grout and the section just above the sleeves. During the first cycles pertaining to points 1 and 2, the first cracks formed at the bed grout section, accompanied by another crack just above the sleeves. By the end of cycles 9 and 10, all major cracks in the column had developed. Spalling started at point 9 and progressed at the corners of the column section. As the test progressed past point 9, the cracks widened and spalling increased. Beginning at cycles 13 and 14, yielding of the field dowel began and resulted in concrete crushing at the top of the footing, adjacent to the column. At points 19 and 20, both extreme longitudinal bars on the west and east side fractured just below the column in the field dowel. Once the bars fractured, the capacity of the column dropped by at least 20 percent, at which point the test was terminated. After completion of the test, it was noticed that the column had twisted about its base. It is not clear at what time this happened since it was not observed during the test.

3.2.2 FCNMB-1 AE Monitoring Assessment

An AE monitoring assessment of FCNMB-1 was performed in order to relate damage of the RC precast bridge column to AE measurements. To perform the assessment, an analysis of the AE event history as well as the cumulative AE energy was performed.

3.2.2.1 AE Event History Assessment

Figure 58 shows the AE event history for the sensors on the west, AE-W, and the sensors on the east, AE-E, with the displacement history superimposed. From Figure 58, it can be seen that the majority of AE events occur within the first half of the test. This can be attributed to the concentration of damage at the column to pier cap interface at the larger displacements.

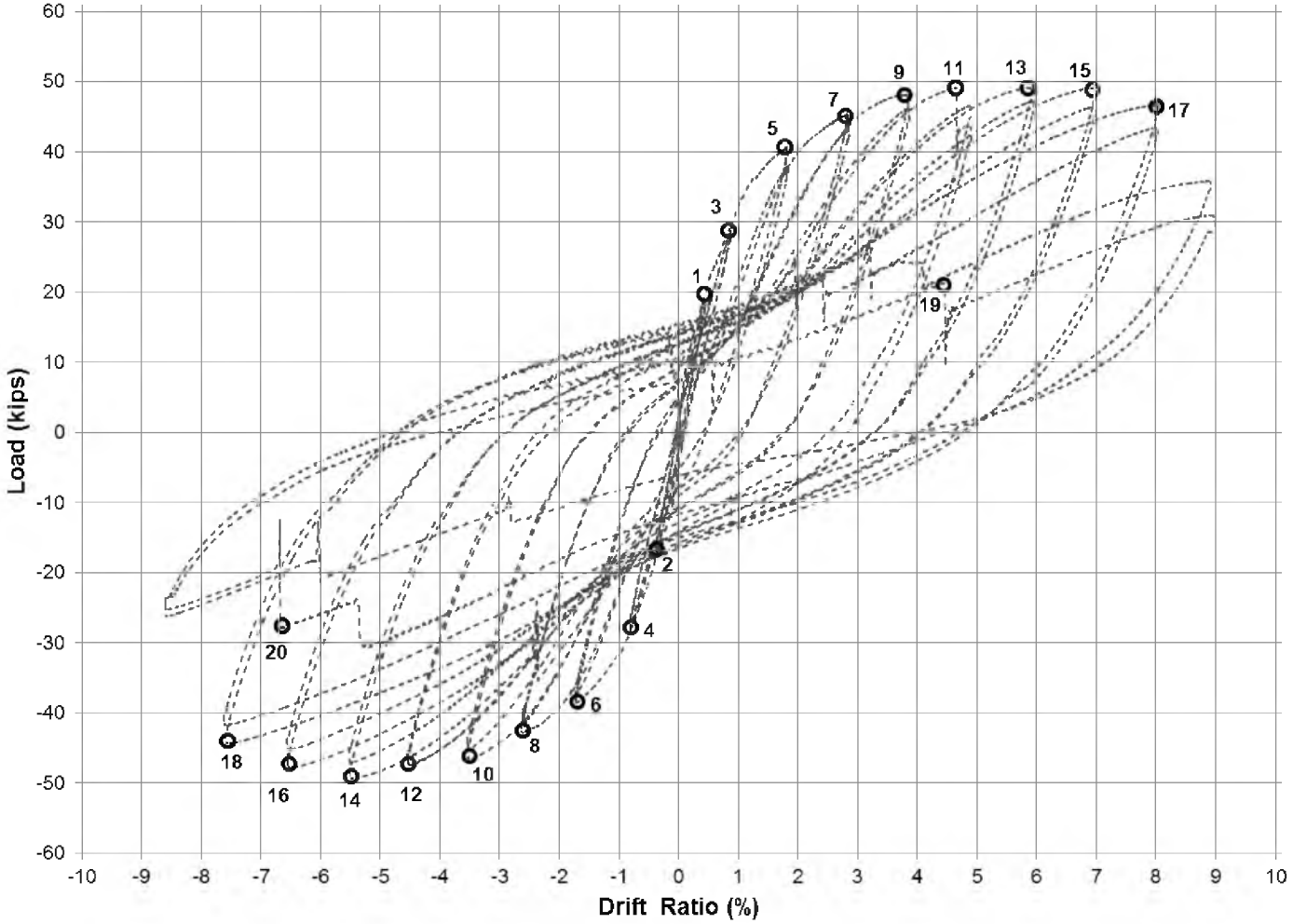

Figure 57. FCNMB-1 Hysteresis. Data From (*6*)

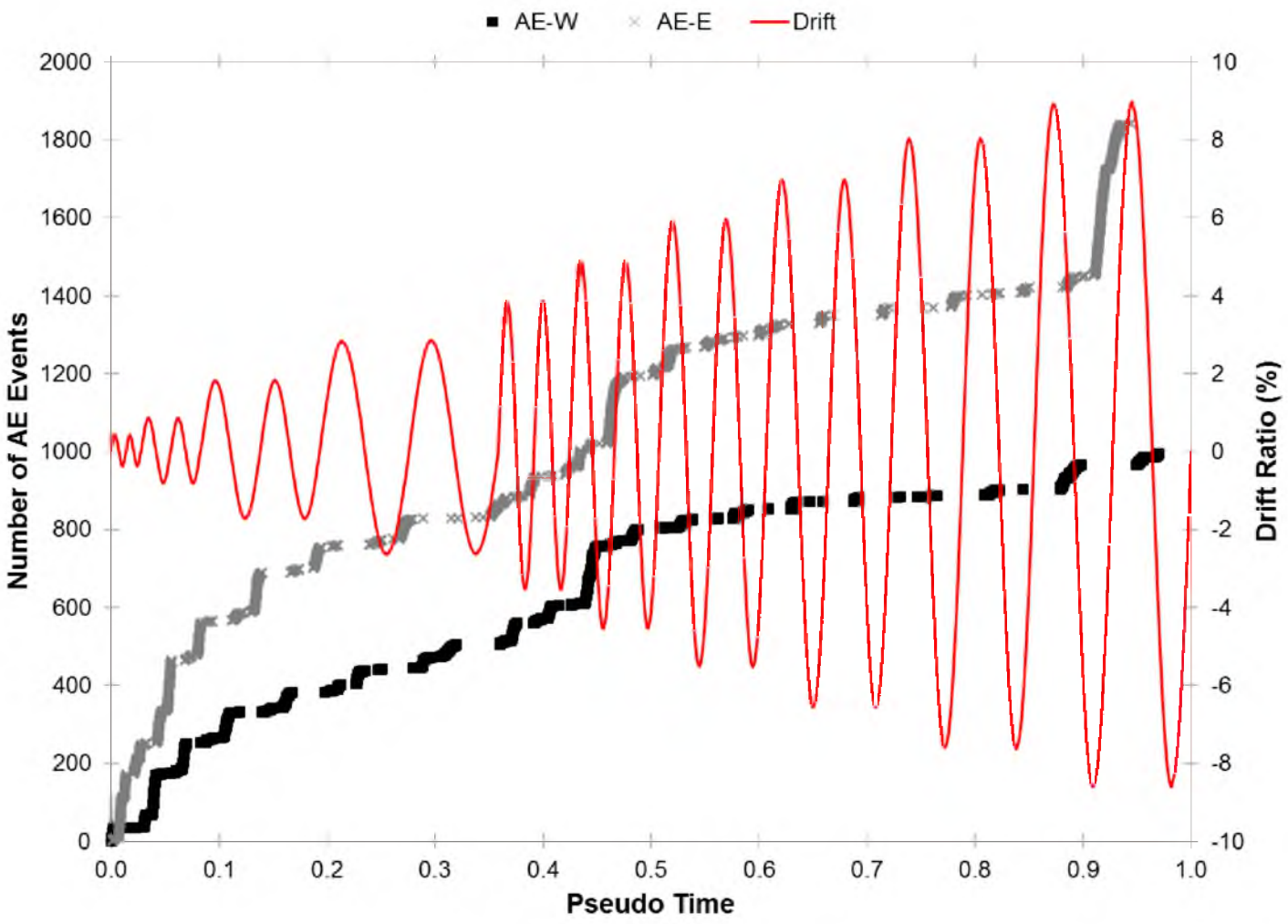

Figure 58. FCNMB-1 AE Event History

This also means that the majority of structural damage to the column due to cracking and crushing of the concrete was completed early in the test and that most of the deformations at the end of the test were resisted mainly by the field dowels in the footing.

Figures 59 to 63 show the AE event history for FCNMB-1 broken up into five sections in order to get a better understanding of when the AE events occur within the cycles. On these plots, the displacement history is superimposed on the AE event history, and includes vertical dashed lines at the maximum and minimum displacements.

Figure 59 shows the AE event history for the cycles corresponding to points 1-4 on the hysteresis. AE events recorded by AE-W begin almost simultaneously with the start of the test and the number of AE events increases until the maximum displacement at point 1 is reached. These events are attributed to the creation and propagation of microcracks on the west side of the column (i.e., a positive displacement puts the west side of the column in tension). As the displacement reaches a maximum at point 1, the number of AE events ceases to increase indicating that the microcracks have stopped propagating. The condition of no increase in the number of AE events remains as the actuator starts to move in the opposite direction which begins to close the cracks with no new cracks opening. As the displacement goes through zero, a similar pattern of behavior exhibited by sensors AE-W is repeated by sensors AE-E. However, once the actuator reaches a maximum displacement at point 2 and starts to move in the opposite direction, there continue to be AE events recorded by sensors AE-E as the cracks are closing. The events in this region most likely come from the friction between the crack interfaces as they close.

As the second of the two cycles begins, there are almost no AE events that occur and the few that do can be attributed to the friction between the existing crack interfaces. Therefore, in the second cycle, there are no new cracks created or growth of existing cracks. As the next set of cycles begins (i.e., as the displacement goes from zero to point 3), there are essentially no AE events, but as the maximum displacement of the previous set of cycles is reached, the number of AE events begins to increase once more. The maximum amplitude of the previous events is denoted by a green line. This delay in AE events can be attributed to the Kaiser effect. The

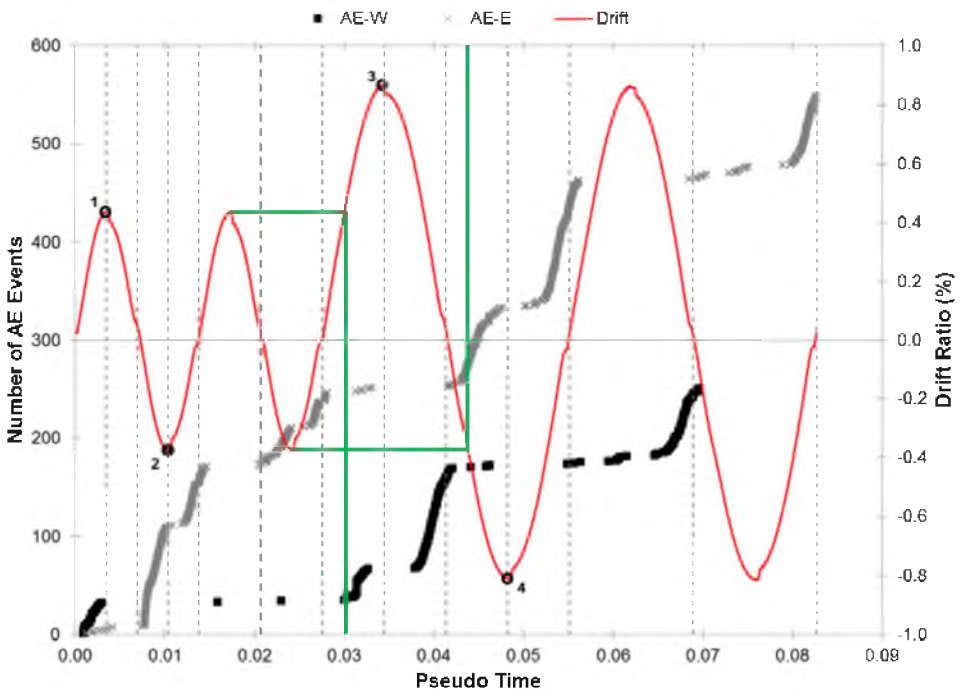

Figure 59. FCNMB-1 AE Event History Points 1-4

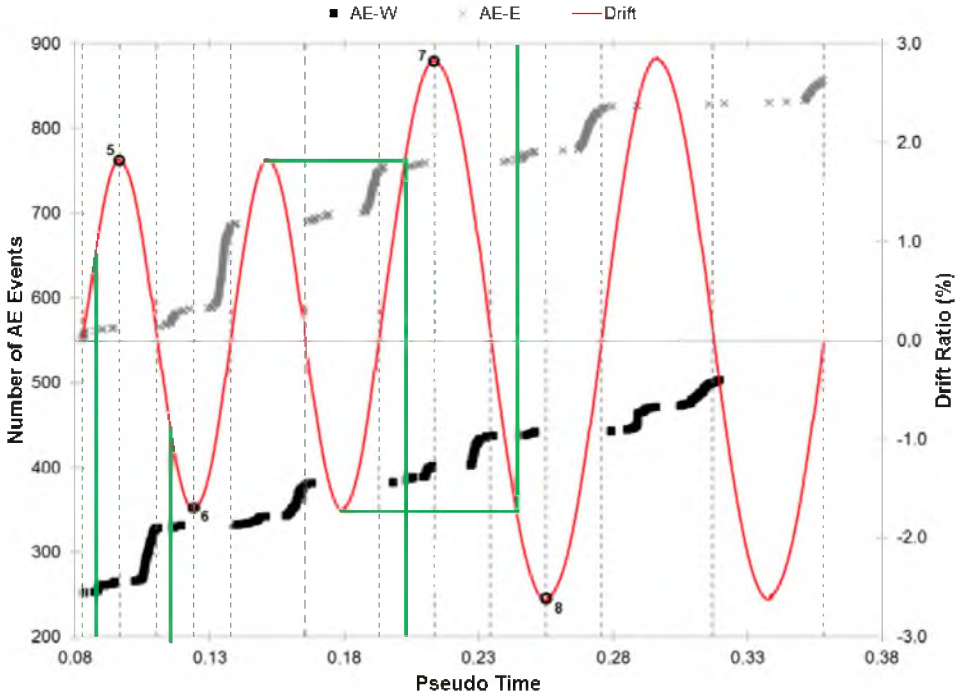

Figure 60. FCNMB-1 AE Event History Points 5-8

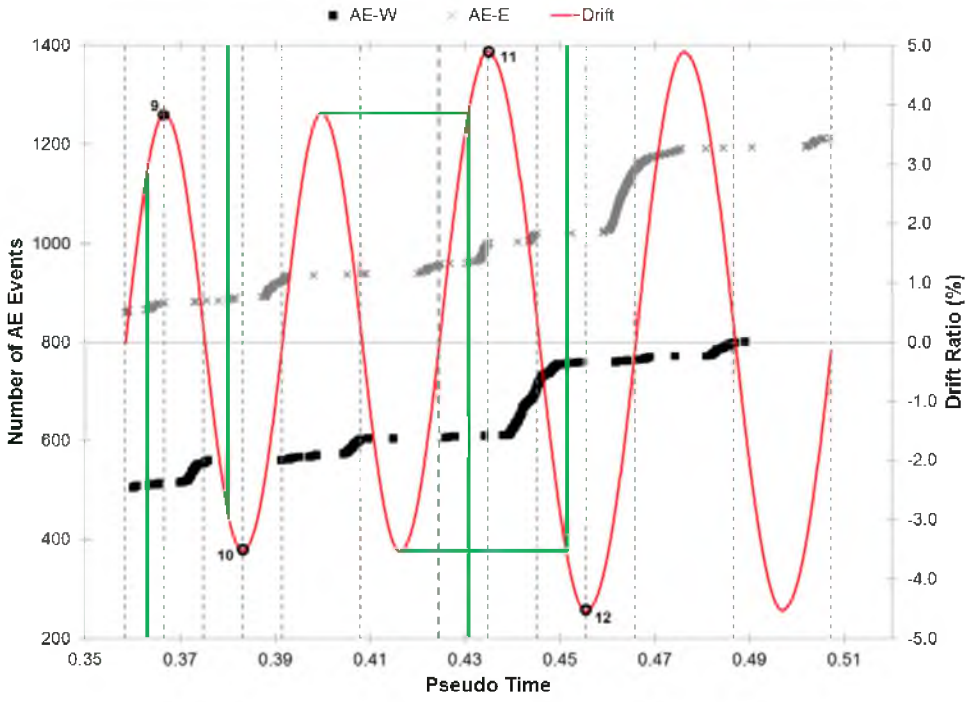

Figure 61. FCNMB-1 AE Event History Points 9-12

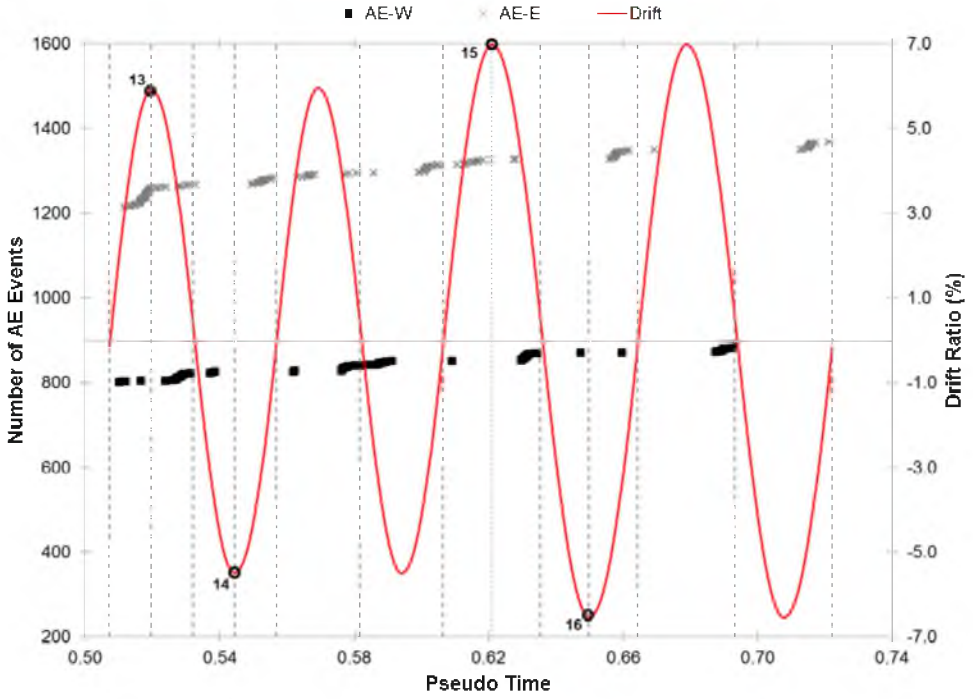

Figure 62. FCNMB-1 AE Event History Points 13-16

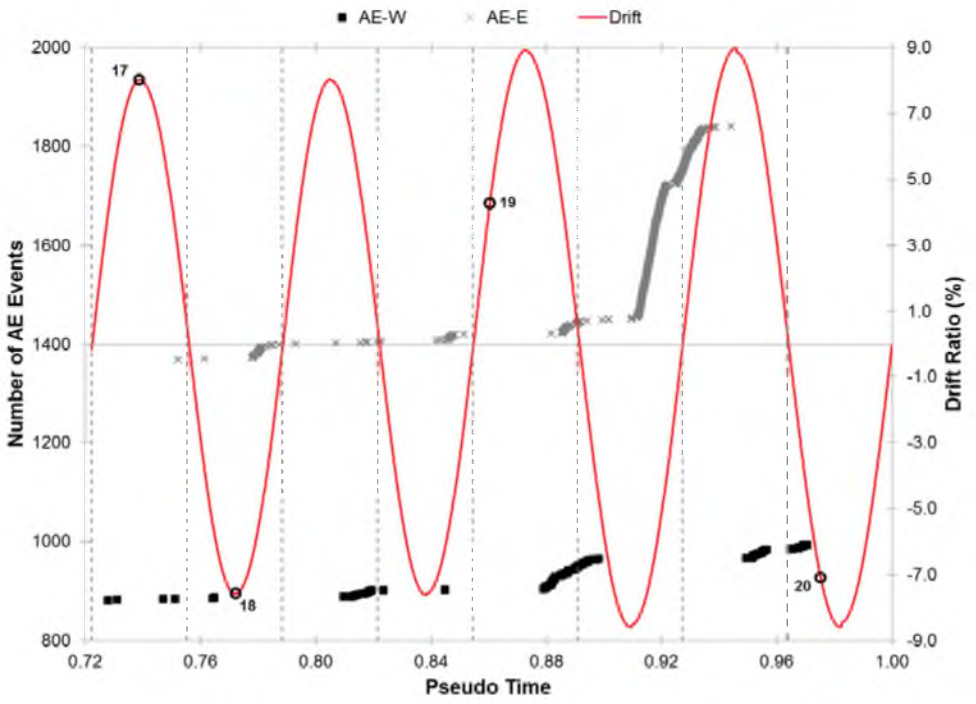

Figure 63. FCNMB-1 AE Event History Points 17-20

increase in the number of AE events is caused by the growth of the existing cracks as well as the formation of new ones. The same patterns noted for points 1 and 2 are also seen for points 3 and 4. The only difference is that the increase in AE events does not occur until the maximum displacement of the previous set of cycles is reached.

Figure 60 shows the AE event history for the cycles corresponding to points 5-8 on the hysteresis. In this figure, the AE events follow a similar pattern as for Figure 59. The main difference is that there is a smaller increase in events as the actuator moves from zero to the maximum displacement for the first time, but as the actuator moves from the maximum displacement to zero, there is a large increase in AE events. The smaller increase in AE events can be explained by the fact that most of the cracks have already opened by this point and only a small amount of propagation occurred in the existing cracks as they widened. The larger increase in AE events as the actuator moves from the maximum displacement to zero is caused by the newly propagated portion of the existing cracks closing and friction is created between these two interfaces causing AE events.

Figure 61 shows the AE event history for the cycles corresponding to points 9-12 on the hysteresis. During the cycles that correspond to points 9 and 10, there were very few AE events, since there was not very much new damage during these cycles. During the cycles corresponding to points 11 and 12, the spherical bearing plate at the top of the column began to stick. As the column was being displaced, the bearing plate would stick as it rotated, causing loud audible noises. During these two cycles, a rapid increase in the number of AE events can be seen in sensors AE-W and AE-E. This rapid increase in AE events is unlikely to be coming from cracks propagating or friction between the crack interfaces. Instead, it can be explained by the external noise created by the spherical bearing plate during these cycles.

Figure 62 and Figure 63 show the AE event history for the cycles corresponding to points 13-20 on the hysteresis. As observed in section 3.2.1, after point 10, all major cracks in the column had developed and instead, the damage was concentrated at the column to footing interface. This is shown in the AE event history by there being very few events after point 12. This fact is described in Figure 64, which shows the number of AE events per drift level. In this figure,

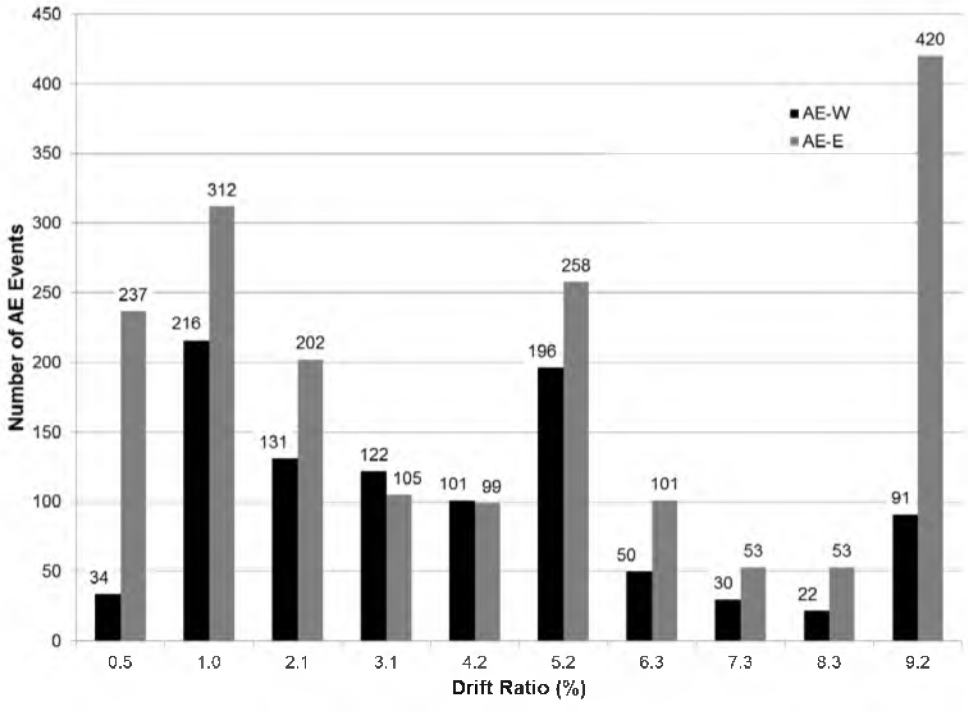

Figure 64. FCNMB-1 Number of AE Events Per Drift Level

there is a noticeable reduction of events at the 5.2 percent drift level which corresponds to points 11 and 12 on the hysteresis. In Figure 63, there is a very large increase of AE events recorded by sensor AE-E during the last two cycles. The point at which the AE events begin to rapidly increase could be related to where the column begins to rotate about its base.

3.2.2.2 Cumulative AE Energy Assessment

Figure 65 shows the cumulative AE energy for the sensors on the west, AE-W, and the sensors on the east, AE-E, with the displacement history superimposed. Similar to the AE event history, the majority of the cumulative AE energy occurred within the first half of the test. From Figure 65, there are two areas where most of the AE energy is released. There was substantial AE energy released during the first two drift levels as well as at a drift level of 4 percent.

Benaven-Climent et al. (*16*) suggest that for monolithic beam column joints, there is a strong correlation between structural damage expressed in terms of hysteretic energy and the cumulative AE energy. To enable this comparison, both the AE energy and hysteretic energy are normalized by their respective value at the end of the test. Figure 66 shows the comparison between the normalized cumulative AE energy and the normalized hysteretic energy. From this figure, it can be seen that the normalized cumulative AE energy accumulates at the beginning of the test while the hysteretic energy accumulates at the end of the test. This completely opposite response in energy dissipation can be attributed to the behavior of the column during the test. After the first couple of cycles, damage did not accumulate in the column. The damage instead was accumulated in the field dowels at the top of the footing. This behavior is different from that of monolithic joints, in which AE and hysteretic energy closely relate to one another due to the spreading of plastic deformations in the column.

3.3 PCLEN-1 Damage and AE Monitoring Assessment

3.3.1 PCLEN-1 Hysteresis and Observed Damage

Figure 67 shows the hysteretic response for PCLEN-1 (*6*). The point corresponding to the maximum displacement reached in the first cycle of each drift ratio set is marked by a circle and

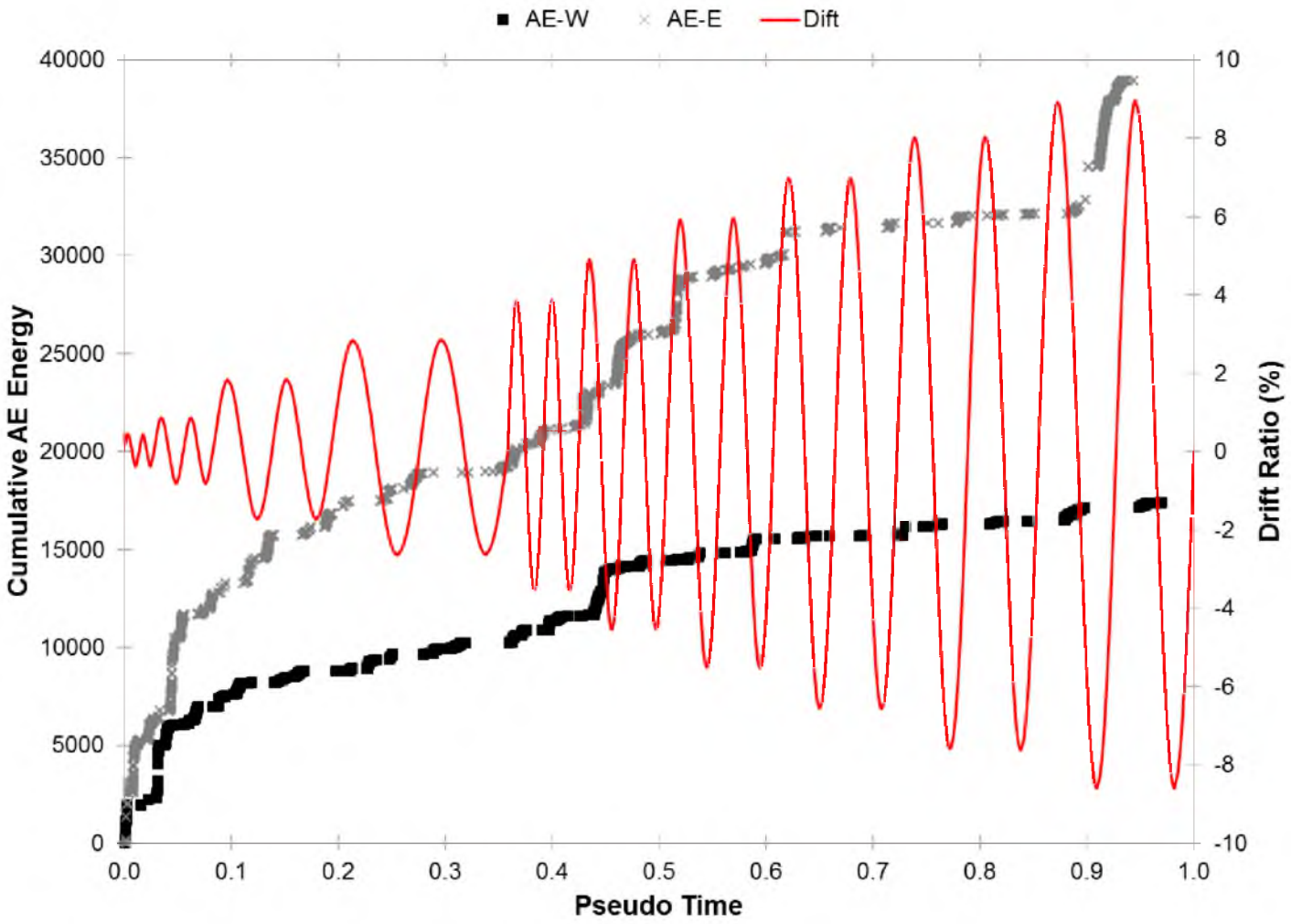

Figure 65. FCNMB-1 Cumulative AE Energy

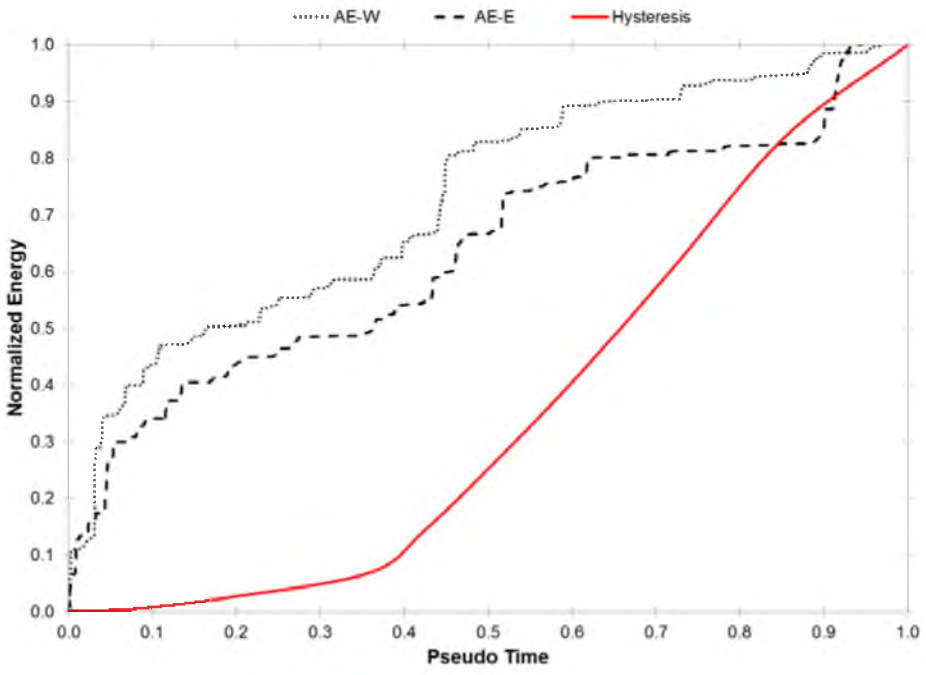

Figure 66. FCNMB-1 Comparison of Normalized Cumulative AE Energy and Normalized Hysteretic Strain Energy

numbered from 1 to 12. Points 13 and 14 mark where the extreme column longitudinal bars began to pull out. Damage was concentrated in two key sections: specifically, the bed grout and the section just above the sleeves. During the cycles pertaining to points 1 and 2, the first crack formed at the bed grout section, accompanied by another crack just above the sleeves. By the end of cycles 7 and 8, all of the major cracks in the column had developed. Spalling started at point 7 and progressed at the corners of the column section. After point 8, it was noted that the damage in the column was localized to the column to pier cap interface. At points 11 and 12, both extreme longitudinal bars on the west and east side began to pull out. Once the bars pulled out, the capacity of the column dropped by at least 20 percent, after which the test was terminated.

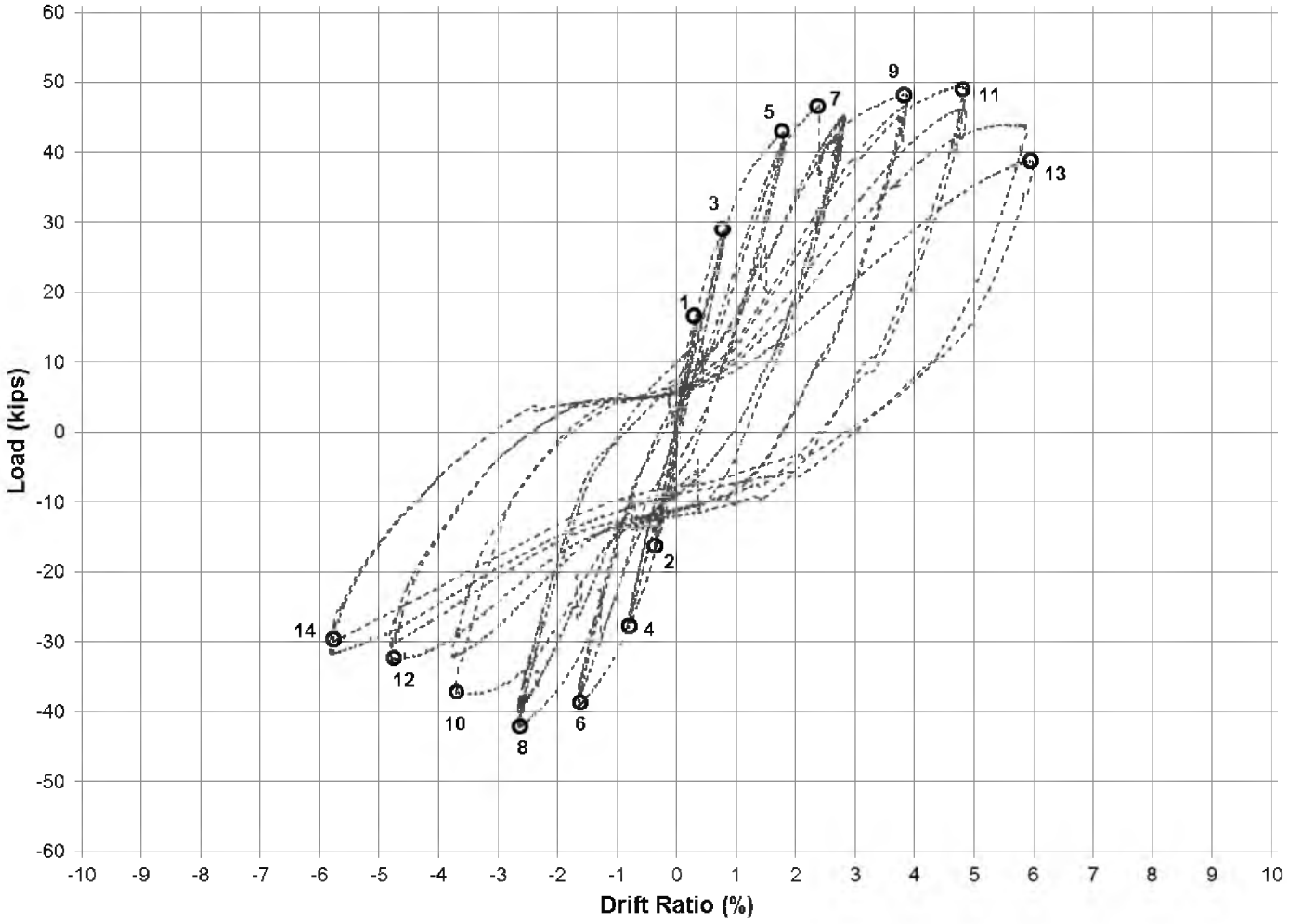

Figure 67. PCLEN-1 Hysteresis. Data From (6)

3.3.2 PCLEN-1 AE Monitoring Assessment

An AE monitoring assessment of PCLEN-1 was performed in order to relate damage of the RC precast bridge column to AE measurements. To perform the assessment, an analysis of the AE event history as well as the cumulative AE energy was performed.

3.3.2.1 AE Event History Assessment

Figure 68 shows the AE event history for the sensors on the west, AE-W, and the sensors on the east, AE-E, with the displacement history superimposed. From Figure 68, it can be seen that the majority of AE Events occurred within the first half of the test. This can be attributed to the damage being localized at the column to pier cap interface. This also means that the majority of the structural damage to the column due to cracking of the concrete occurred early in the test and that most of the deformations at the end of the test were mainly resisted by the field dowels in the pier cap.

Figures 69 to 71 show the AE event history for PCLEN-1 broken up into three sections. On these plots, the displacement history is superimposed on the AE event history, and includes vertical dashed lines at the maximum and minimum displacements. Figure 69 shows the AE event history for the cycles corresponding to points 1-4 on the hysteresis. In Figure 69, AE events recorded by sensors AE-W begin almost simultaneously with the start of the test and the number of AE events increases rapidly until the maximum displacement at point 1 is reached. These events are attributed to the propagation of microcracks on the western side of the column (i.e., a positive displacement places the west side of the column in tension). As the displacement reaches a maximum at point 1, the number of AE events ceases to increase indicating that the microcracks have stopped propagating. The condition of no increase in the number of AE events remains as the actuator starts to move in the opposite direction which begins to close the cracks with no new cracks opening. There are, however, a few AE events that are recorded by sensors AE-W as the cracks are closing. The events in this region come from the friction between the crack interfaces as they close. As the displacement goes through zero, the previous pattern of behavior exhibited by sensors AE-W is repeated by sensors AE-E. As the second of the two

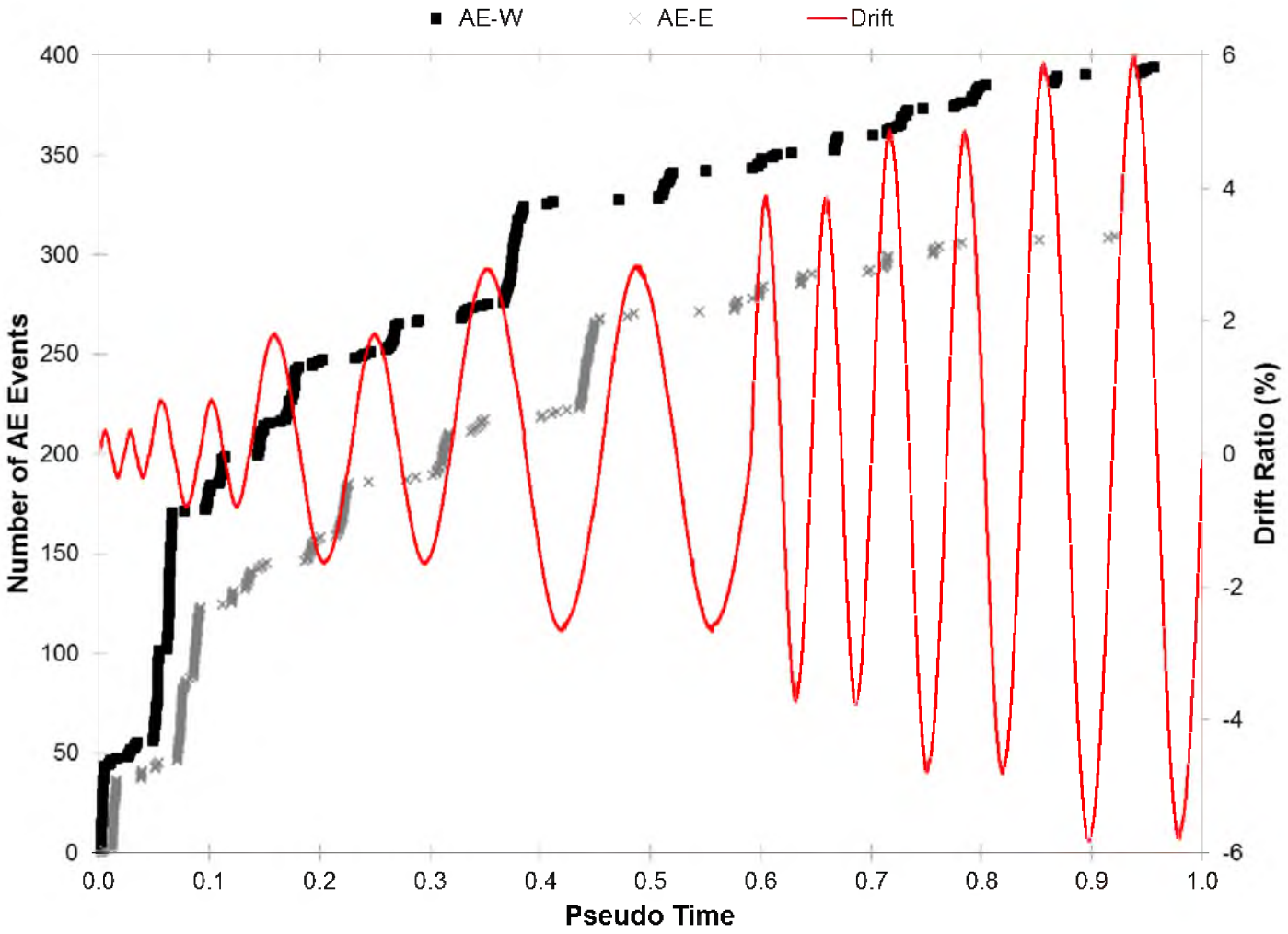

Figure 68. PCLEN-1 AE Event History

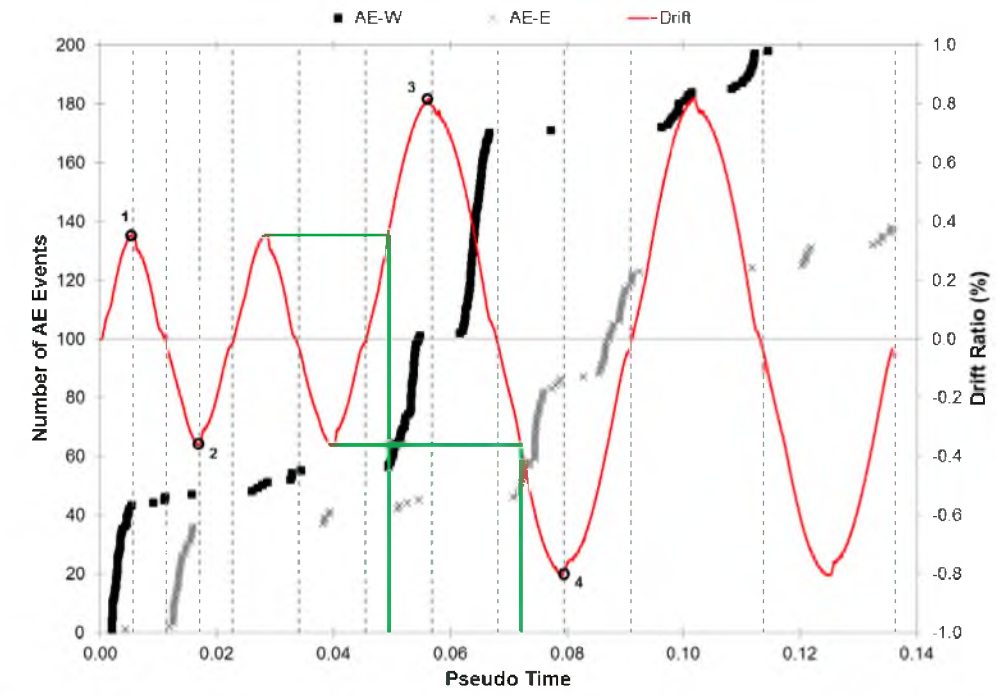

Figure 69. PCLEN-1 AE Event History Points 1-4

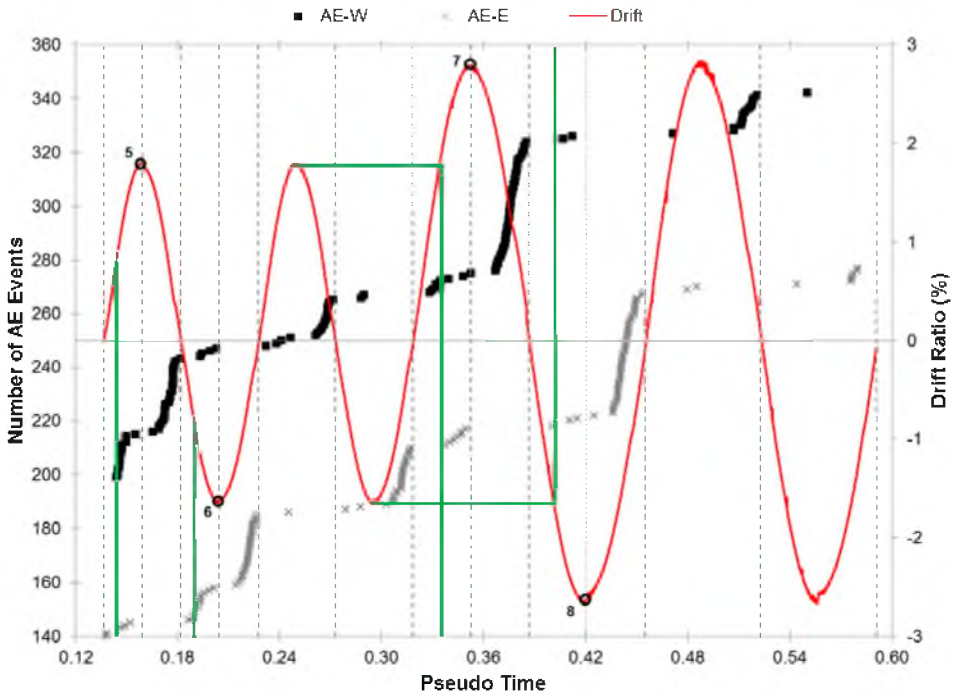

Figure 70. PCLEN-1 AE Event History Points 5-8

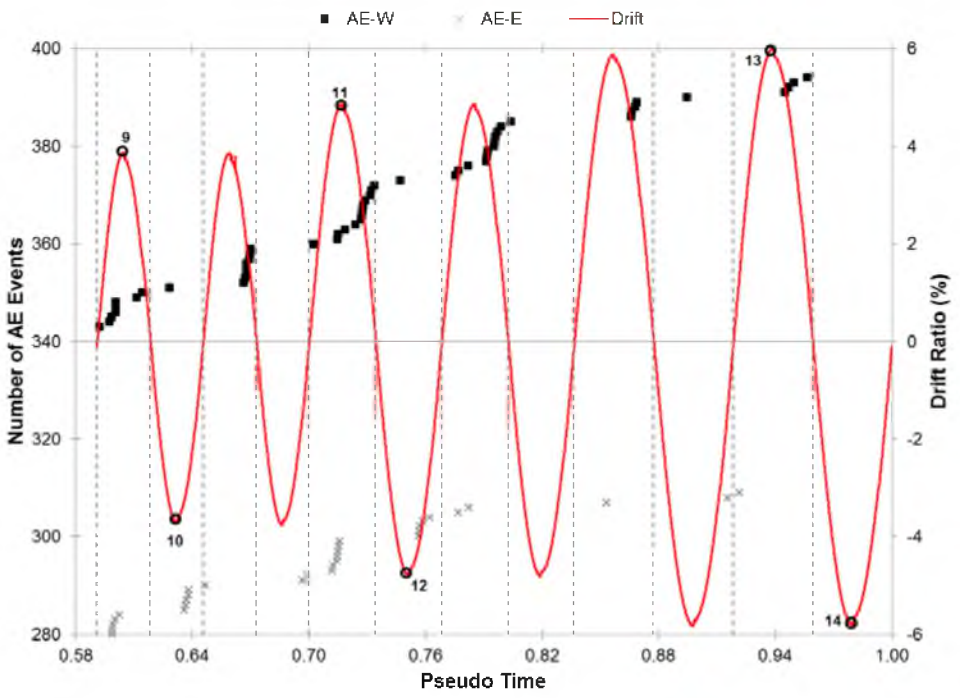

Figure 71. PCLEN-1 AE Event History Points 9-14

cycles begins, there are almost no AE events that occur and the few that do can be attributed to the friction between the existing crack interfaces. Therefore, in the second cycle, there are no new cracks created or growth of existing cracks.

As the next set of cycles begins (i.e., as the displacement goes from zero to point 3) there are essentially no AE events, but as the maximum displacement of the previous set of cycles is reached, the number of AE events begins to increase rapidly once more. The maximum amplitude of the previous events is denoted by a green line. This delay in events can be attributed to the Kaiser effect. The increase in the number of AE events is caused by the growth of the existing cracks as well as the formation of new ones. The same patterns noted for points 1 and 2 are also observed for points 3 and 4. The only difference is that the increase in AE events does not occur until the maximum displacement of the previous set of cycles is reached.

Figure 70 shows the AE event history for the cycles corresponding to points 5-8 on the hysteresis. In this figure, the AE events follow a similar pattern as mentioned before for Figure 69. The main difference is that there is a smaller increase in events as the specimen reaches a

displacement for the first time. The smaller increase in AE events can be explained by the fact that most of the cracks have already opened by this point and only a small amount of propagation of the existing cracks occurred as they widened.

Figure 71 shows the AE event history for the cycles corresponding to points 9-14 on the hysteresis. As mentioned in section 3.3.1, after point 8, the major cracks in the column had already developed and the damage was concentrated at the column to pier cap interface. This is shown in the AE event history as evidenced by very few events beyond this point. This fact is demonstrated in Figure 72, which shows the number of AE events per drift level. In this figure, there is a noticeable drop of events at the 4.2 percent drift level which corresponds to points 9 and 10 on the hysteresis.

3.3.2.2 Cumulative AE Energy Assessment

Figure 73 shows the cumulative AE energy for the sensors on the west, AE-W, and the sensors on the east, AE-E, with the displacement history superimposed. Similar to the AE event

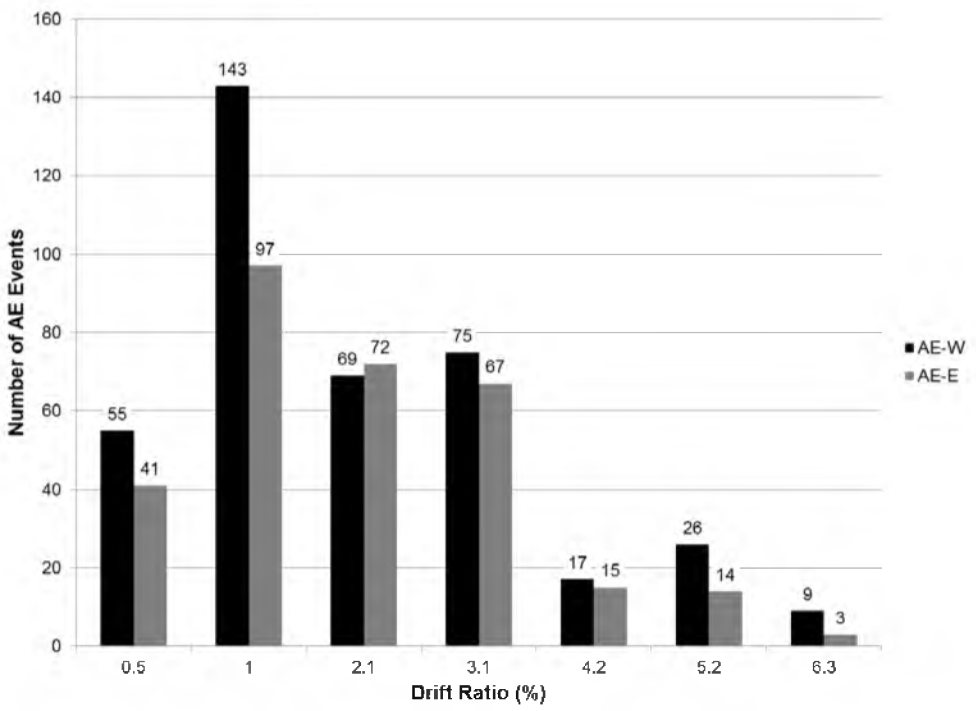

Figure 72. PCLEN-1 Number of AE Events per Drift Level

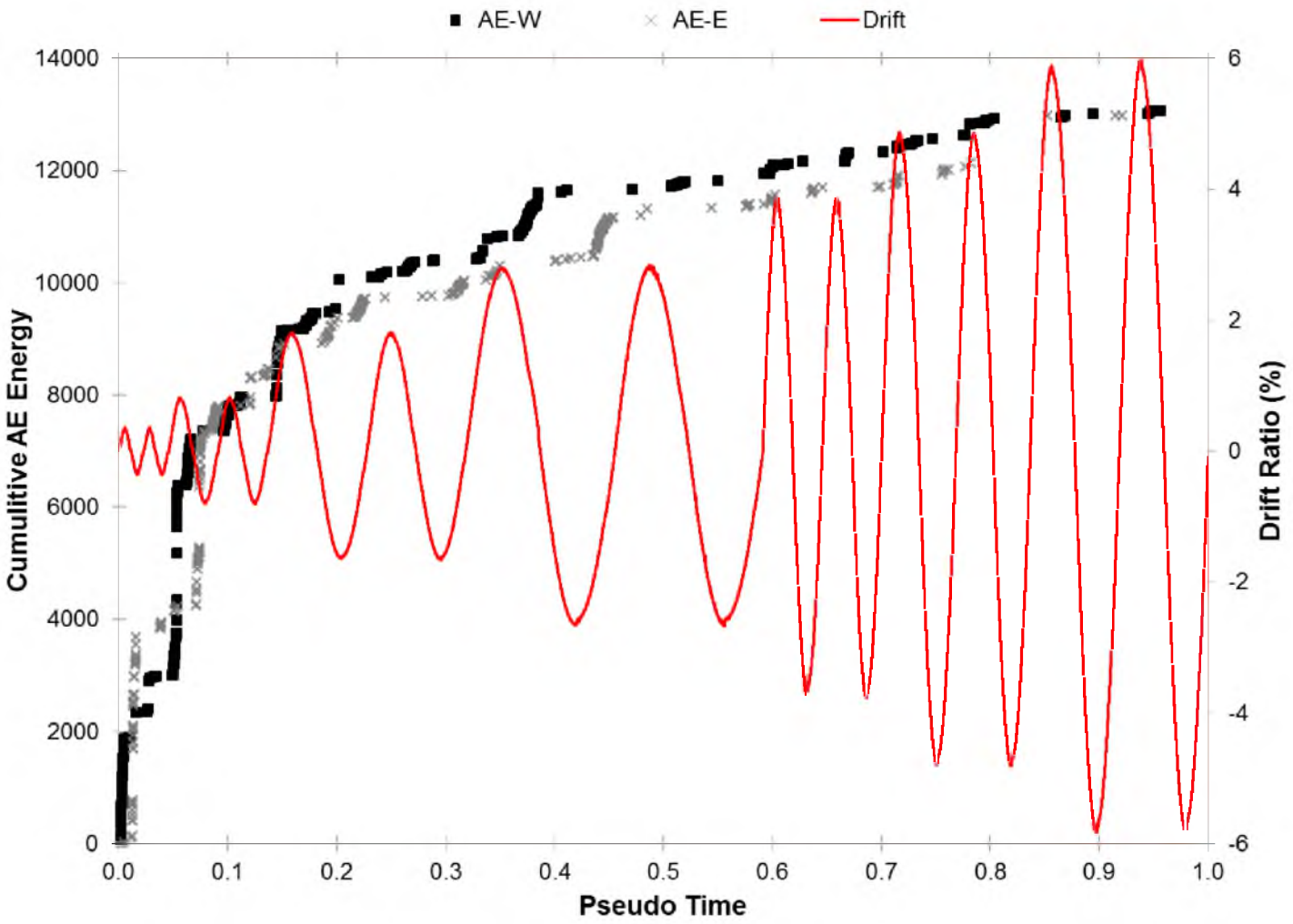

Figure 73. PCLEN-1 Cumulative AE Energy

history, the majority of the cumulative AE energy occurred within the first half of the test. The AE energy and hysteretic energy are normalized by their respective value at the end of the test. Figure 74 shows the comparison between the normalized cumulative AE energy and the normalized hysteretic energy. From this figure, it is observed that normalized cumulative AE energy accumulates at the begging of the test while the hysteretic strain energy accumulates at the end of the test. This completely opposite response in energy can be attributed to the behavior of the column during the test. After the first few cycles, the damage was localized at the column to pier cap interface and plastic deformations did not spread in the column.

3.3.3 AE Monitoring Assessment Summary

In both FCNMB-1 and PCLEN-1, the AE event history and cumulative AE energy showed that the majority of the damage to the column cross-section came early on in the test. This is consistent to what was observed. The reason damage did not accumulate in the column at the

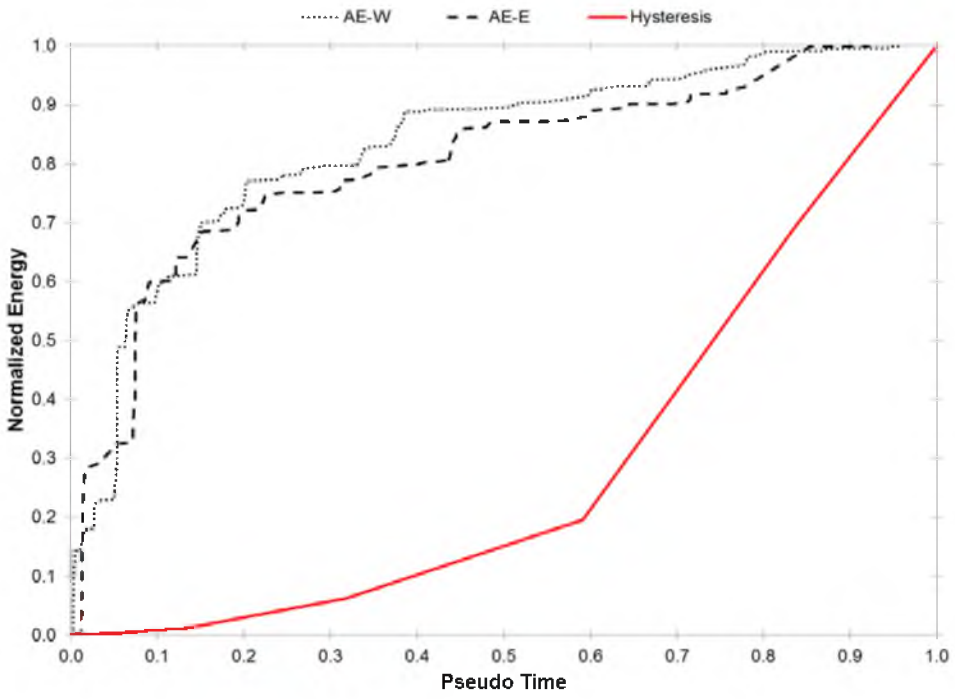

Figure 74. PCLEN-1 Comparison of Normalized Cumulative AE Energy and Normalized Hysteretic Strain Energy

end of the tests is because, instead of damage accumulating in the column, the damage was forced just below the column to the column and footing or pier cap interface. This conclusion is supported by the decline of AE events in the column as well as observations made during testing.

The normalized cumulative AE energy was compared to the normalized hysteretic energy for both specimens. According to Benaven-Climent et al. (*16*), there is a strong correlation between these two in monolithic beam column joints. In the case of FCNMB-1 and PCLEN-1, there was not a strong correlation. This is mainly due to the fact that the column was not the critical section allowing plastic deformations to form and spread. Instead, the damage was localized between the column and footing or pier cap interface, thus not causing any AE events in the column itself where the AE instruments were located.

CHAPTER 4

REPAIR OF PRECAST RC BRIDGE COLUMN TO PIER CAP CONNECTION WITH AE MONITORING ASSESSMENT

4.1 Repair of Precast Column to Pier Cap Connection

Precast RC bridge elements with grouted splice sleeve connections are a popular choice for accelerated bridge construction (ABC). In the aftermath of an earthquake, the option of repairing damaged bridge column elements is a good alternative compared to the high cost and social impact of complete replacement. Recent studies have shown that precast RC bridge components with grouted splice sleeve connections exhibit localized damage, making them excellent candidates for repair.

4.1.1 Original Test Specimen PCLEN-2

Before a repair was performed, an undamaged precast RC test specimen with a grouted splice sleeve connection was tested under quasi-static cyclic loads to induce damage. This test specimen is denoted as PCLEN-2, and is very similar to PCLEN-1 except that the splice sleeves are located in the bridge pier cap instead of the column. The connection details for PCLEN-2 are shown in Figure 75 and the material properties are listed in Table 9 (*6*).

To induce damage to PCLEN-2, the same loading protocol (Figure 56) and test setup (Figure 55) for PCLEN-1 was used along with a simulated axial load of 104 kips. At a drift level of 3.8 percent, a maximum lateral load of 34.73 kips was reached. At a drift level of 6.4 percent, the extreme west longitudinal bar in the column fractured, causing a 20 percent drop in the lateral load capacity after which the test was terminated.

In order to properly design a repair for PCLEN-2, an accurate assessment of the damage

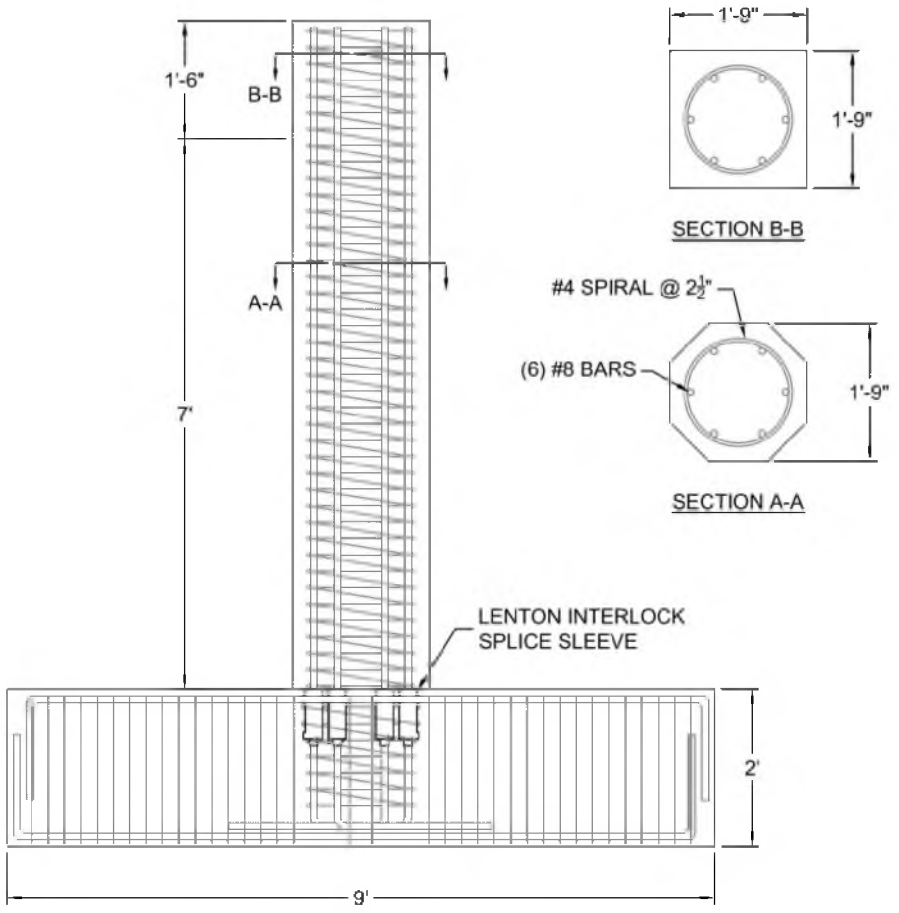

Figure 75. PCLEN-2 Connection Details. Data From (*6*)

Table 9. PCLEN-2 Material Properties. Data From (*6*)

Bar Properties				Concrete Compresive Strength		Grout Compressive Strength	
Longitudinal (No. 8)		Transverse (No. 4)					
F_y (ksi)	F_u (ksi)	F_y (ksi)	F_u (ksi)	28-day (ksi)	Test-day (ksi)	28-day (ksi)	Test-day (ksi)
68	93	63	103	3.9	6.0	10.3	10.3

at the end of the test was performed. Figures 76 to 80 show the damage to PCLEN-2. In the figures, a 4 in. by 4 in. grid is shown on the column, allowing approximation of damage locations. From these figures, it can be seen that the grouted splice sleeve connection localized the damage at the base (the top elevation in the actual case) of the column. Spalling of the column concrete reached a maximum height of 11.5 in. while the last major structural crack occurred 13 in. above the column base, or 62 percent the column thickness. Figure 80 shows the fractured longitudinal bar in the column. The fracture of the bar occurred 1 in. from the top of the pier cap.

During the test, the pier cap exhibited minor cracking and remained elastic throughout the test. Therefore, the pier cap did not need any repair and was not repaired.

4.1.2 PCLEN-2 Repair Strategy

The structural integrity of the column cross-section is compromised by extensive spalling and severe structural cracks. The integrity of the column cross-section can be reestablished by relocating the plastic hinge in the column to an area just above the original plastic hinge. From

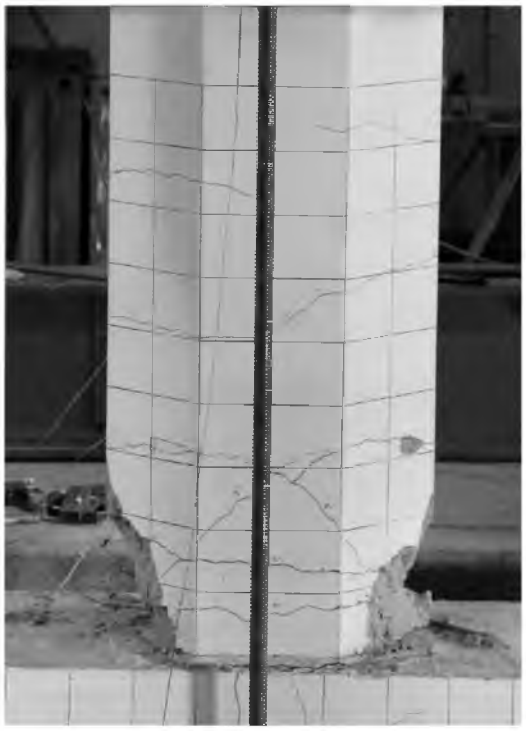

Figure 76. PCLEN-2 Column Damage

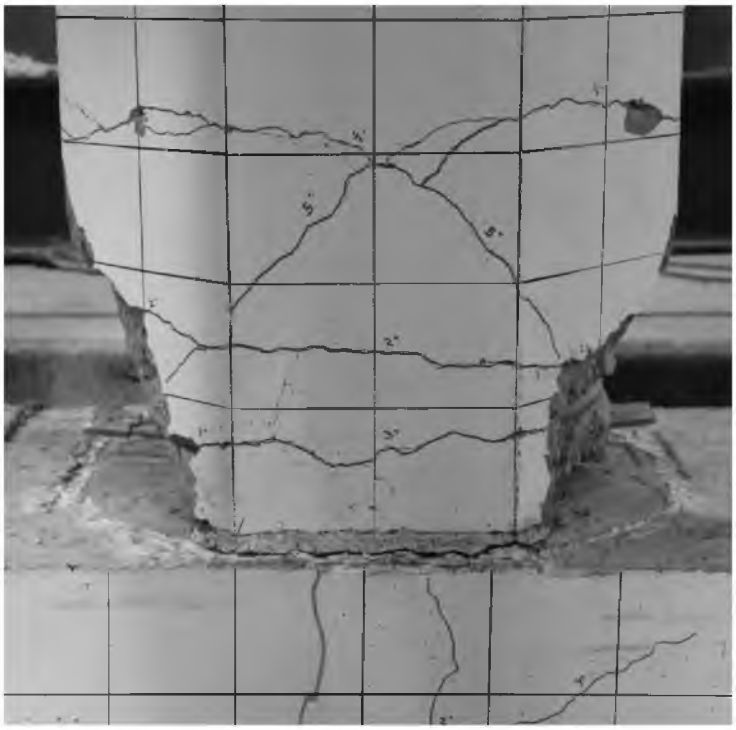

Figure 77. PCLEN-2 Column Damage Close Up

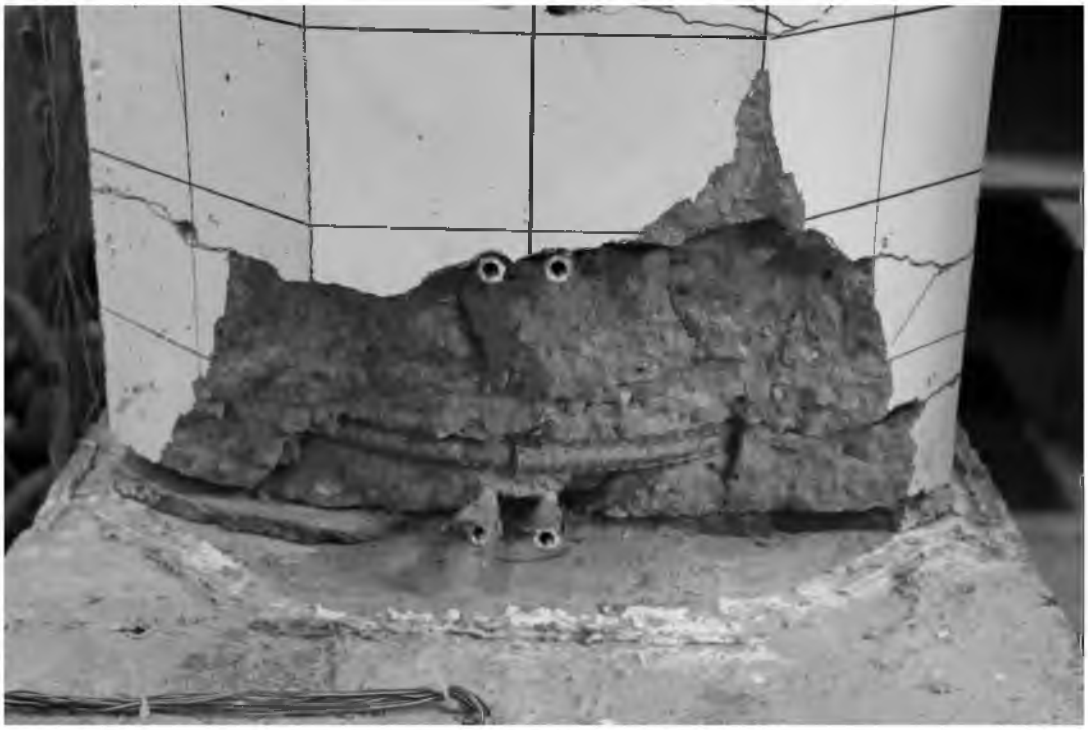

Figure 78. PCLEN-2 West Face Damage

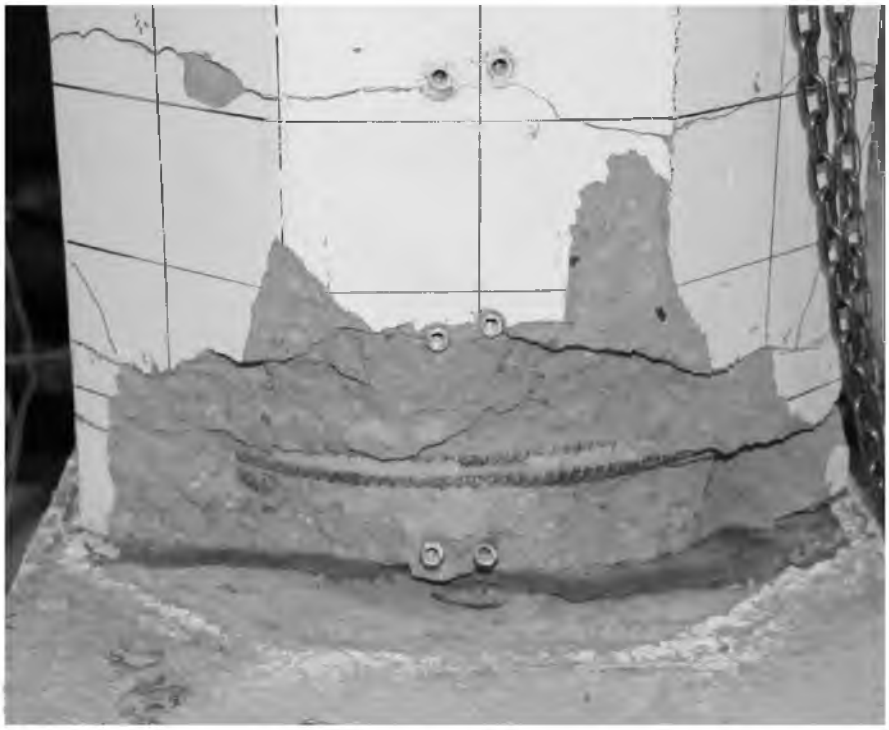

Figure 79. PCLEN-2 East Face Damage

Figure 80. PCLEN-2 Fractured West Longitudinal Bar

the existing damage in the column, an original plastic hinge height of 13 in. can be observed. Therefore, if the plastic hinge were to be relocated a distance equal to or greater than 13 in. from the column base, the integrity of the column cross-section could be reestablished.

Also, because a longitudinal bar fractured in the column of the original specimen, a new mechanism was needed to transfer forces induced by the bending moment from the column to the pier cap. To achieve the transfer of the column bending moment, external bars were postinstalled into the pier cap to complete the load path. Since the plastic hinge is also being relocated away from the damaged area, the original plastic hinge region has to have an increased moment capacity which is another reason for adding external reinforcement.

In order to force the plastic hinge to its new location in the column, the base of the column was repaired using a prefabricated CFRP shell to provide confinement and also to act as concrete formwork. Inside the prefabricated CFRP shell, headed mild steel bars were epoxy anchored into the pier cap to increase the flexural capacity of the plastic hinge region of the damaged column. Subsequently, nonshrink concrete was used to fill the void between the original column and CFRP shell.

4.1.3 PCLEN-2 Repair Design

The first step in the repair design requires the selection of a new plastic hinge location. While many new plastic hinge locations can be chosen, it is important to note that the higher the plastic hinge is relocated, the greater the moment demand becomes to reach the same lateral deformation capacity. Also, not only does the new plastic hinge location need to be above the previous one, but an appropriate height needs to be provided to allow proper development of the postinstalled headed bars in the repaired region. An 18 in. height was chosen due to the available widths of carbon fiber reinforced polymer (CFRP) in the lab, which satisfied the requirements for a new plastic hinge location. For this research, a new plastic hinge location of 18 in. from the column base was chosen.

The second step involves the extrapolation of the moment capacity of PCLEN-2 at the new plastic hinge location to the base of the column, as shown in Figure 81. The required

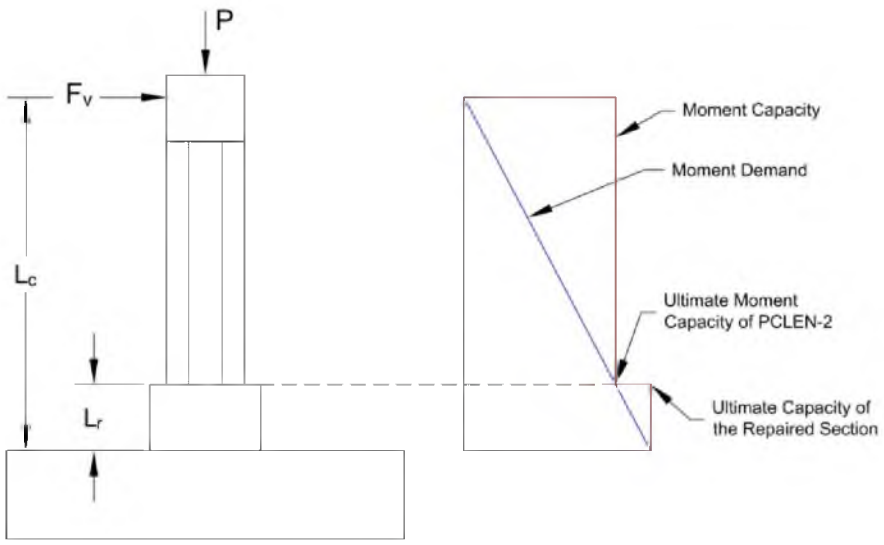

Figure 81. Extrapolation of PCLEN-2 Moment Capacity

moment capacity for the section at the base of the column, M_{Base}, is given by equation 1.

$$M_{Base} = \frac{M_{PCLEN-2}}{L_c - L_r} * L_c \quad (1)$$

where;

$M_{PCLEN-2}$: Ultimate moment capacity of PCLEN-2

L_c : Column height

L_r : Repair height

From the test results of PCLEN-2, the ultimate moment capacity of the cross-section was 278 kip-ft. Therefore, using a column height of 8 ft and a repair height of 18 in. the extrapolated moment at the base of the column is 342 kip-ft and is induced by a lateral load, F_v, of 43 kips.

Next, the column cross-section in the repaired region was converted into a 30 in. diameter circular section using a prefabricated CFRP shell with the addition of postinstalled headed bars laid out as shown in Figure 82. This layout was developed in order to reduce the group effects between the postinstalled headed bars while also keeping the diameter of the CFRP shell to a minimum. There was also a physical limitation that the bars could be no closer

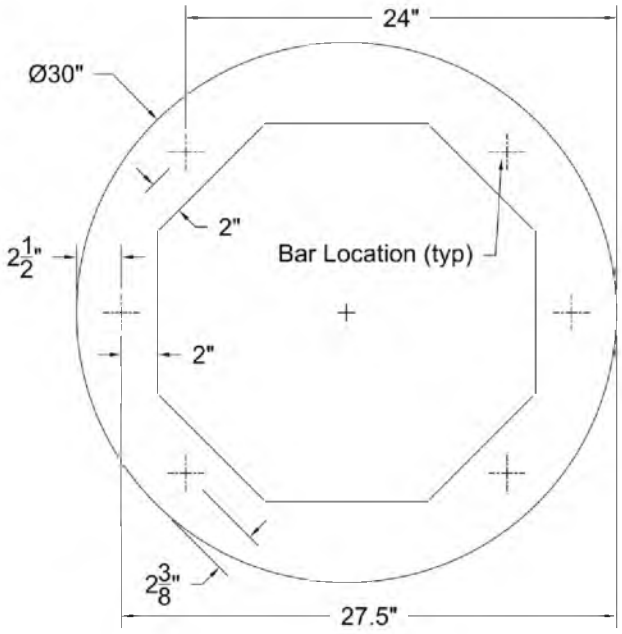

Figure 82. Repair Bar Locations

than 2 in. from the column to allow drilling of the holes for the postinstalled bars. From this layout, the distance from the extreme compression fiber to the centroid of the postinstalled bars, d, is 25.17 in.

The ultimate tension in the postinstalled bars, T_u, caused by M_{base} was computed using equation 2. With the assumption that j is equal to 0.9, T_u was found to be equal to 181 kips.

$$T_u = \frac{M_{Base}}{jd} \quad (2)$$

For the repair to be successful, the ultimate tensile capacity of the postinstalled bars in the repaired region needs to be larger than T_u. To achieve this, three grade 60 #8 bars were used and the ultimate tensile capacity of the bars was assumed to be 130 percent of yield. Equation 3 shows that the tensile capacity of the bars, T_n, is 185 kips which is adequate for the repaired region.

$$T_n = 1.3 * f_y * A_s \quad (3)$$

Note that in determining the size and number of reinforcing bars needed in the repaired region, the existing bars in the column were excluded from the computations. This was done since the integrity of the existing bars and their bond to the sleeve was unknown, and it was felt that it was not appropriate to rely on them for any tensile reinforcement.

The development length of the postinstalled bars needs to be less than the height of the repair in order for them to be effective. Using XTENDER HRC 555 headed rebar from Headed Reinforcement Corp. the development length, L_{dt}, of a headed bar according to ACI 318-11 (21) is given in equation 4.

$$L_{dt} = \left(\frac{0.16 * f_y}{\sqrt{f'_c}}\right) * d_b \quad (4)$$

where:

f_y : yield strength of the bar, 60,000 psi

f'c : concrete compressive strength, 6,000 psi

d_b : bar diameter, 1 in.

Therefore, the development length of a #8 headed bar is 12.4 in. which was less than the height of the repair. For this repair, it was decided that a cover of 3 in. should be used, leaving a final bar length of 15 in. in the repaired region.

The bond length of the epoxy anchored bar also has to be checked to ensure proper tension transfer from the postinstalled bar to the pier cap. The minimum length to develop the ultimate strength of the bar in tension is given by equation 5.

$$L_d = \frac{A_b * 1.3 * f_y}{d_b * \pi * \tau_{bond}} \quad (5)$$

where:

A_b : area of bar, 0.79 in^2

f_y : yield strength of the bar, 60,000 psi

d_b : diameter of bar, 1 in

τ_{bond} : bond strength of epoxy

Using Hilti HIT-RE 500-SD epoxy which has a bond strength of 1800 psi, the minimum embedment length of the #8 headed bar from equation 6 was found to be equal to 11 in. For the repair, it was decided to embed the bars a length of 19 in. to ensure pullout of the postinstalled bars would not occur.

The final design consisted of six postinstalled headed bars that were embedded 19 in. into the pier cap and had a length into the repaired region of 15 in., as shown in Figure 83.

The thickness of the CFRP jacket was designed for shear and confinement with the goal of preventing strain softening from occuring. To determine the required CFRP jacket thickness, t_j, for shear equation 6 was used which was developed for columns with a circular cross-section (1).

$$t_j = \frac{\frac{V_o}{\varphi_v} - (V_c - V_s - V_p)}{\frac{\pi}{2} \cdot 0.004 \cdot E_j \cdot D} \quad (6)$$

where:

V_o : is the column shear demand, 43 kips

φ_v : is the shear capacity reduction factor, typically 0.85

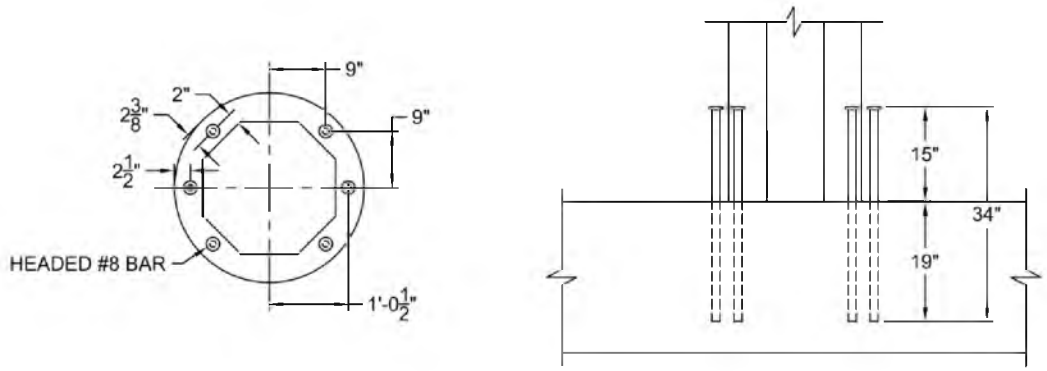

Figure 83. Postinstalled Headed Bar Design

V_c, V_s, and V_p : is the shear capacity contribution from the concrete, shear reinforcement, and axial load. For this design, all three terms were conservatively taken as zero.

E_j : is the modulus of elasticity of the CFRP jacket, assumed to be 12,000 ksi for design

D : is the diameter of the jacket, 30 in.

From equation 7, the required jacket thickness for shear is 0.02 in. which results in one layer of CFRP.

To determine the required CFRP jacket thickness for confinement and to prevent strain softening, equation 7 was used for columns with a circular cross-section (*25*).

$$t_j = \left(\frac{f_{co}}{E_j}\right) \cdot \left[\frac{H_c \cdot \lambda_{SH}}{4 \cdot C_{sh}}\right] \quad (7)$$

where:

f_{co} : is the unconfined concrete compressive strength, 6 ksi

H_c : is the diameter of the CFRP jacket, 30 in.

λ_{SH} : is 12 for circular sections

C_{sh} : is 1

From equation 7, the required jacket thickness to prevent strain softening is 0.045 in. which results in two layers of CFRP. Therefore, a total of four layers of CFRP were needed. One layer was used of the CFRP shell, one layer was provided for shear, and two layers were provided for confinement and to prevent strain softening.

Figure 84 shows the details of the final design of the CFRP wrap which was 18 in. high and 30 in. in diameter with the fibers oriented in the hoop direction. A 1/2 in. gap was left between the bottom of the wrap and the top of the pier cap to prevent the wrap from bearing on the pier cap. Also since the diameter of the wrap was larger than the width of the pier cap, a wood form was built to widen the pier cap to be able to cast the concrete.

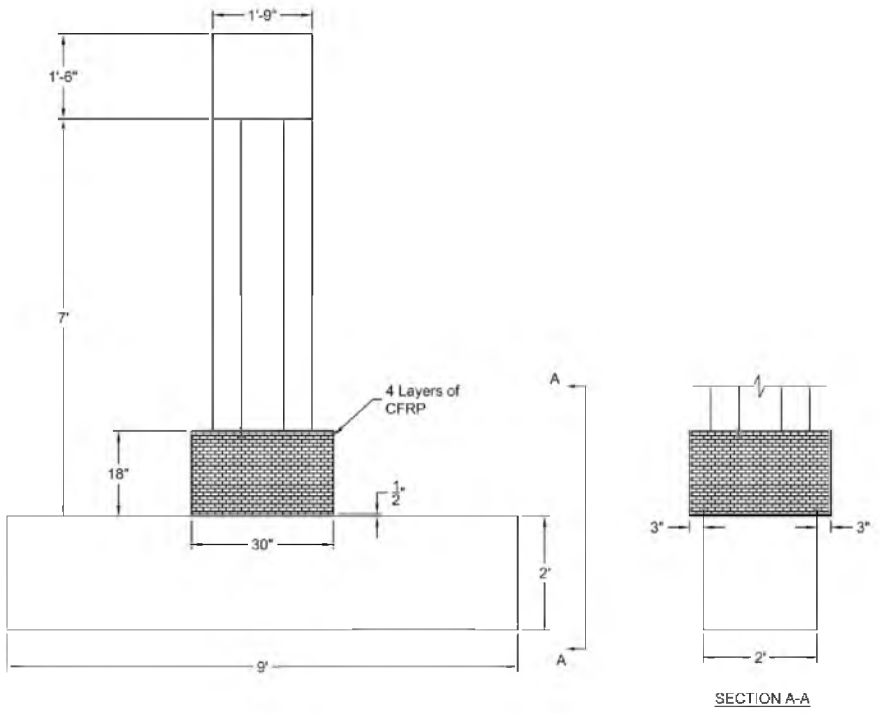

Figure 84. Wrap Design

4.1.4 PCLEN-2 Repair Procedure

The first step in the repair was to create prefabricated CFRP shells. To achieve this, a 100 in. long by 18 in. wide piece of Sikawrap – Hex 103c carbon fiber was impregnated by hand with Sikadur 300 epoxy. With the fibers oriented in the hoop direction, a single layer of CFRP was wrapped around a 30 in. sonotube which provided the proper shape for the shell. Before applying the CFRP, the sonotube was prewrapped with heavy duty plastic sheeting to prevent the epoxy from bonding to the sonotube; this enabled easy removal of the CFRP shell. The 100 in. long carbon fiber sheet provided enough length so the two ends of the carbon fiber sheet would overlap by 6 in., thus providing an adequate splice length for the fiber to exhibit a monolithic performance. Figure 85 shows the CFRP sheet being laid up on the sonotube where it was left for 7 days to cure.

While the CFRP shell was curing, the holes for the postinstalled headed bars were drilled by Penhall Company, Inc. For the postinstalled headed bars, a 1.25 in. diameter hole was drilled using a diamond core drill bit which had the ability to cut through concrete as well as any steel

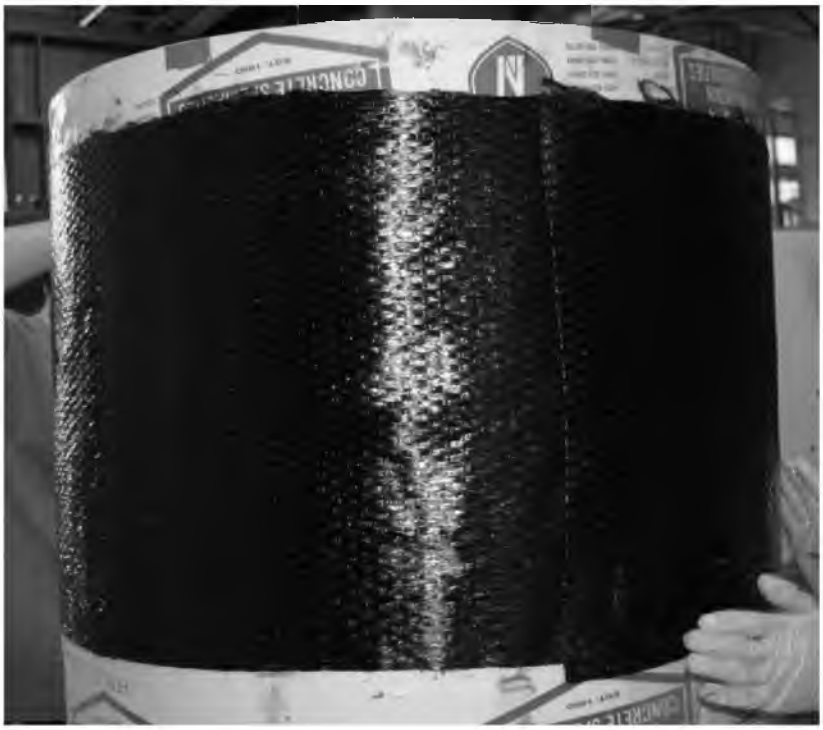

Figure 85. Prefabricated CFRP Shell on Sono Tube Form

reinforcement in the pier cap. Figure 86 shows a Penhall worker drilling out the holes for the postinstalled headed bars.

Once the holes were drilled, they were cleaned and dried using standard methods from the Hilti installation instructions flow chart. Once cleaned and dried, Hilti HIT-RE 500-SD epoxy was injected into the bottom of the borehole using the Hilti HIT-Dispenser. While injecting the epoxy, extra care was taken to avoid the formation of air voids. After adding the epoxy to the borehole, the bar was inserted while being slowly twisted. Once the bar is inserted, there needs to be enough epoxy to completely fill the void between the bar and the side of the hole. If the borehole was not completely filled, the bar was removed, additional epoxy added, and the bar reinserted. Figure 87 shows the headed bars being epoxied into the pier cap. Notice in this figure how excess epoxy is forced from the borehole when the bar is inserted. The excess epoxy indicates that adequate epoxy has been added to the borehole. After inserting the bars into the boreholes, the anchors were not disturbed for at least 18 hours.

When the prefabricated shells had cured, they were split into two halves and spliced

Figure 86. Drilling of Postinstalled Head Bar Holes

Figure 87. Epoxying of Headed Bars

around the column, as shown in Figure 88. This procedure was performed since in a real bridge, it would be impossible to get the shell around the column without first cutting it in two. Figure 88 shows that the sonotube is still behind the split CFRP shell. This was done in order to maintain the circular shape because a single layer of CFRP at this diameter was found to be too flexible and would not be able to keep its shape as the additional layers of CFRP were added. Also, in Figure 88, there is wood formwork on the edge of the pier cap. This wood formwork is in place to extend the width of the pier cap since the diameter of the repair is larger than the width of the pier cap.

With the split CFRP shell around the column a 12 in. long by 18 in. wide piece of CFRP was used to splice the two halves of the CFRP shell with the fibers of the splice oriented in the hoop direction. Once the first layer of the CFRP shell was spliced, the additional 3 layers of CFRP were added, as shown in Figure 89, with the fibers oriented in the hoop direction and left to cure for 7 days. This was the last step in completing the construction of the CFRP jacket and stay-in-place formwork for the repair. It should be noted that there are methods that decrease the

Figure 88. Split CFRP Shell

Figure 89. Applying Additional Layers to CFRP Shell

curing time of the CFRP. While these methods were not used in this research to construct the CFRP jacket and stay-in-place formwork, they could be used to speed up the repair procedure from two weeks to just a few days.

Once the CFRP jacket had fully cured and was centered on the column, nonshrink concrete with a mix design as specified in Table 10 was added to the gap between the column and CFRP jacket, as shown in Figure 90. The nonshrink concrete was then left to cure for 28 days before testing.

4.1.5 PCLEN-2 Repair Results

The repair of PCLEN-2 is denoted by PCLEN-2R where the “R” stands for repair. The test setup for PCLEN-2R is very similar to PCLEN-2 except that for PCLEN-2R, an axial load of 105 kips was applied.

Table 10. Mix Design of Nonshrink Concrete per 1/2 yd^3

Component		Weight (lb)
Cement	Portland Cement	305
	Komponent	46
Water	Weight	140
Rock	3/4" minus gravel	818.5
Sand	Weight	579.5
Additives	glenium 30-30	1.53
	daravair	0.2

Figure 90. CFRP Jacket (a) Without Nonshrink Concrete; (b) With Nonshrink Concrete

4.1.5.1 PCLEN-2R Instrumentation

During the test, strain gages, linear variable differential transformers (LVDTs), and string pots were placed on PCLEN-2R to monitor its performance. The location of the LVDTs is shown in Figure 91. In this figure, each LVDT is with the displacement capacity of the LVDT shown in parentheses under the LVDT designation. LVDT-1 and LVDT-2 were used to measure the curvature of the repaired section while LVDT-3 and LVDT-4 measured the curvature of the

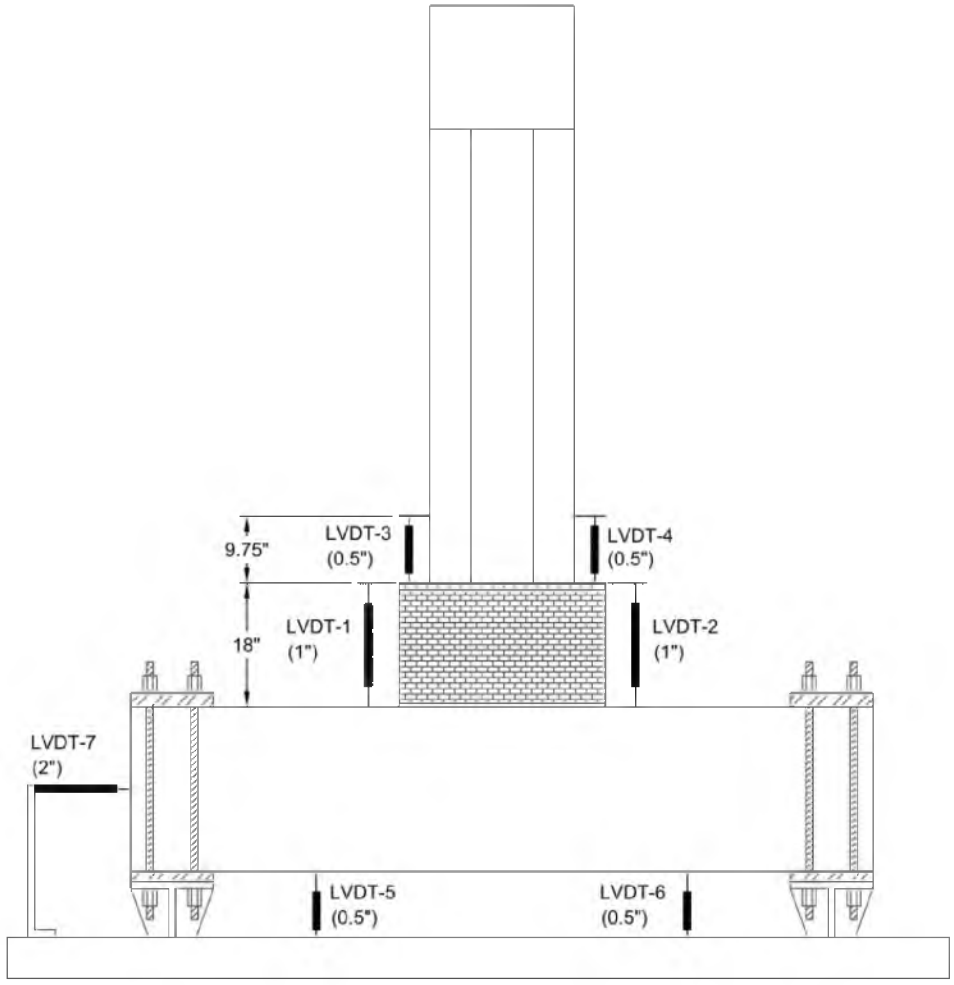

Figure 91. PCLEN-2R LVDT Layout

column just above the repair. LVDT-5 and LVDT-6 were used to measure the deflection of the pier cap, while LVDT-7 was used to measure any slip during the test.

To monitor the strains in the CFRP jacket, strain gages were placed as shown in Figure 92. Each strain gage designation has three symbols. The first letter represents a strain gage. The middle letter designates what component the gage is on, where W is used for the CFRP jacket. The final letter and number represent the location of the gage. For example, SG-W-2E is a strain gage located on the CFRP jacket and it is located on the east side of the repair in section 2. There was also a single strain gage added to the extreme headed bar on each side of the column. These gages are denoted as SG-HB-W for the gage located on the extreme west

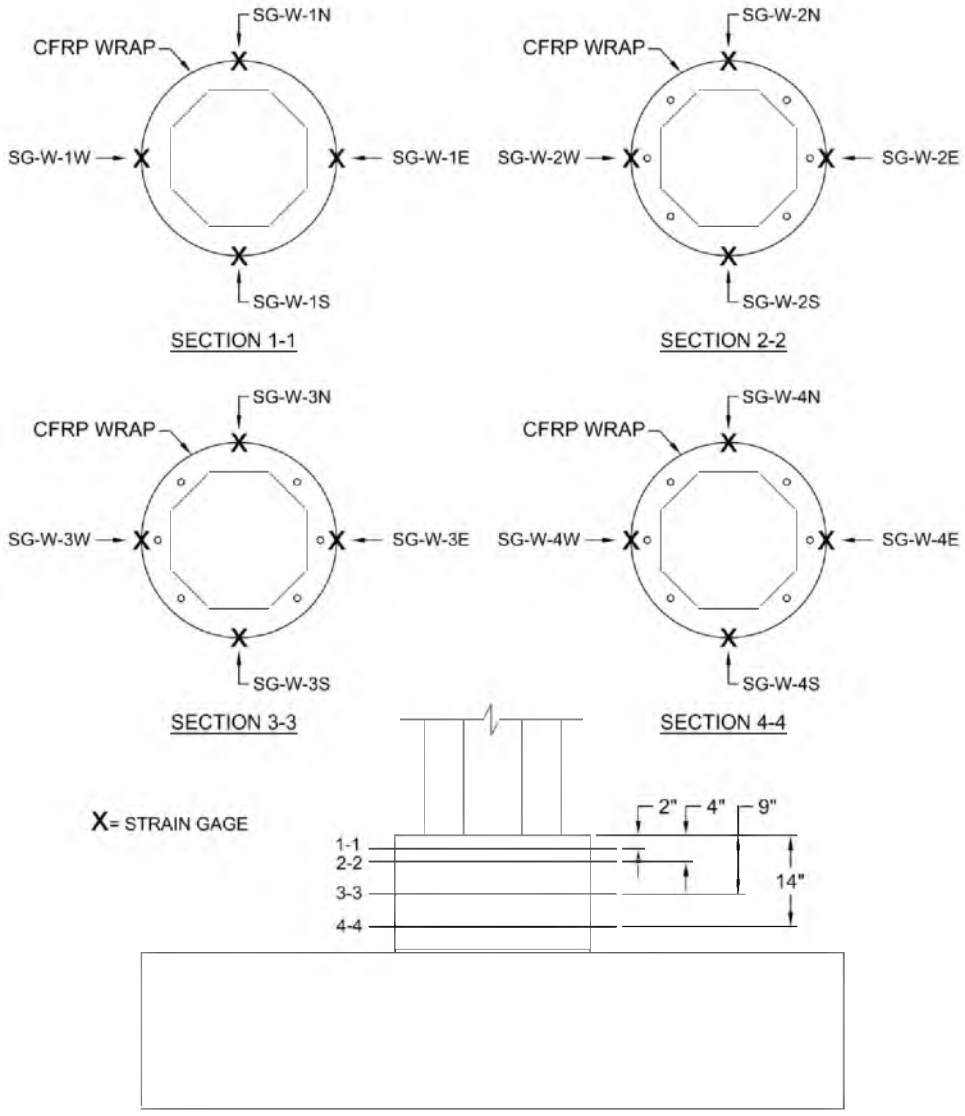

Figure 92. PCLEN-2R CFRP Strain Gages

headed bar, and SG-HB-E for gage located on the extreme east headed bar. Both gages were located 7.5” above the pier cap which is half way between the pier cap and the top of the headed bar.

To monitor the horizontal displacement of the top of the column, two string pots were used and were connected to the column at the neutral axis. The displacements measured from these string pots were then averaged to obtain the actual displacement of the column.

4.1.5.2 PCLEN-2R Material Properties

The material properties for PCLEN-2R are given in Table 11. The steel tensile properties were obtained using ASTM A370-09a (*17*), the concrete properties were obtained from 4 in. diameter by 8 in. high concrete cylinders following ASTM C39 (*24*), the grout properties were obtained using ASTM C109, and the CFRP properties were obtained using ASTM D3039 (*18*).

4.1.5.3 PCLEN-2R Monotonic Pushover Test Results

It was intended to load PCLEN-2R with the loading protocol shown in Figure 56. It was not known, however, that the polarity of the actuator applying the lateral displacements was reversed. Hence, when the test began, the actuator pushed the column to the east to a displacement of 6.65 in. before it could be stopped. The column at the maximum displacement is shown in Figure 93. In this figure, it can be seen that the plastic hinge has been successfully moved above the repair with extensive spalling on the east side of the column that extends up to 20 in. There are, in addition, major flexural cracks that opened on the west side of the column at 2 in., 9 in., and 12 in. above the repair.

After the monotonic pushover, PCLEN-2R was pulled back to zero displacement and the damage was assessed. Figure 94 shows the damage to the column with the loose concrete removed and the column at zero displacement. In the figure, cracks that were observed from the original test are marked in red while the cracks that occurred from the push over are marked in black. With the cracks closed, it can be seen that the cracks that were observed during the monotonic pushover at 2 and 12 in. were existing cracks that opened up, while the crack that was observed at 9 in. is new.

From the test observations of PCLEN-2, the existing cracks at 2 and 12 in. were originally hairline cracks, but after the monotonic pushover, they had grown substantially to a width of 0.05 in. The new crack that opened at 9 in. had a width of 0.016 in.

With all of the loose concrete removed from the east side of the column, it can be seen that the concrete cover has crushed thus exposing the spiral reinforcement. Also, there were four radial cracks in the new concrete added for the repair. These cracks extended from four of the

Table 11. PCLEN-2R Properties

Bar Properties						Column & Beam Concrete Strength		Grout Strength		Repair Concrete Strength		CFRP Jacket	
Longitudinal (No. 8)		Transverse (No. 4)		Headed (No. 8)									
F_y (ksi)	F_u (ksi)	F_y (ksi)	F_u (ksi)	F_y (ksi)	F_u (ksi)	28-day (ksi)	Test-day (ksi)	28-day (ksi)	Test-day (ksi)	28-day (ksi)	Test-day (ksi)	F_u (ksi)	E_j (ksi)
68	93	63	103	62	86	3.9	6.0	10.3	13.0	7.0	7.0	100	9000

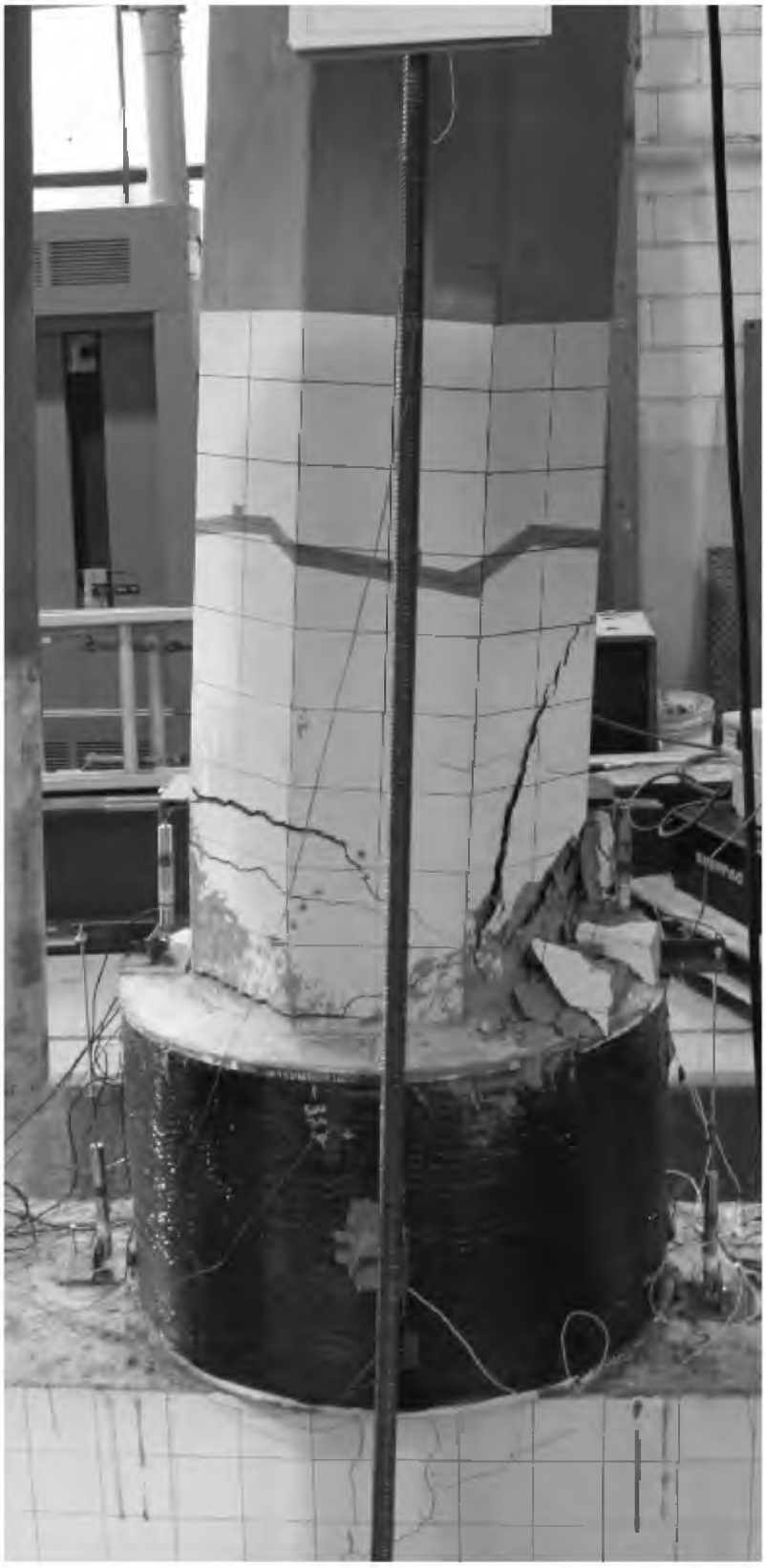

Figure 93. PCLEN-2R Monotonic Pushover at Maximum Drift

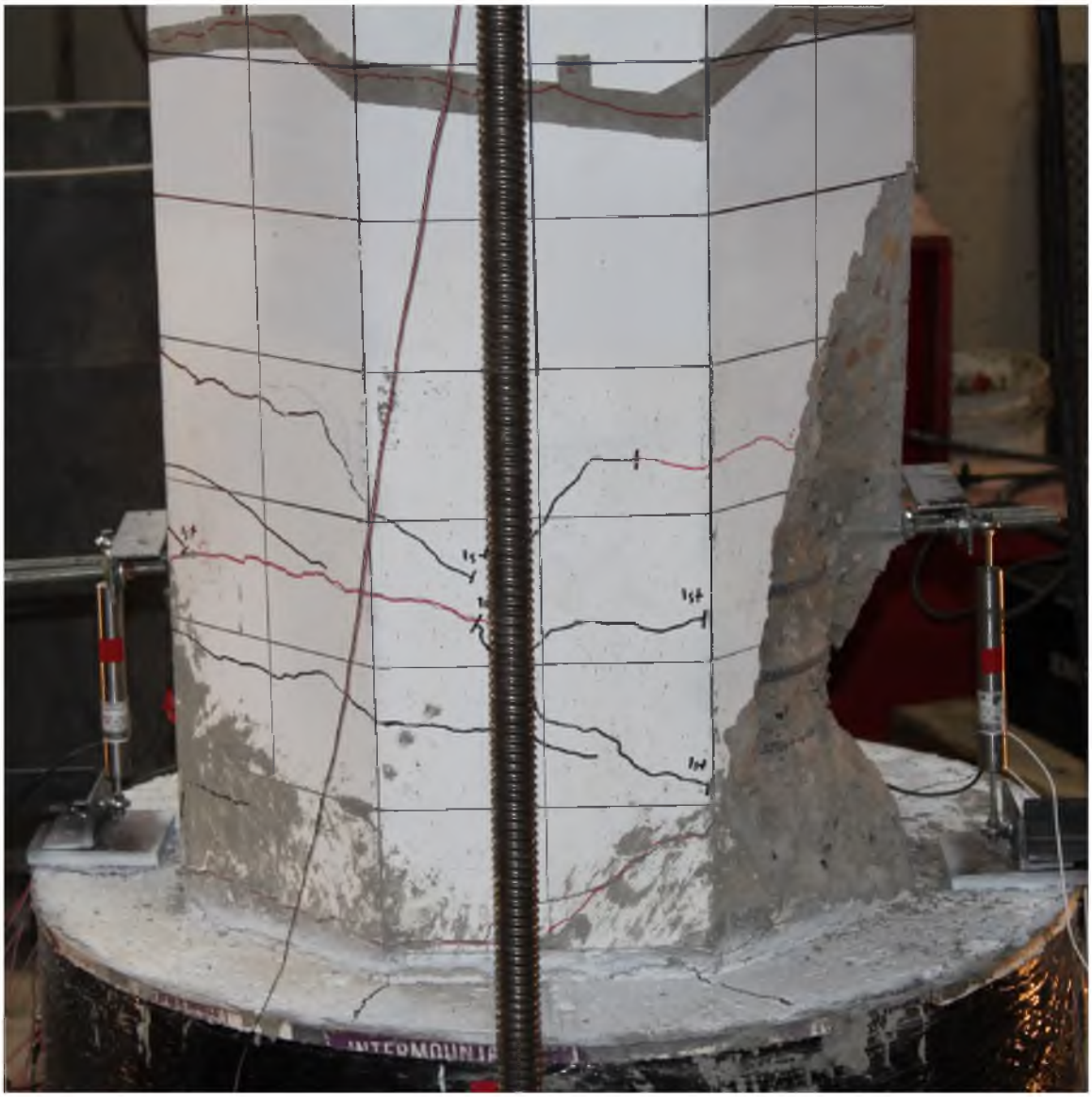

Figure 94. PCLEN-2R Monotonic Pushover Damage

corners of the column out to the CFRP jacket and had a width of 0.01 in.

Although this test did not follow the prescribed loading protocol, the data acquisition system was running during the unintended loading and the monotonic pushover curve shown in Figure 95 was obtained. Point A in the figure corresponds to the maximum lateral load from the monotonic pushover which occurred at a drift level of 2.97 percent. After the maximum lateral load was reached, the concrete on the east side of the column began to crush and the lateral load began to decrease until the actuator was stopped at point B.

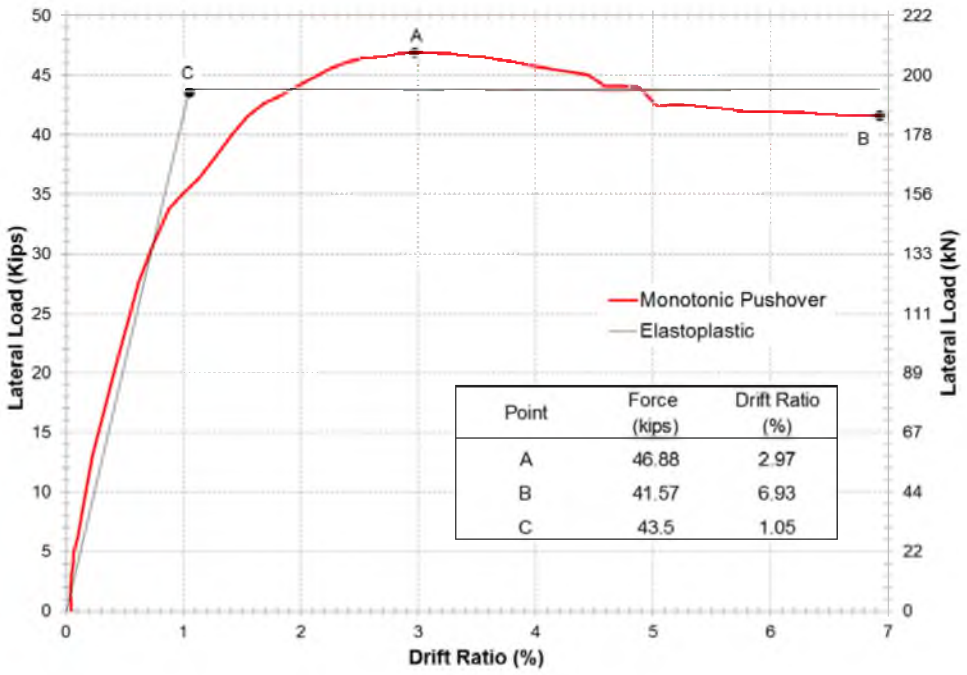

Figure 95. PCLEN-2R Monotonic Pushover Curve

To determine the ductility of PCLEN-2R from the monotonic pushover curve, an idealized elastoplastic curve is superimposed on the monotonic pushover curve. In Figure 95, point C represents the theoretical yield point of the system. To obtain the elastoplastic curve, the equal area method was used. The initial stiffness of the elastoplastic curve was determined by drawing a line through the point at which the lateral load from the push over curve equals 70 percent of the theoretical yield and the origin. Using the elastoplastic curve the ductility was computed by dividing the drift at point B by the drift at point C; a ductility of 6.6 was obtained for PCLEN-2R from the monotonic pushover.

Since the results for PCLEN-2R are from a monotonic pushover instead of a cyclic test, they cannot be reasonably compared to the results of PCLEN-2.

4.1.5.4 PCLEN-2R Monotonic Pushover LVDT and Strain Gage Analysis

In order to better understand the behavior of PCLEN-2R during the monotonic pushover, analysis of the LVDTs and strain gages was performed. The difference in stiffness between the

repaired region and the region of the column just above the repair can be observed from the moment curvature. To compute the curvature of the repaired region, LVDT-1 and LVDT-2 were used and to compute the curvature of the column region LVDT-3 and LVDT-4 were used. The curvature computed using this method gives the average curvature for the cell height being measured. Therefore, LVDT-1 and LVDT-2 measure the average curvature from the top of the pier cap to the top of the repair; LVDT-3 and LVDT-4 measure the average curvature from the top of the repair to 9.75" above the repair.

Figure 96 shows the moment curvature of these two sections where the moment arm was computed at the mid height of the cell. It is important to note that LVDT-3 and LVDT-4 had a 0.5" stroke length which was reached just after the maximum load at a 3.3 percent drift. Therefore, the moment curvature of the column cross-section is incomplete. In Figure 96, it is clear that the stiffness of the repaired region is much greater than that of the original column. Also, once the maximum moment was reached, the repaired section experienced no additional curvature since larger deformations took place in the column just above the repair.

LVDT-5, LVDT-6, and LVDT-7 recorded displacements no larger than 0.01 in. Therefore, the pier cap deflections and slippage of the test specimen was negligible.

The strains that were observed in the CFRP jacket during the monotonic pushover are presented in Figures 97-101. Figure 97 shows the strain on the east side of jacket which is the direction the column was pushed. This side of the jacket experienced the highest strain; the amount of strain decreases towards the pier cap. In all of the figures showing the jacket strain, there is a noticeable plateau; this occurs at about the 3 percent drift level which is where the maximum horizontal load occurred. The fact that the strains in the jacket remain constant after the maximum lateral load is reached suggests that the strains in the jacket are more dependent on the applied horizontal load rather than the displacement of the column.

The strain observed in the extreme headed bars during the monotonic pushover is presented in Figure 101. Since the column was pushed to the east, Figure 101 shows that the postinstalled headed bars on the west side of the column pick up the tension and transfer it to the pier cap while the east headed bars go into compression. From these strain gage data, it is

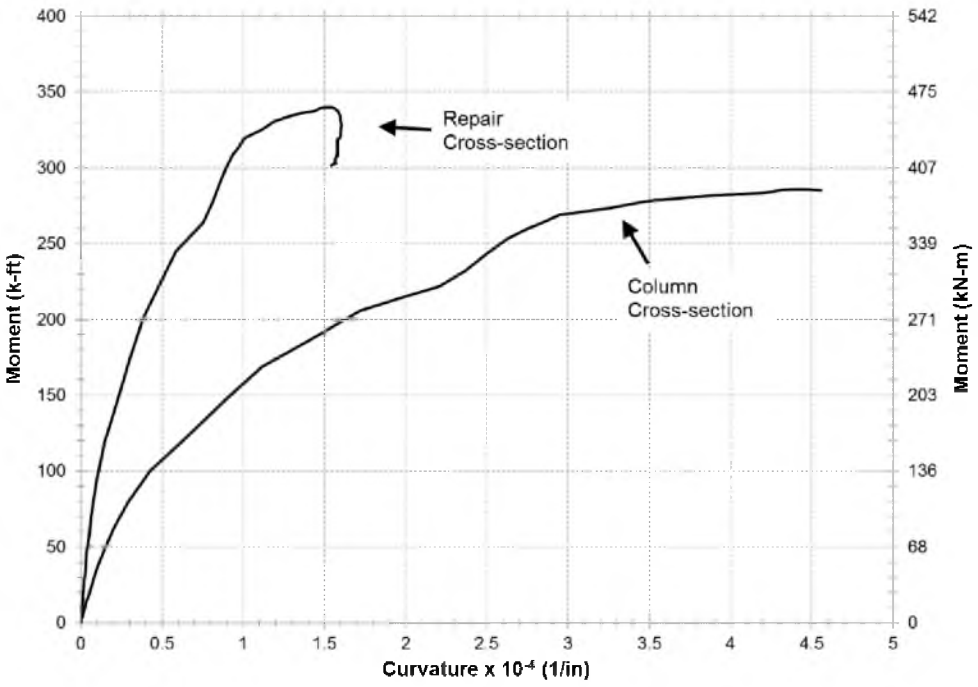

Figure 96. PCLEN-2R Monotonic Pushover Moment Curvature

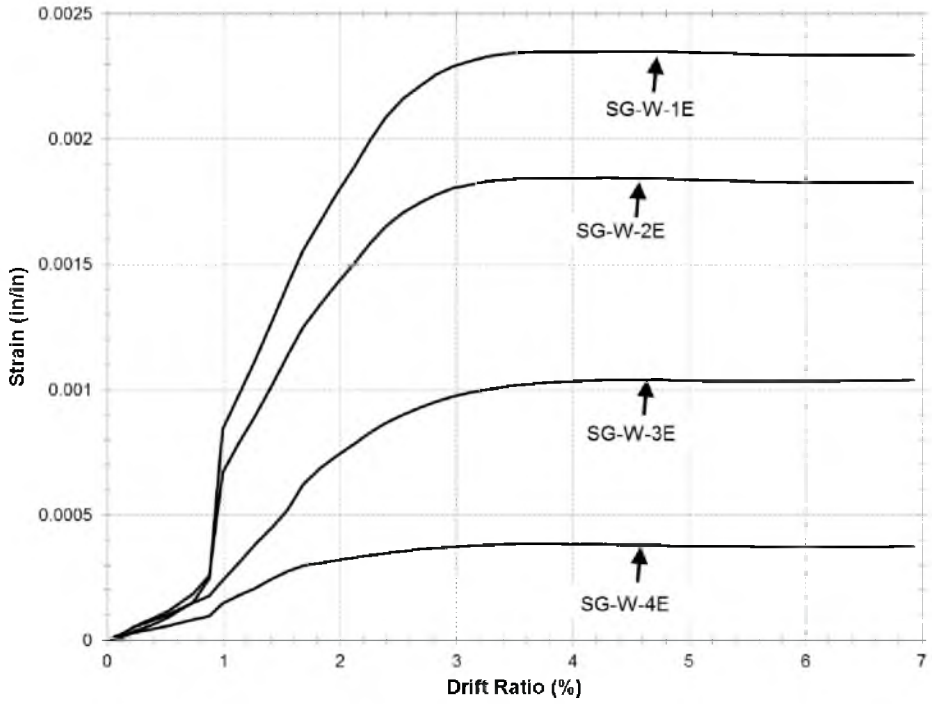

Figure 97. PCLEN-2R East CFRP Jacket Strains

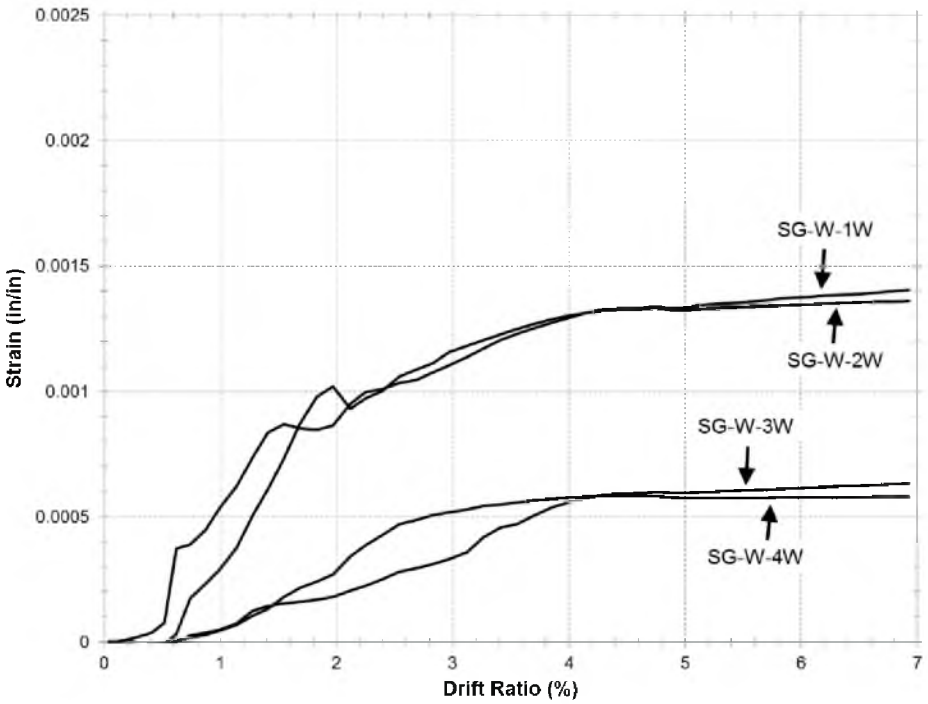

Figure 98. PCLEN-2R West CFRP Jacket Strains

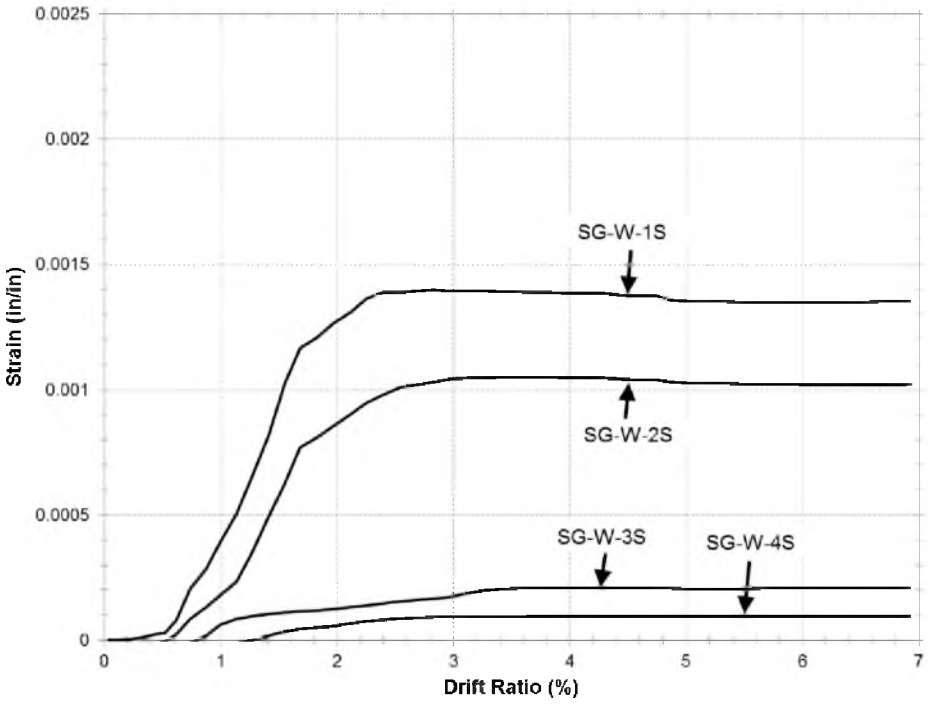

Figure 99. PCLEN-2R South CFRP Jacket Strains

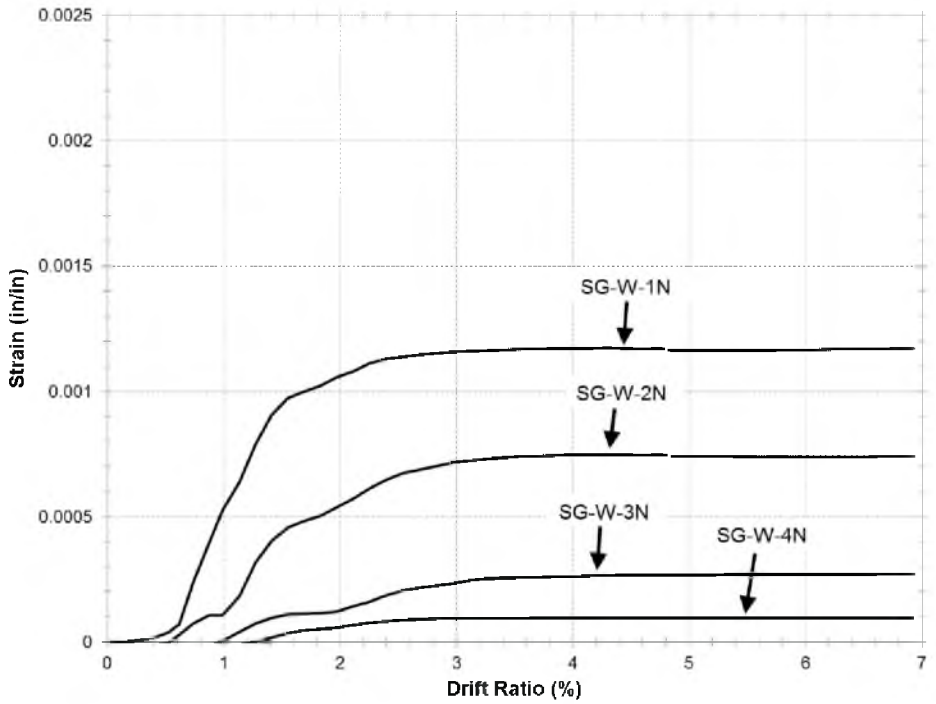

Figure 100. PCLEN-2R North CFRP Jacket Strains

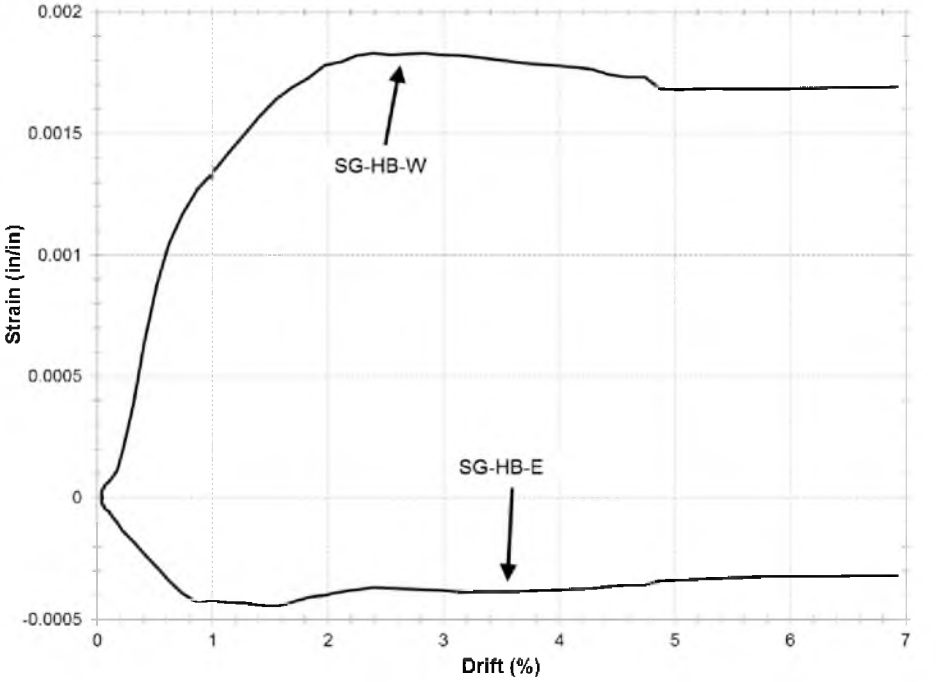

Figure 101. PCLEN-2R Headed Bar Strains

clear that none of the instrumented postinstalled bars have exceeded the yield strain of 0.00207 in./in. It should be noted, however, that this strain gage was located halfway between the pier cap and the top of the headed bar so it may be possible that strains farther away from the head have gone above the yield strain.

The headed bars also have a plateau or drop in strain near the drift level at which the maximum lateral load occurred. Therefore, similar to the strain in the CFRP jacket, the strain in the headed bars depends more on the horizontal load rather than the displacement of the column.

4.1.5.5 PCELN-2R Cyclic Test Results

Although PCLEN-2R was already damaged from the monotonic pushover test, it was decided to retest the column using the loading protocol shown in Figure 56. Even with the initial damage from the monotonic pushover, the column was able to reach a maximum drift of 7.2 percent and a maximum lateral load of 40.5 kips before fracturing the extreme east longitudinal column bar just above the repaired section.

To clearly see the relocation of the plastic hinge in PCLEN-2R, Figure 102 compares PCLEN-2 and PCLEN-2R at maximum drift. In Figure 102 (a), the plastic hinge formed just above the pier cap while in Figure 102 (b), the plastic hinge was relocated to a position just above the repair. In Figures 103 and 104, the final damage of the east and west side of the column is shown respectively. On the east column face, additional spalling of the concrete occurred, exposing more of the column reinforcement; ultimately the extreme longitudinal bar on this side fractured. The west face of the column had spalling that went 10 in. up the face of the column, exposing transverse reinforcement. No additional flexural cracks developed during the test. The cracks that developed from the monotonic pushover test just continued to widen from 0.05 in. to 0.125 in. by the end of the cyclic test.

Figure 105 shows the hysteresis for PCLEN-2R. When the column was pulled back to zero displacement, it required a lateral force of -22 kips to maintain this position due to permanent deformations of the steel reinforcement. Therefore, instead of the hysteresis beginning at zero

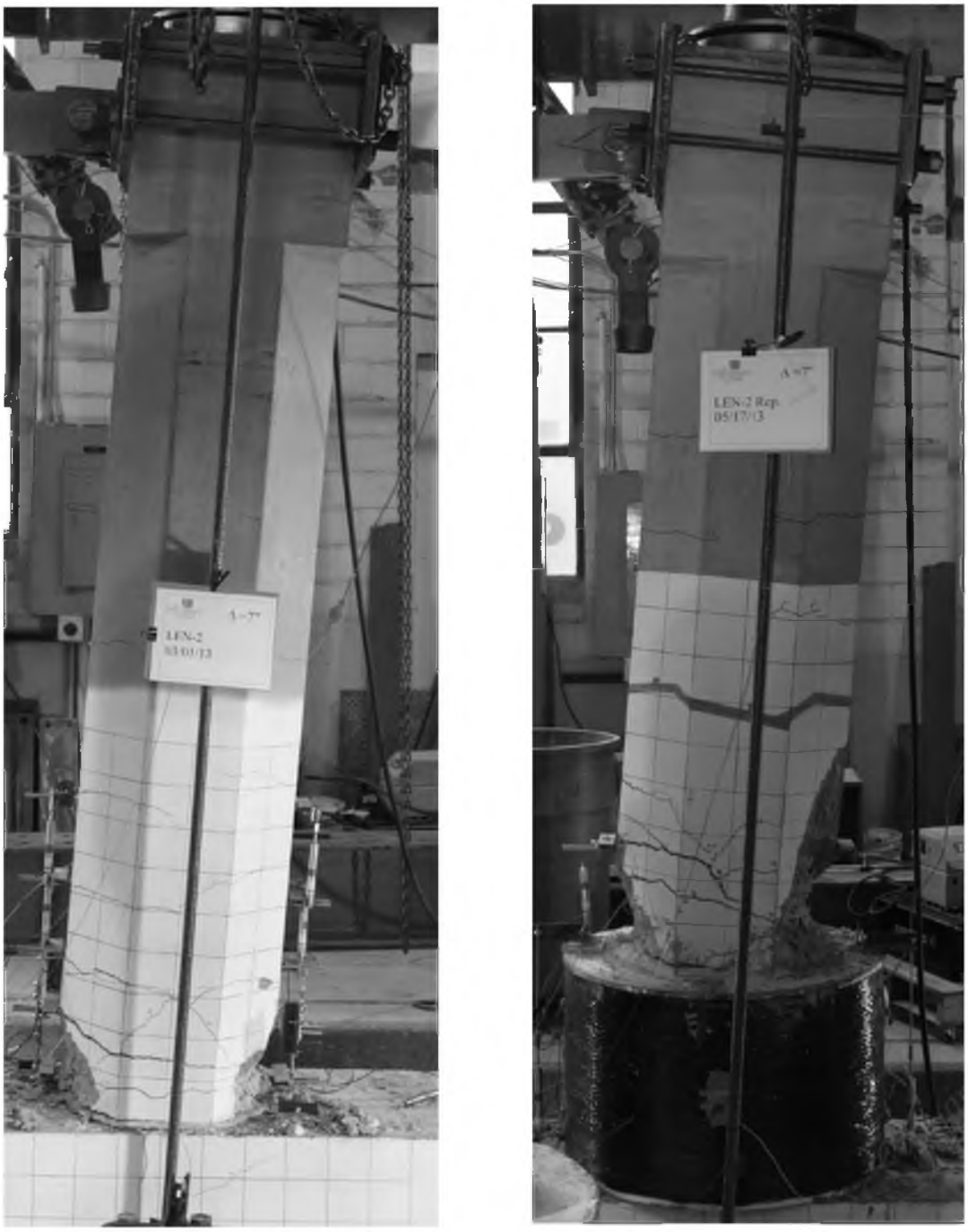

(a) (b)

Figure 102. Test Comparison (a) PCLEN-2 at Maximum Drift (b) PCLEN-2R at Maximum Drift

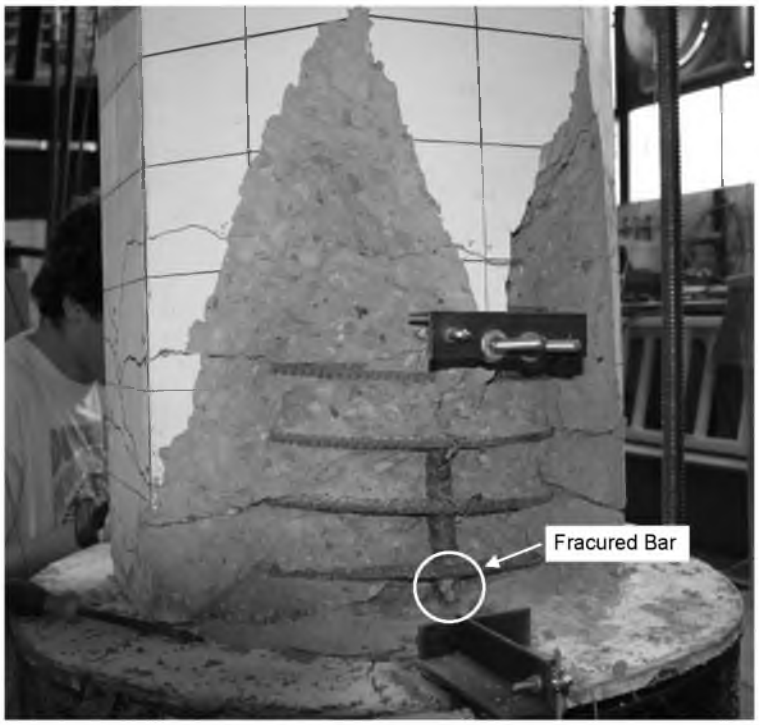

Figure 103. PCLEN-2R East Face Final Damage

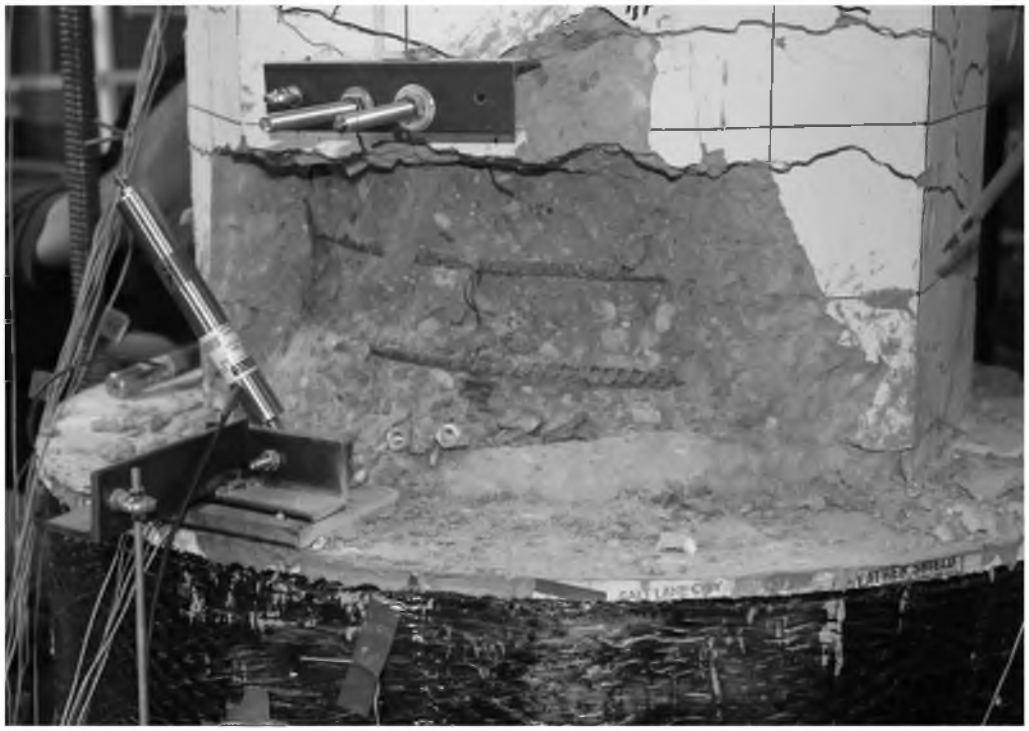

Figure 104. PCLEN-2R West Face Final Damage

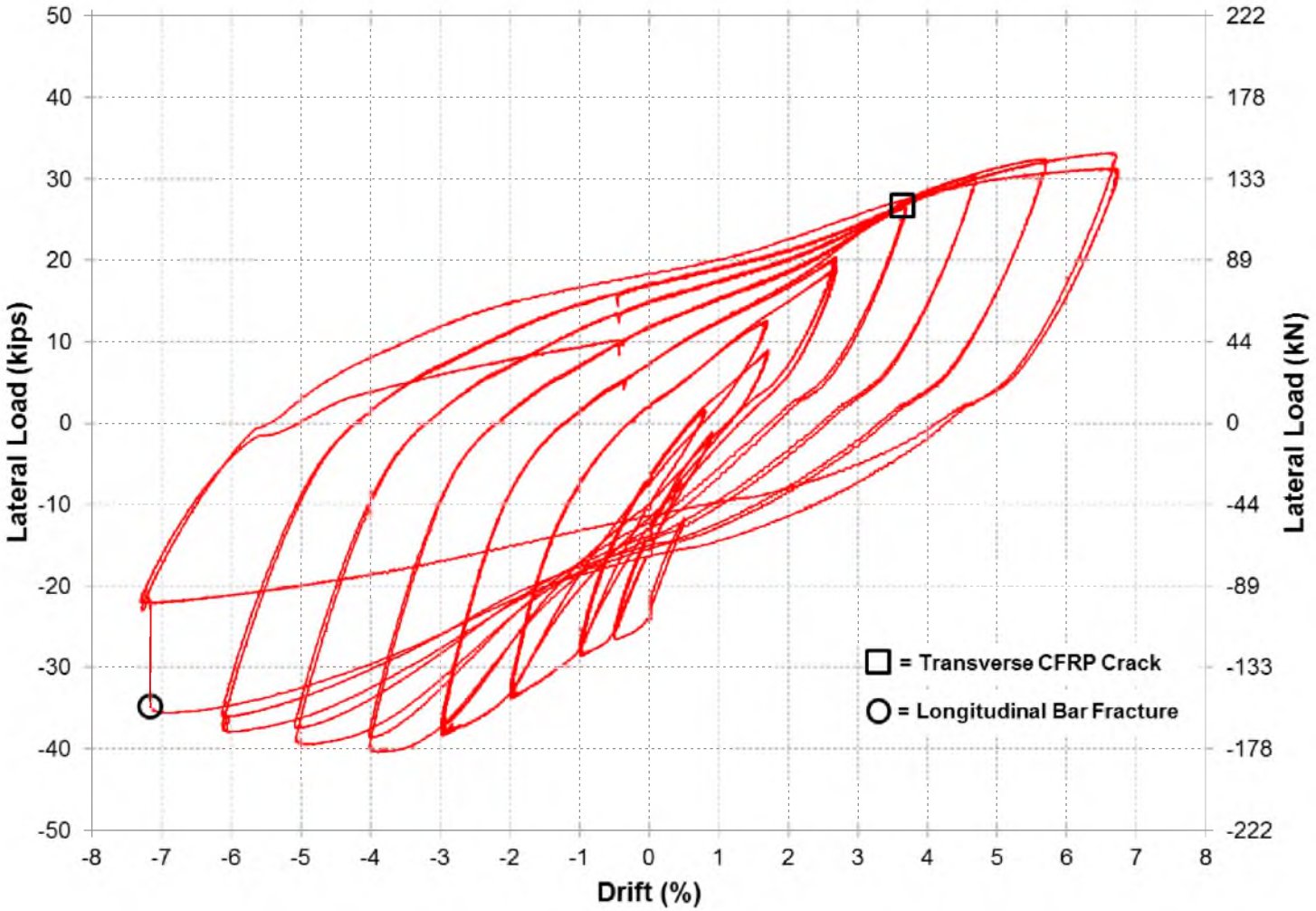

Figure 105. PCLEN-2R Hysteresis

force and zero displacement, it begins at a force of -22 kips and zero displacement. Since there was extensive damage to the column from the monotonic pushover test, the right side of the hysteresis has an unusual shape. The left side of the hysteresis, however, was only slightly affected from the monotonic pushover test and has a more normal shape since the column had not yet been displaced in that direction.

Two notable observations during the test are marked on the hysteresis in Figure 105. The square marks the cycle where transverse cracking of the CFRP jacket began to occur and the circle denotes fracture of the column longitudinal reinforcement. Note that there is no apparent change in the hysteresis, due to the transverse CFRP crack. The cracking of the CFRP jacket occurred just above the top of the headed bars and is shown market by a white line in Figure 106. This crack was not observed during the cyclic test, but was instead identified by the AE event history which will be discussed latter. The crack in the CFRP had a final width of 0.125 in., a length of 38.75 in., and only existed on the west side of the jacket. The crack was caused by an increased curvature demand on the repaired section when the column was pushed to the west.

Figure 106. PCLEN-2R Transverse CFRP Crack

Analysis of the moment curvature is discussed in section 4.1.5.6

Figure 107 compares both the monotonic pushover and cyclic results of PCLEN-2R to PCLEN-2. Since the right side of the hysteresis of PCLEN-2R represents a column that was severely damaged from the monotonic pushover test, it was ignored for the comparison. From Figure 107, it can be seen that the lateral load for both the monotonic pushover and cyclic tests of PCLEN-2R is larger than the lateral load for PCLEN-2. This increase in the lateral load was expected since moving the plastic hinge up the column shortens the moment arm to that section. It is also clear that the displacement capacity of PCLEN-2R is the same as that of PCLEN-2 for both the monotonic pushover and cyclic tests. Since there was no test of PCLEN-2R that can be directly related to PCLEN-2, it is difficult to make an absolute comparison between PCLEN-2R and PCLEN-2 in terms of displacement capacity, ductility, and energy dissipation. However, from the results observed, it would be appropriate to conclude that PCLEN-2R would have performed at least as good as PCLEN-2.

Also in Figure 107, a mirrored plot of the monotonic pushover is superimposed in the 3rd quadrant of the graph in order to compare the monotonic pushover performance to the cyclic performance of PCLEN-2R. From this comparison, it can be seen that up to a drift level of -3 percent the hysteretic response of PCLEN-2R was slightly affected by the initial damage from the monotonic pushover. After a drift level of -3 percent, however, the hysteretic response of PCLEN-2R does not appear to be affected by the initial damage from the monotonic pushover and follows a similar shape to the monotonic pushover curve.

4.1.5.6 PCLEN-2R Cyclic Moment Curvature Analysis

Figure 108 shows the cyclic moment curvature response envelopes of the repaired cross-section. The moment curvature envelopes were obtained by taking the moment and curvature at the maximum and minimum drifts for each set of cycles.

In Figure 108, the curvature of the repaired cross-section is much larger when a positive bending moment is induced (i.e., the column is pushed to the east) than when a negative bending moment is induced. Note that due to the damage caused by the monotonic pushover test, there is

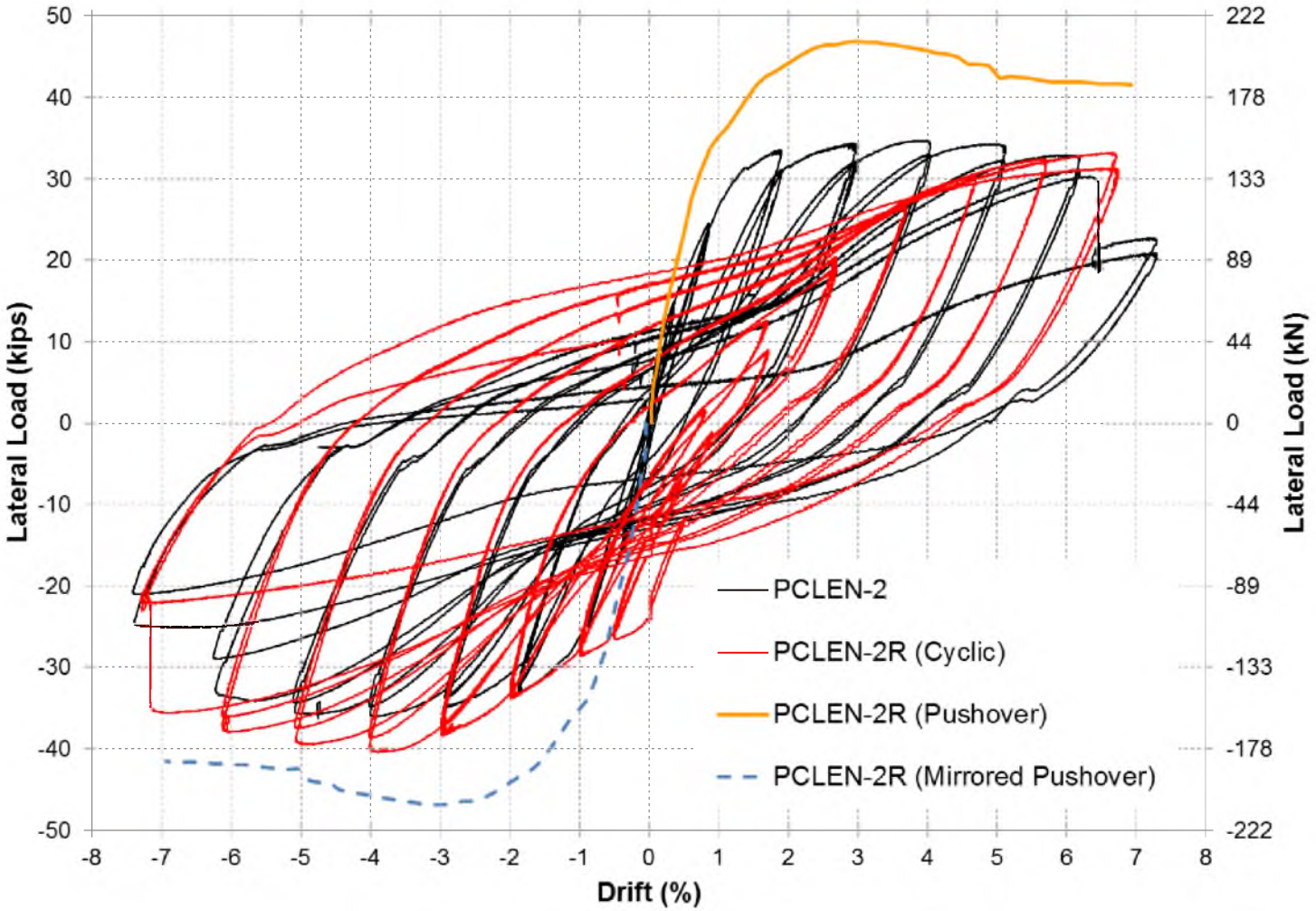

Figure 107. Comparison of Test Results

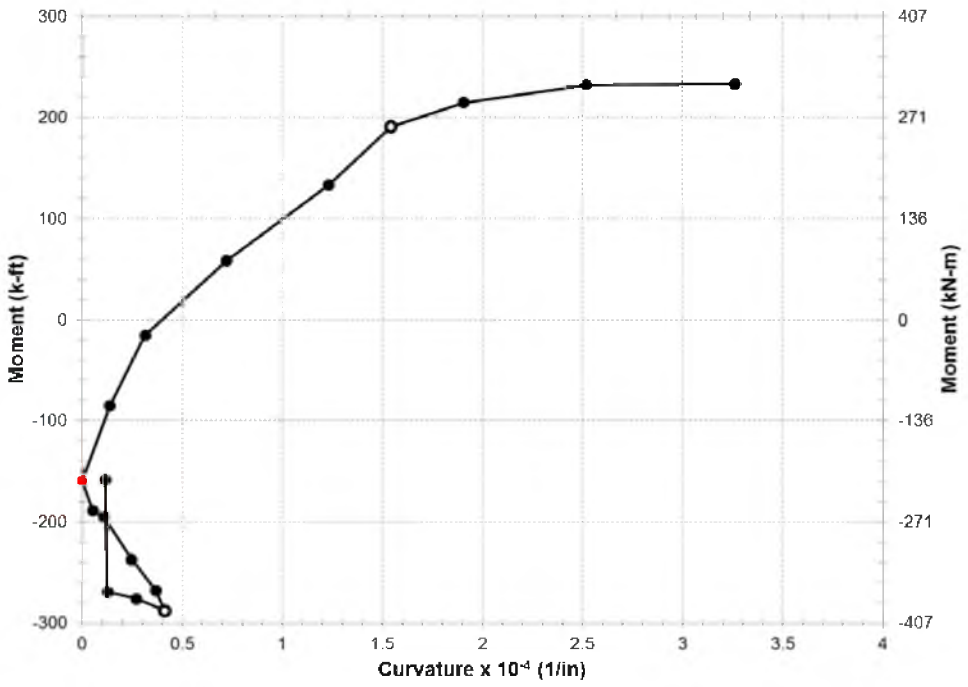

Figure 108. PCLEN-2R Repaired Section Cyclic Moment Curvature Envelope

an initial negative moment on the column at the beginning of the test. The starting point of the moment curvature is denoted by the red circle. The unbalanced curvature demand is even apparent well before the transverse crack in the CFRP begins to occur, which is denoted by the open circles. Referring back to the results of PCLEN-2, an extreme longitudinal bar fractured on the west side of the column, which is the same side as the transverse CFRP crack. Therefore, the column had less moment capacity in the push direction, creating additional tensile demand in the repaired cross-section. The transverse CFRP crack occurred at the section where the postinstalled headed bars were terminated; this means that the tensile capacity of the repaired cross-section in this region consists of the tensile capacity of the concrete and CFRP jacket in the direction perpendicular to the fibers. Unfortunately the combined tensile capacity of these two elements is low in the direction perpendicular to the jacket; thus, a transverse crack is created when these capacities are exceeded in the region above the postinstalled headed bars.

4.1.5.7 PCLEN-2R AE Monitoring Assessment

PCLEN-2R was monitored by six ceramic AE sensors laid out as shown in Figure 109. The AE monitoring system was used to monitor both the monotonic pushover and cyclic tests of PCLEN-2R.

During the monotonic pushover of PCLEN-2R, the sensors located on the column were unfortunately compromised. Due to large amounts of spalling on the east side of the column, AE-6 fell off the specimen with concrete spalling; AE-5 had a large flexural crack open right under the sensor, causing it to loose contact with the concrete surface. Due to these two events, the AE history from the two sensors located on the column could not be used. Also, because of the speed of the monotonic pushover and the small amount of damage that occurred in the repaired region, there were minimal AE events recorded by the sensors located on the CFRP jacket, which resulted in no correlations to damage.

As mentioned earlier, the AE history of the cyclic test picked up when transverse cracking

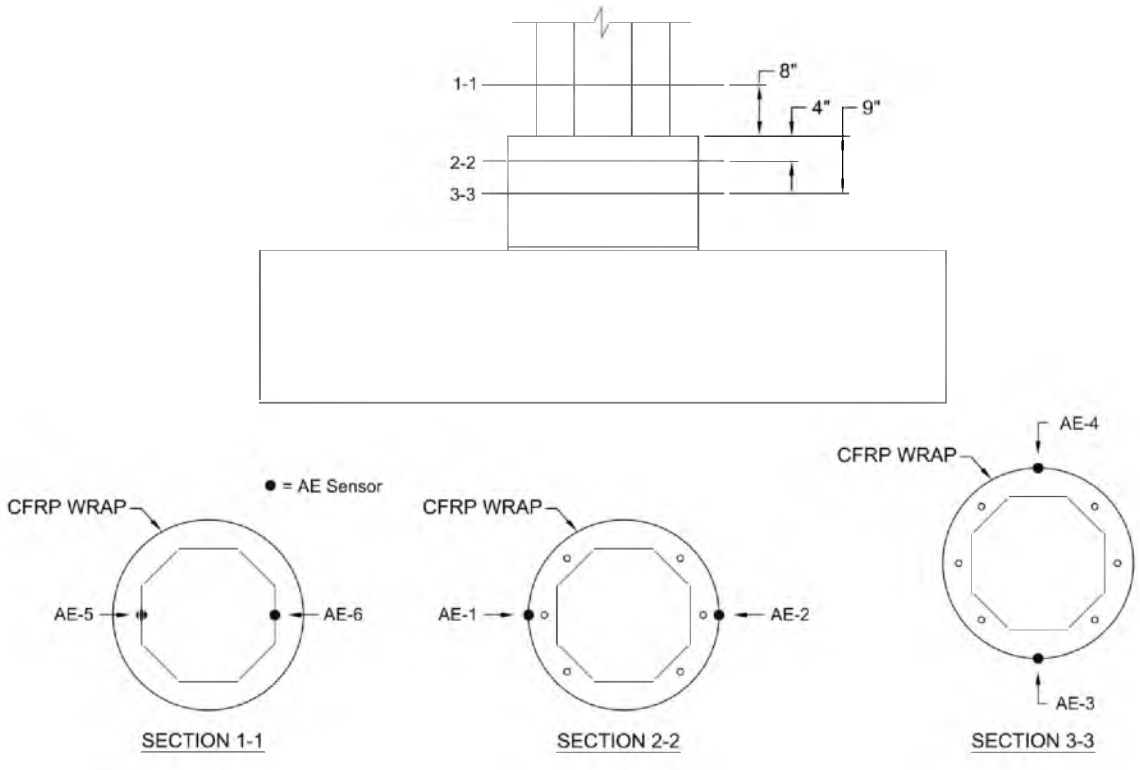

Figure 109. PCLEN-2R AE Sensor Layout

of the CFRP jacket had begun. In Figure 110, the AE history for sensor AE-1 is shown. AE-1 was located right above the crack and was able to record all of the events produced by the crack. All the other sensors located on the CFRP jacket recorded very few events and showed no correlation to the damage observed. In Figure 110, it is clear that a dramatic increase of AE events occurs half way through the test and recurs every cycle. To better understand exactly where in the cycle the increase in AE events is happening, Figure 111 shows the AE history of the last half of the test only. In this figure, it can be seen that that there is an increase in AE events every time the column is pushed to the east putting tension on the west face of the repair. This increase in AE events occurs right after the column moves through zero displacement, well before it reaches the displacement level previously attained showing no sign of the Kaiser effect.

From the AE history, it is difficult to assess how much damage is being done to the CFRP jacket with each push, but it does give a good indication of the presence and accumulation of the damage. The AE monitoring in this case helped to identify the general location of where damage was occurring in the CFRP jacket and when this occured by reviewing the AE event history,

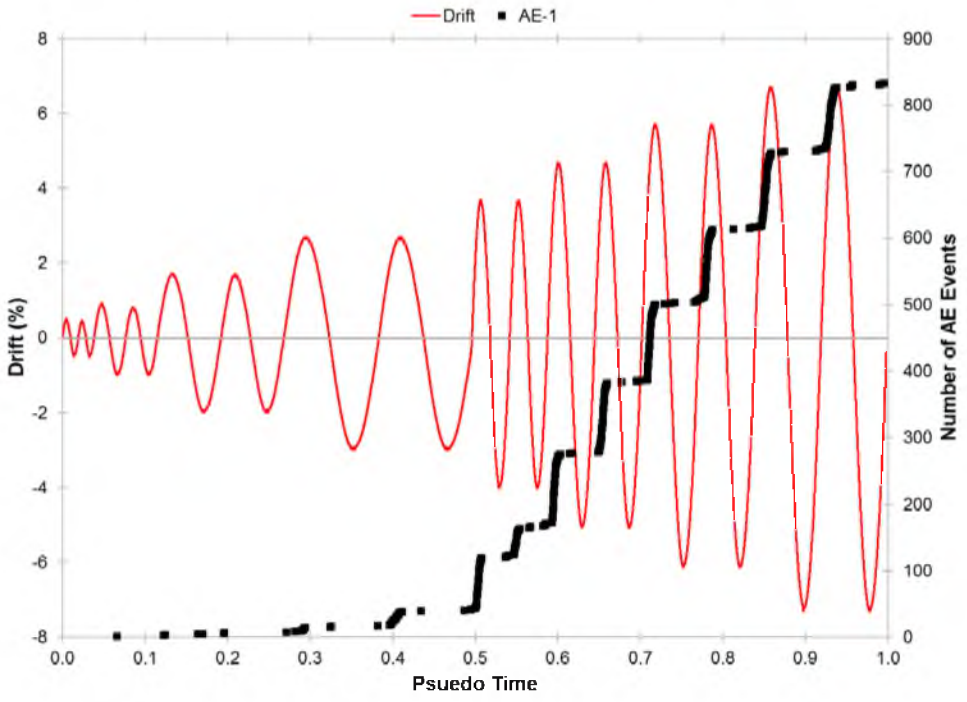

Figure 110. PCLEN-2R Cyclic Test AE Events History

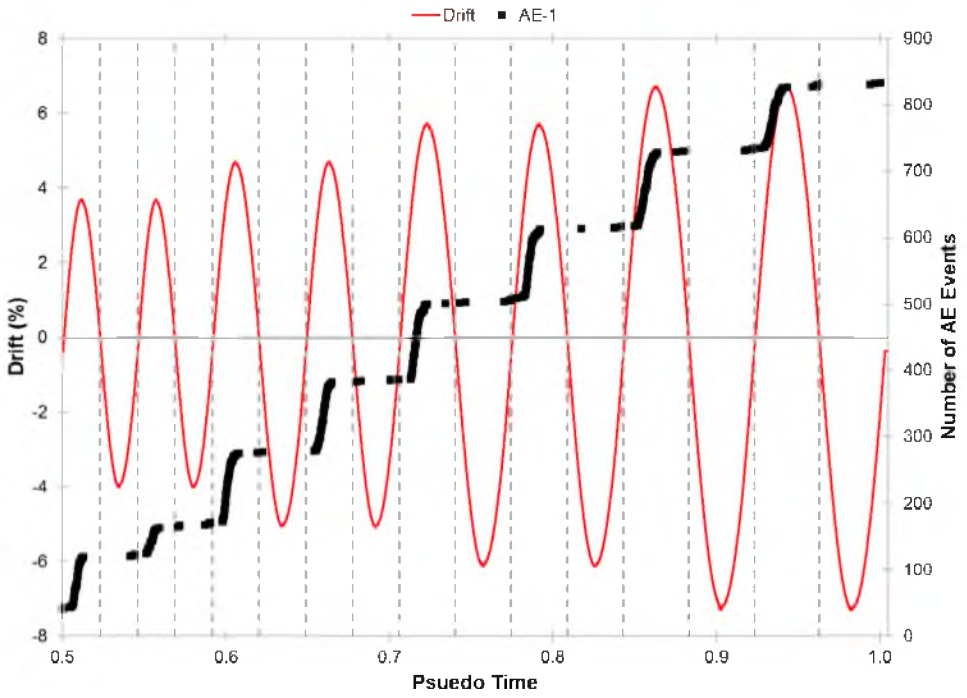

Figure 111. PCLEN-2R AE Event History Last Half of Cyclic Test

which otherwise may not have been detected.

4.1.6 Strut and Tie Model

4.1.6.1 PCLEN-2 Strut and Tie Model

A strut and tie model (STM) was created using the material properties in Table 9, which represents PCLEN-2 and is shown in Figure 112. In Figure 112 the struts are represented with dashed lines and the ties are represented with solid lines. The forces in the struts and ties are also presented in (kip) units adjacent to the respective strut or tie denoted by the symbol (k). The forces in the ties are considered negative and this is represented by the force being placed in parenthesis.

The layout of the nodes and the location of the struts and ties were determined based on the layout of the reinforcing steel along with the failure mode that was observed. This model was developed considering the ultimate horizontal load capacity of the column, which does not occur at the ultimate drift where a bar fractures, but instead at an intermediate drift when the concrete

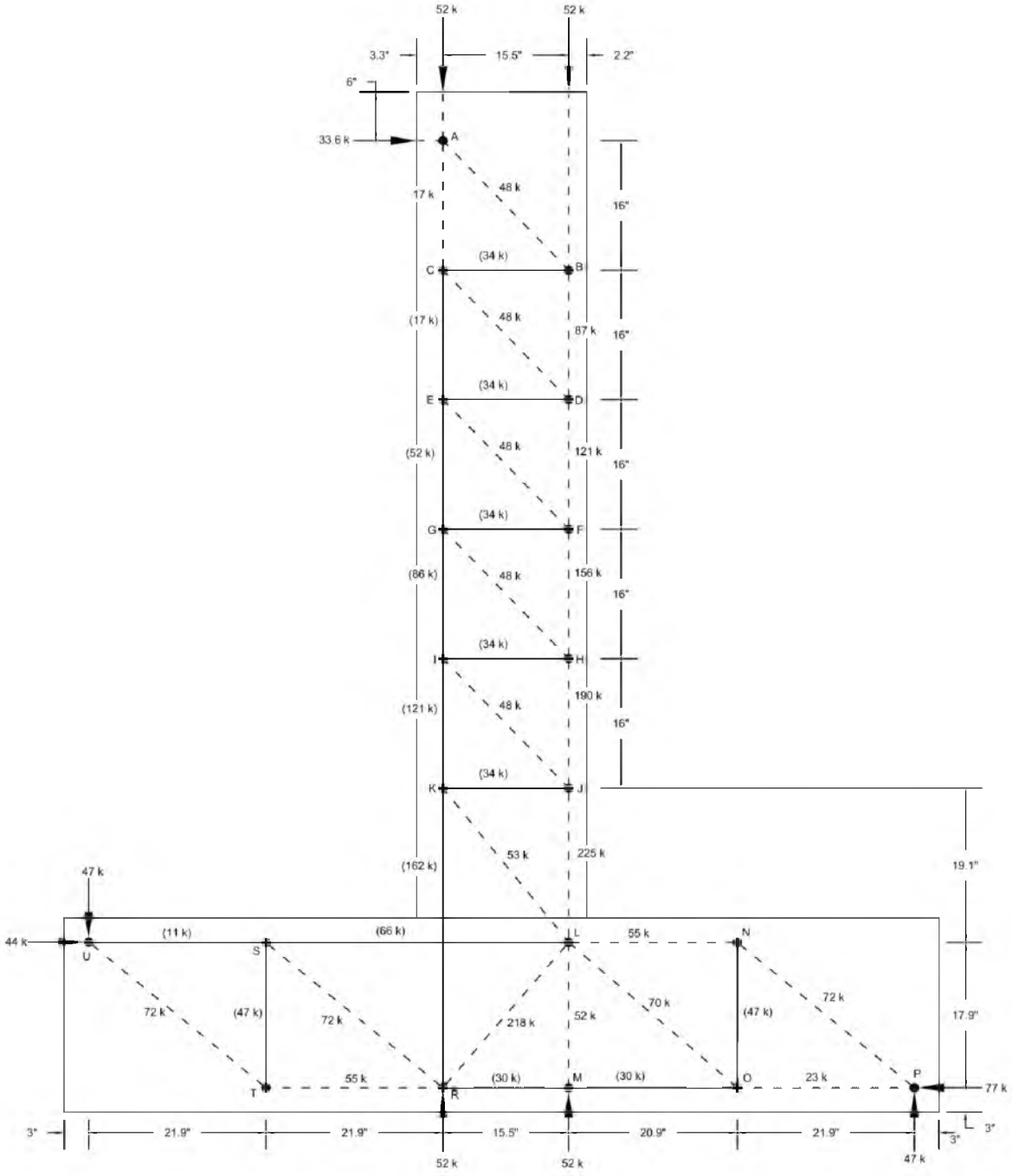

Figure 112. PCLEN-2 STM

begins to crush at the column to pier cap interface. This is supported by the test results of PCLEN-2 where the maximum horizontal load of 34.73 kips occurred at a drift of 3.8 percent, and failure did not occur until a drift of 6.8 percent where a longitudinal bar in the column fractured. Therefore, it would be reasonable to place struts B-D, D-F, F-H, H-J, and J-L at an appropriate distance away from the column face so that they crush.

Without knowing any other forces in the STM, there are an unlimited number of distances from the column face where strut J-L would crush given enough horizontal load. To determine the force in strut J-L at the ultimate horizontal load, the force in tie K-R was calculated using moment curvature analysis obtained from the test results of PCLEN-2. Using the curvature at a section just above the pier cap, the strains in the tension steel were calculated at the time of maximum lateral load (*6*). From these strains, a tie force of 162 kips was obtained for tie K-R which corresponds to a strut force of 225 kips in strut J-L. Using a strut force of 225 kips the required area of strut J-L was computed and the struts on the compression side of the column were placed a distance away from the column face where strut J-L would crush. In the case of PCLEN-2, this distance is 2.2 in. from the column face..

The required area of a strut is based on the strut compressive strength. The compressive strength of a strut, F_{ns}, is given by equation 8.

$$F_{ns} = f_{ce} \cdot A_{cs} \tag{8}$$

where:

A_{cs} : is the cross-sectional area of one end of the strut

f_{ce} : is the smaller of the effective compressive strength of the strut, equation 9, and the effective compressive strength of the node, equation 10.

The effective compressive strength of the strut is given by equation 9 for f'_c not greater than 6000 psi.

$$f_{ce} = 0.85 \cdot \beta_s \cdot f'_c \tag{9}$$

where:

β_s : assuming bottle shaped strut $\beta_s = 0.75$

f'_c : compressive strength of concrete, 6000 psi

The effective compressive strength of the node is given by equation 10.

$$f_{ce} = 0.85 \cdot \beta_n \cdot f'_c \quad (10)$$

where:

β_n : nodes not anchoring any ties $\beta_n = 1$, nodes anchoring one tie $\beta_n = 0.8$, nodes anchoring two or more ties $\beta_n = 0.6$

f'_c : compressive strength of concrete, 6000 psi

Therefore, the minimum required area of a strut is given in equation 11.

$$A_{cs,min} = \frac{F_u}{\min(0.85 \cdot \beta_s \cdot f'_c \ , \ 0.85 \cdot \beta_n \cdot f'_c)} \quad (11)$$

where:

F_u : is the force in the strut

Using equations 9-11, the minimum required area for each strut can be calculated and compared to the strut area that can be provided. The results from these calculations are shown in Table 12 for the struts located in the column, and in Table 13 for the struts located in the pier cap. In these tables, the strut thickness is determined from the location of the strut. In the column, for example, for strut A-B the thickness of the concrete at node A is 21 in., but at node B it is only 13.4 in. creating different strut areas on either end of the strut. A strut width is then determined based on the geometry of the member which when multiplied by the strut thickness gives the strut area. In the case of struts B-D, D-F, F-H, H-J, and J-L, there is an available maximum strut width of 4.4 in. since the struts are placed 2.2 in. from the face of the column.

Figure 113 is a visual representation of Tables 12 and 13 and shows the required strut widths in both the column and pier cap. Note that the width of strut H-J does not reach the face of the column, which from Table 12 has a width of 3.75 in. which is less than the maximum strut width of 4.4 in.

The ties in the column were checked to ensure that none of the ties are over stressed.

Table 12. PCLEN-2 Strut Sizes in Column

Member		Force (kips)	f_{ce} for Strut (ksi)	β_n	f_{ce} for Node (ksi)	$A_{CS,min}$ (in^2)	Strut Thickness (in)	Strut Width (in)	A_{CS} (in^2)	$A_{cs} > A_{cs,min}$
Vertical Strut At A		52	3.825	1	5.1	13.6	21.0	0.75	15.8	OK
Horizontal Strut At A		33.6	3.825	1	5.1	8.8	21.0	0.50	10.5	OK
A-B	@ A	48	3.825	1	5.1	12.5	21.0	1.00	21.0	OK
	@ B	48	3.825	0.8	4.08	12.5	13.4	1.00	13.4	OK
A-C	@ A	17	3.825	1	5.1	4.4	21.00	0.50	10.5	OK
	@ C	17	3.825	0.8	4.08	4.4	13.40	0.50	6.7	OK
Vertical Strut At B		52	3.825	0.8	4.08	13.6	13.4	1.25	16.8	OK
B-D	@ B	87	3.825	0.8	4.08	22.7	13.40	1.75	23.5	OK
	@ D	87	3.825	0.8	4.08	22.7	13.40	1.75	23.5	OK
C-D	@ C	48	3.825	0.6	3.06	15.7	13.40	1.25	16.8	OK
	@ D	48	3.825	0.8	4.08	12.5	13.40	1.25	16.8	OK
D-F	@ D	121	3.825	0.8	4.08	31.6	13.40	2.50	33.5	OK
	@ F	121	3.825	0.8	4.08	31.6	13.40	2.50	33.5	OK
F-H	@ F	156	3.825	0.8	4.08	40.8	13.40	3.25	43.6	OK
	@ H	156	3.825	0.8	4.08	40.8	13.40	3.25	43.6	OK
H-J	@ H	190	3.825	0.8	4.08	49.7	13.40	3.75	50.3	OK
	@ J	190	3.825	0.8	4.08	49.7	13.40	3.75	50.3	OK
J-L	@ J	225	3.825	1	5.1	59.0	13.40	4.40	59.0	Crush
	@ L	225	3.825	0.8	4.08	59.0	13.40	4.40	59.0	Crush

Table 13. PCLEN-2 Strut Sizes in Pier cap

Member		Force (kips)	f_{ce} for Strut (ksi)	β_n	f_{ce} for Node (ksi)	$A_{CS,min}$ (in^2)	Strut Thickness (in)	Strut Width (in)	A_{CS} (in^2)	$A_{cs} > A_{cs,min}$
L-M	@ L	52	3.825	0.8	4.08	13.6	24.00	0.75	18.0	OK
	@ M	52	3.825	0.6	3.06	17.0	24.00	0.75	18.0	OK
L-N	@ L	55	3.825	0.8	4.08	14.4	24.00	0.75	18.0	OK
	@ N	55	3.825	0.8	4.08	14.4	24.00	0.75	18.0	OK
L-O	@ L	70	3.825	0.8	4.08	18.3	24.00	1.00	24.0	OK
	@ O	70	3.825	0.6	3.06	22.9	24.00	1.00	24.0	OK
L-R	@ L	218	3.825	0.8	4.08	57.0	24.00	3.00	72.0	OK
	@ R	218	3.825	0.6	3.06	71.2	24.00	3.00	72.0	OK
N-P	@ N	72	3.825	0.8	4.08	18.8	24.00	1.00	24.0	OK
	@ P	72	3.825	1	5.1	18.8	24.00	1.00	24.0	OK
O-P	@ O	23	3.825	0.6	3.06	7.5	24.00	0.50	12.0	OK
	@ P	23	3.825	1	5.1	6.0	24.00	0.50	12.0	OK
R-S	@ R	72	3.825	0.6	3.06	23.5	24.00	1.00	24.0	OK
	@ S	72	3.825	0.6	3.06	23.5	24.00	1.00	24.0	OK
R-T	@ R	55	3.825	0.6	3.06	18.0	24.00	0.75	18.0	OK
	@ T	55	3.825	0.8	4.08	14.4	24.00	0.75	18.0	OK
T-U	@ T	72	3.825	0.8	4.08	18.8	24.00	1.00	24.0	OK
	@ U	72	3.825	0.8	4.08	18.8	24.00	1.00	24.0	OK

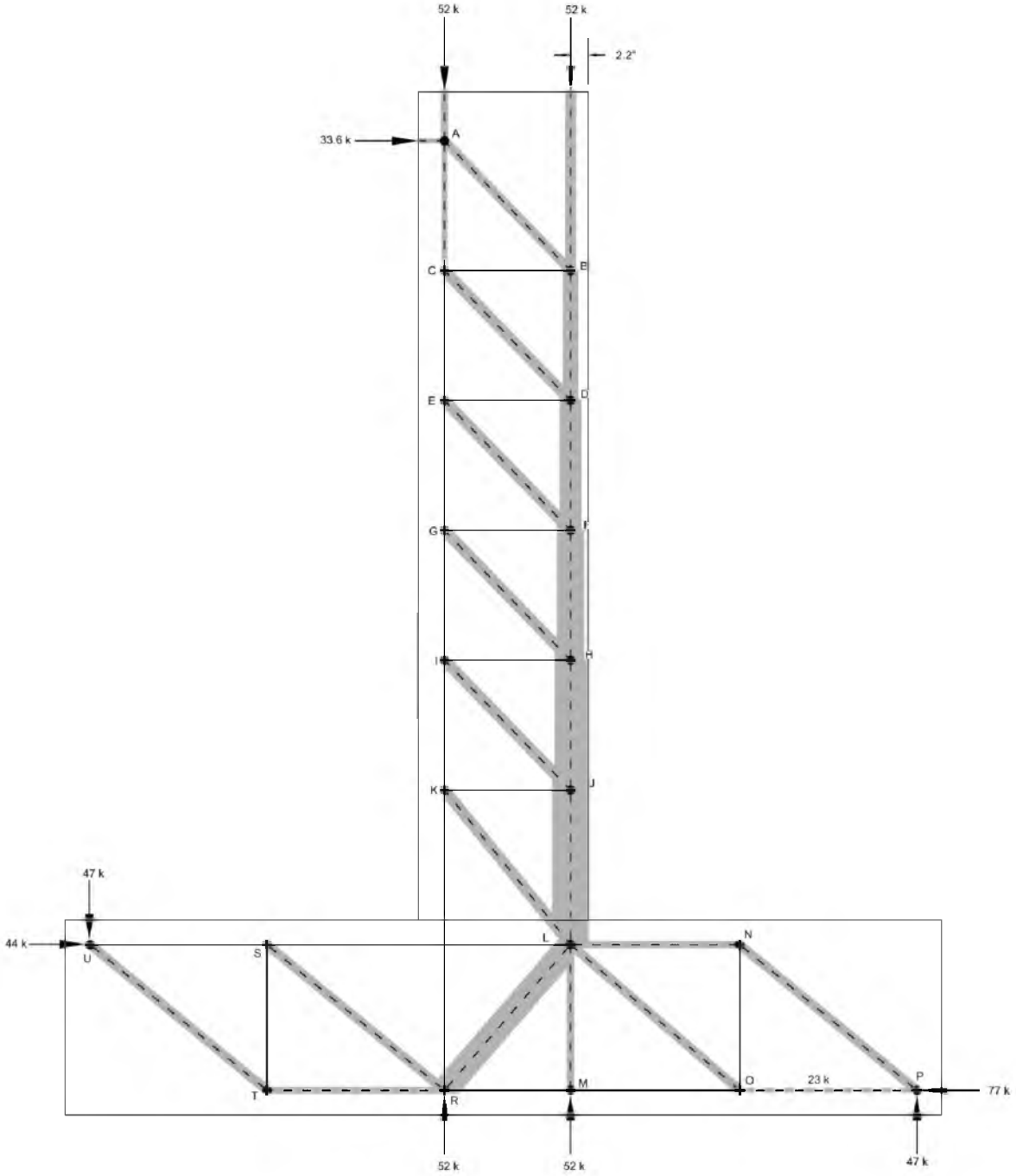

Figure 113. PCLEN-2 STM Strut Width

The ties were checked at both the yield stress, f_y, and fracture stress, f_u, using equations 12 and 13, respectively.

$$A_{sy,min} = \frac{F_u}{0.75 * f_y} \quad (12)$$

$$A_{su,min} = \frac{F_u}{0.75 * f_u} \quad (13)$$

Using equations 12 and 13, the minimum area of steel required for each tie can be calculated and compared to the area of steel provided. The results from these calculations are shown in Table 14 for the ties located in the column, and in Table 15 for the ties located in the pier cap. Note that ties E-D, G-F, and I-H have the same force and actual steel as tie C-B. From Tables 14 and 15, there are no ties that have fractured and only ties I-K and K-R have yielded, which is supported by strain gage data from the PCLEN-2 test results.

To verify the accuracy of the model, the horizontal load calculated to cause strut J-L to crush in the STM is compared to the maximum horizontal load from the test results of PCLEN-2. The horizontal load at which strut J-L is calculated to crush is 33.6 kips. With a horizontal load of 34.74 kips obtained from the cyclic test results of PLCEN-2, the STM predicts 97 percent of this load. Since the maximum horizontal load from PCLEN-2 is obtained from cyclic testing, it would be expected that the maximum horizontal load from a monotonic pushover test would be higher. Therefore, although the direct comparison of the strut and tie to the PCLEN-2 results are not the best comparison, the strut and tie model shows it is conservative.

4.1.6.2 PCLEN-2R Strut and Tie Model

The same procedure used to develop the STM for PCLEN-2 was used to also develop a STM for PCLEN-2R. Since the column cross-section in the plastic hinge region is the same for both PCLEN-2 and PCLEN-2R, the struts on the compressive face of the column in the STM for PCLEN-2R are considered to be 2.2 in. from the column face just like in the STM for PCLEN-2. Figure 114 shows the STM for PCLEN-2R. In the STM for PCLEN-2R, there is no tie which represents the longitudinal reinforcement in the column that crosses over into the pier cap. This is

Table 14. PCLEN-2 Tie Steel In Column

Member	Force (kips)	$A_{sy,min}$ (in^2)	$A_{su,min}$ (in^2)	Actual A_s (in^2)
Tie C-B	34	0.67	0.49	3
Tie C-E	17	0.33	0.24	2.37
Tie E-G	52	1.02	0.75	2.37
Tie G-I	86	1.69	1.23	2.37
Tie I-K	121	2.37	1.73	2.37
Tie K-R	162	3.18	2.32	2.37

Table 15. PCLEN-2 Tie Steel In Pier cap

Member	Force (kips)	$A_{sy,min}$ (in^2)	$A_{su,min}$ (in^2)	Actual A_s (in^2)
Tie L-S	66	1.29	0.95	10
Tie S-U	11	0.22	0.16	10
Tie R-M	30	0.59	0.43	8
Tie M-O	30	0.59	0.43	10
Tie N-O	47	0.92	0.67	12
Tie S-T	47	0.92	0.67	12

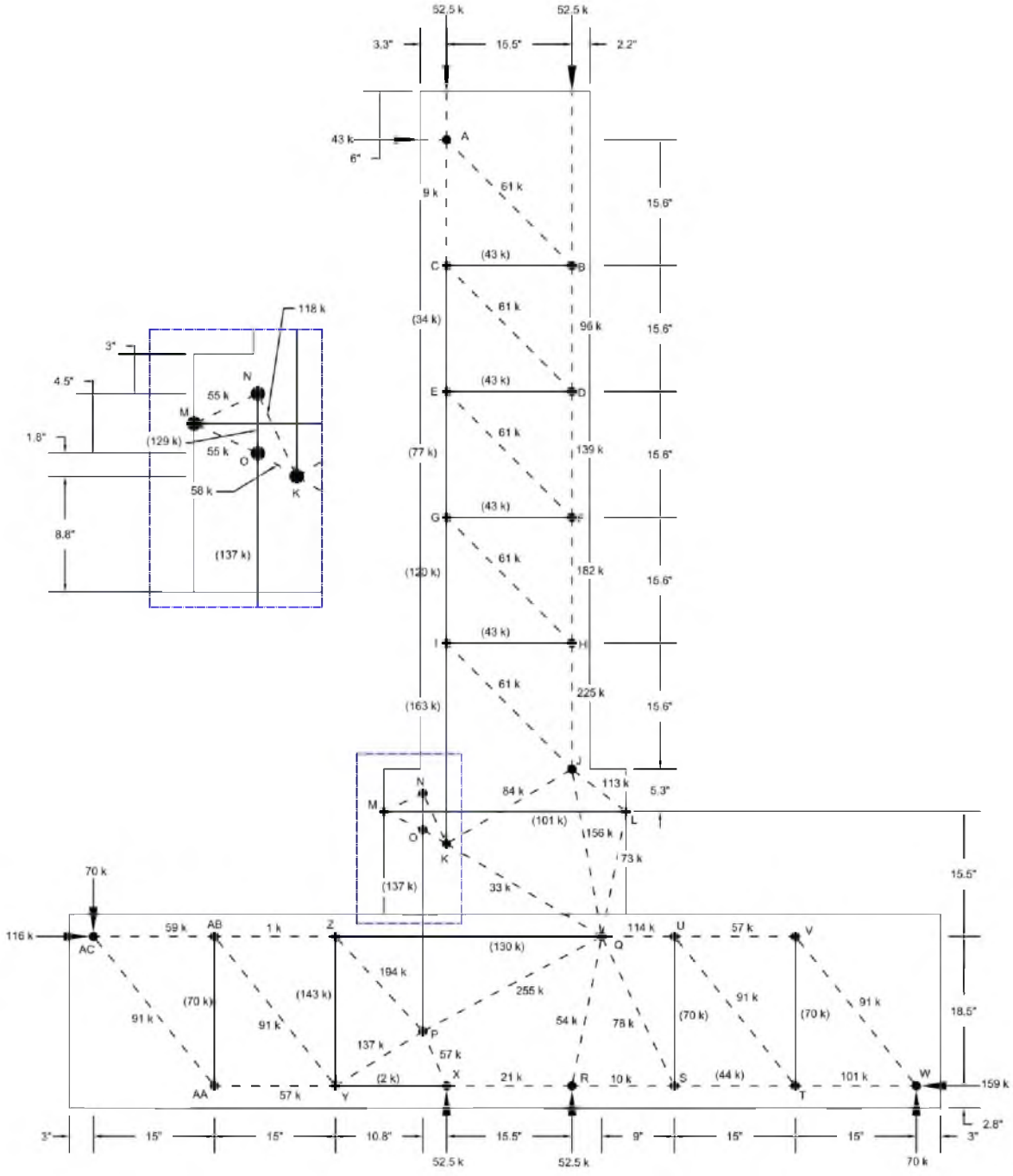

Figure 114. PCLEN-2R STM

because the extreme bar in the original specimen PCLEN-2 had fractured just above the pier cap, as shown in Figure 80. Instead, all the tension generated by bending is transferred to the pier cap by ties N-O, and O-P which represents three of the postinstalled headed bars. Since the headed bars were postinstalled, there is not a means to directly transfer the tension in the bars to the pier cap longitudinal reinforcement directly. Therefore, tie O-P is terminated above the bottom longitudinal reinforcement and subsequently anchored with struts P-Q, P-Y, P-Z, and P-X. Also, the CFRP jacket is represented in the STM by tie L-M, which transfers the tension across the repaired region to the headed bars.

The required sizes of the struts in the STM for PCLEN-2R are calculated as before by using equations 9 – 11.The results from these calculations are shown in Table 16 for the struts located in the column, Table 17 for the struts located in the repaired region, and Tables 18 and 19 for the struts located in the pier cap. Note that struts E-F, G-H, and I-J all have the same properties as strut C-D, and for this reason, they were not included. A graphical representation of these calculations is also shown in Figure 115 where the required minimum strut widths are drawn to scale on the STM.

The required area of steel for the ties is also calculated as before using equations 12 – 13. The results from these calculations are presented in Table 20 for ties located in the column, Table 21 for ties located in the repair region, and Table 22 for ties located in the pier cap. According to the STM ties I-K, N-O, and O-P yield while the rest of the ties in the STM remain elastic.

From the test results, it is known that the compression strut in the column just above the repair began to crush at the maximum lateral load. In the STM for PCLEN-2R, this failure mode is observed when a horizontal load of 43 kips is applied to the top of the column. The horizontal load calculated by the STM is the same horizontal load that was computed from extrapolating the base moment in section 4.1.3. To verify the accuracy of the STM, the horizontal load calculated by the STM is compared to the horizontal load from the monotonic pushover test results of PCLEN-2R. With an actual horizontal load of 46.88 kips from the monotonic pushover test results of PCLEN-2R the STM conservatively computed 92 percent of the monotonic pushover load.

Table 16. PCLEN-2R Strut Sizes in Column

Member		Force (kips)	f_{ce} for Strut (ksi)	β_n	f_{ce} for Node (ksi)	$A_{cs,min}$ (in^2)	Stut Thicnkess (in)	Strut Width (in)	A_{cs} (in^2)	$A_{cs} > A_{cs,min}$
Vertical Strut At A		52.5	3.825	1	5.1	13.7	21.0	0.75	15.8	OK
Horizontal Strut At A		43	3.825	1	5.1	11.2	21.0	0.75	15.8	OK
A-B	@ A	61	3.825	1	5.1	15.9	21.0	1.25	26.3	OK
	@ B	61	3.825	0.8	4.08	15.9	13.4	1.25	16.8	OK
A-C	@ A	9	3.825	1	5.1	2.4	21.0	0.25	5.3	OK
	@ C	9	3.825	0.8	4.08	2.4	13.4	0.25	3.4	OK
Vertical Strut At B		52.5	3.825	0.8	4.08	13.7	13.4	1.25	16.8	OK
B-D	@ B	96	3.825	0.8	4.08	25.1	13.4	2.00	26.8	OK
	@ D	96	3.825	0.8	4.08	25.1	13.4	2.00	26.8	OK
C-D	@ C	61	3.825	0.6	3.06	19.9	13.4	1.50	20.1	OK
	@ D	61	3.825	0.8	4.08	15.9	13.4	1.50	20.1	OK
D-F	@ D	139	3.825	0.8	4.08	36.3	13.4	2.75	36.9	OK
	@ F	139	3.825	0.8	4.08	36.3	13.4	2.75	36.9	OK
F-H	@ F	182	3.825	0.8	4.08	47.6	13.4	3.75	50.3	OK
	@ H	182	3.825	0.8	4.08	47.6	13.4	3.75	50.3	OK
H-J	@ H	225	3.825	0.8	4.08	59.0	13.4	4.40	59.0	Crush
	@ J	225	3.825	0.8	4.08	59.0	13.4	4.40	59.0	Crush

Table 17. PCLEN-2R Strut Sizes in Repair

Member		Force (kips)	f_{ce} for Strut (ksi)	β_n	f_{ce} for Node (ksi)	$A_{cs,min}$ (in^2)	Stut Thicnkess (in)	Strut Width (in)	A_{cs} (in^2)	$A_{cs} > A_{cs,min}$
J-Q	@ J	156	4.4625	1	5.95	35.0	21.00	1.75	36.75	OK
	@ Q	156	4.4625	0.8	4.76	35.0	21.00	1.75	36.75	OK
J-L	@ J	113	4.4625	1	5.95	25.3	21.00	2.25	47.25	OK
	@ L	113	4.4625	0.8	4.76	25.3	12.00	2.25	27.00	OK
J-K	@ J	84	4.4625	1	5.95	18.8	21.00	1.00	21.00	OK
	@ k	84	4.4625	0.8	4.76	18.8	21.00	1.00	21.00	OK
L-Q	@ L	73	4.4625	0.8	4.76	16.4	12.00	1.50	18.00	OK
	@ Q	73	4.4625	0.8	4.76	16.4	24.00	1.50	36.00	OK
M-N	@ M	55	4.4625	0.8	4.76	12.3	10.00	1.50	15.00	OK
	@ N	55	4.4625	0.8	4.76	12.3	22.00	1.50	33.00	OK
M-O	@ M	55	4.4625	0.8	4.76	12.3	10.00	1.50	15.00	OK
	@ O	55	4.4625	0.6	3.57	15.4	22.00	1.50	33.00	OK
N-K	@ N	118	4.4625	0.8	4.76	26.4	22.00	1.25	27.50	OK
	@ K	118	4.4625	0.8	4.76	26.4	22.00	1.25	27.50	OK
O-K	@ O	58	4.4625	0.6	3.57	16.2	22.00	0.75	16.50	OK
	@ K	58	4.4625	0.8	4.76	13.0	22.00	0.75	16.50	OK
K-Q	@ K	33	4.4625	0.8	4.76	7.4	22.00	0.50	11.00	OK
	@ Q	33	4.4625	0.8	4.76	7.4	24.00	0.50	12.00	OK

Table 18. PCLEN-2R Strut Sizes in Pier Cap

Member		Force (kips)	f_{ce} for Strut (ksi)	β_n	f_{ce} for Node (ksi)	$A_{cs,min}$ (in^2)	Stut Thicnkess (in)	Strut Width (in)	A_{cs} (in^2)	$A_{cs} > A_{cs,min}$
Q-R	@ Q	54	3.825	0.8	4.08	14.1	24.00	0.75	18.0	OK
	@ R	54	3.825	1	5.1	14.1	24.00	0.75	18.0	OK
Q-S	@ Q	78	3.825	0.8	4.08	20.4	24.00	1.00	24.0	OK
	@ S	78	3.825	0.8	4.08	20.4	24.00	1.00	24.0	OK
Q-U	@ Q	114	3.825	0.8	4.08	29.8	24.00	1.25	30.0	OK
	@ U	114	3.825	0.8	4.08	29.8	24.00	1.25	30.0	OK
R-S	@ R	10	3.825	1	5.1	2.6	24.00	0.25	6.0	OK
	@ S	10	3.825	0.8	4.08	2.6	24.00	0.25	6.0	OK
S-T	@ S	44	3.825	0.8	4.08	11.5	24.00	0.75	18.0	OK
	@ T	44	3.825	0.6	3.06	14.4	24.00	0.75	18.0	OK
U-T	@ U	91	3.825	0.8	4.08	23.8	24.00	1.00	24.0	OK
	@ T	91	3.825	0.8	4.08	23.8	24.00	1.00	24.0	OK
U-V	@ U	57	3.825	0.8	4.08	14.9	24.00	0.75	18.0	OK
	@ V	57	3.825	1.0	5.1	14.9	24.00	0.75	18.0	OK
T-W	@ T	101	3.825	0.8	4.08	26.4	24.00	1.25	30.0	OK
	@ W	101	3.825	1.0	5.1	26.4	24.00	1.25	30.0	OK
V-W	@ V	91	3.825	0.8	4.08	23.8	24.00	1.00	24.0	OK
	@ W	91	3.825	1	5.1	23.8	24.00	1.00	24.0	OK

Table 19. Strut Sizes in Pier Cap Cont.

Member		Force (kips)	f_{ce} for Strut (ksi)	β_n	f_{ce} for Node (ksi)	$A_{CS,min}$ (in^2)	Stut Thicnkess (in)	Strut Width (in)	A_{CS} (in^2)	$A_{cs} > A_{cs,min}$
Q-P	@ Q	255	3.825	0.8	4.08	66.7	24.00	3.00	72.0	OK
	@ P	255	3.825	0.8	4.08	66.7	24.00	3.00	72.0	OK
R-X	@ R	21	3.825	1	5.1	5.5	24.00	0.25	6.0	OK
	@ X	21	3.825	0.8	4.08	5.5	24.00	0.25	6.0	OK
P-X	@ P	57	3.825	0.8	4.08	14.9	24.00	0.75	18.0	OK
	@ X	57	3.825	0.8	4.08	14.9	24.00	0.75	18.0	OK
P-Y	@ P	137	3.825	0.8	4.08	35.8	24.00	2.25	54.0	OK
	@ Y	137	3.825	0.6	3.06	44.8	24.00	2.25	54.0	OK
P-Z	@ P	194	3.825	0.8	4.08	50.7	24.00	2.75	66.0	OK
	@ Z	194	3.825	0.6	3.06	63.4	24.00	2.75	66.0	OK
Y-AA	@ Y	57	3.825	0.6	3.06	18.6	24.00	1.00	24.0	OK
	@ AA	57	3.825	0.8	4.08	14.9	24.00	1.00	24.0	OK
Y-AB	@ Y	91	3.825	0.6	3.06	29.7	24.00	1.25	30.0	OK
	@ AB	91	3.825	0.8	4.08	23.8	24.00	1.25	30.0	OK
AB-AC	@ AB	59	3.825	0.8	4.08	15.4	24.00	0.75	18.0	OK
	@ AC	59	3.825	1.0	5.1	15.4	24.00	0.75	18.0	OK
AA-AC	@ AA	91	3.825	0.8	4.08	23.8	24.00	1.00	24.0	OK
	@ AC	91	3.825	1.0	5.1	23.8	24.00	1.00	24.0	OK

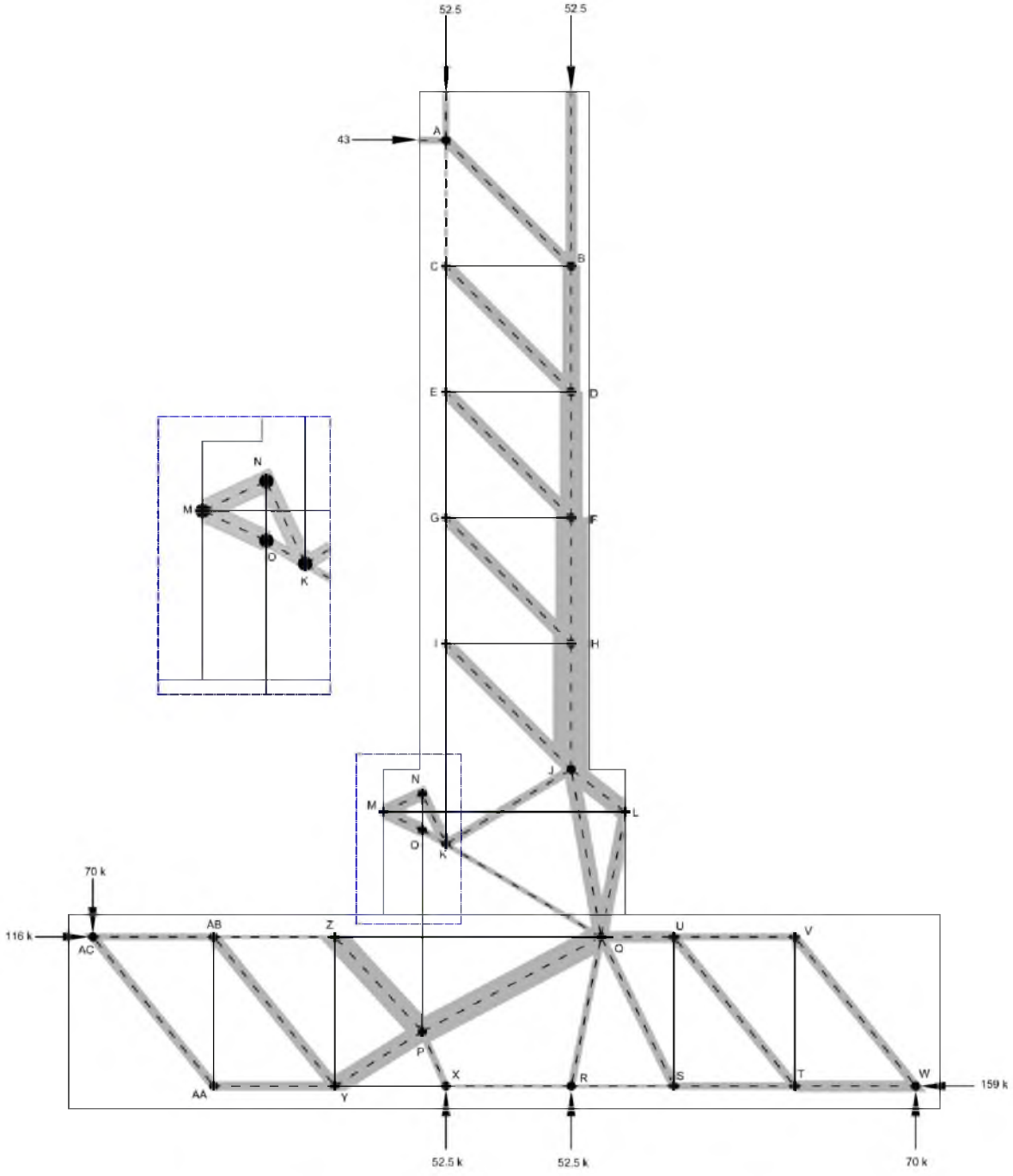

Figure 115. PCLEN-2R STM Strut Widths

Table 20. PCLEN-2R Ties in Column

Member	Force (kips)	$A_{sy,min}$ (in^2)	$A_{su,min}$ (in^2)	Actual A_s (in^2)
Tie C-B	43	0.91	0.56	3
Tie C-E	34	0.67	0.49	2.37
Tie E-G	77	1.51	1.10	2.37
Tie G-I	120	2.35	1.72	2.37
Tie I-K	163	3.20	2.34	2.37

Table 21. PCLEN-2R Ties in Repair

Ties In Donut				
Member	Force (kips)	$A_{sy,min}$ (in^2)	$A_{su,min}$ (in^2)	Actual A_s (in^2)
Headed bar Tie N-O	129	2.77	2.00	2.37
Headed bar Tie O-P	137	2.95	2.12	2.37
Wrap Tie L-M	101	--	1.01*	3.4**

* Minimum Area of CFRP

** Actual Area of CFRP

Table 22. PCLEN-2R Ties in Pier Cap

Member	Force (kips)	$A_{sy,min}$ (in^2)	$A_{su,min}$ (in^2)	Actual A_s (in^2)
Tie Q-Z	130	2.55	1.86	10
Tie Z-Y	143	3.03	1.85	12
Tie Y-X	2	0.04	0.03	8
Tie U-S	70	1.37	1.00	12
Tie V-T	70	1.37	1.00	12
Tie AA-AB	70	1.48	0.91	12

4.1.7 PCLEN-3 Repair

To verify the results of the design procedure, a second column to pier cap connection denoted as PCLEN-3 was tested to failure and subsequently repaired. PCLEN-3 consisted of the same reinforcement and grouted splice sleeve location as PCLEN-1 shown in Figure 53. The concrete used for PCLEN-3, however, was much stronger than the concrete used previously with a compressive strength of 9 ksi. The failure mode of PCLEN-3 was similar to PCLEN-1 where the field dowels pulled out of the splice sleeve on both sides of the column. Due to this failure mode and the stronger concrete, damage to the rest of the column above the splice sleeves was much less severe compared to PCLEN-2. The repaired PCLEN-3 specimen is designated as PCLEN-3R.

The same postinstalled bar layout and repair procedure used for PCLEN-2R was used for PCLEN-3R. There were, however, two modifications made to the design in an attempt to negate the transverse cracks in the CFRP. The first change was to add an additional 1 in. of length to the postinstalled headed bars in the repaired region in order to lessen the distance from the top of the CRFP jacket to the top of the headed bars. The second change was the use of expansive concrete instead of nonshrink concrete in an attempt to posttension the CFRP jacket and increase the confining pressure. The mix design for the expansive concrete is shown in Table 23.

Strain gages on the CFRP wrap as shown in Figure 92 were used to measure the posttensioning of the CFRP jacket while the expansive concrete cured. Figure 116 shows the average strain in the CFRP jacket from when the concrete was cast to the day of the test, which was 21 days. The maximum average strain caused by the expansion of the concrete was 0.0013 in./in., which is 12 percent of the ultimate strain capacity of the CFRP composite.

PCLEN-3 was loaded to failure using the loading protocol in Figure 56. The results from the cyclic test are shown by the hysteresis in Figure 117. Although measures were taken to try and prevent transverse cracking of the CFRP jacket, it still occurred. The cycle where transverse cracking begins is shown by a box in Figure 117. Similar to PCLEN-2R, the transverse crack developed right at the top of the postinstalled headed bars, but unlike PCLEN-2R there were

Table 23. PCLEN-3R Expansive Concrete Mix Design

Component		Weight (lb)
Cement	Portland Cement	201
	Komponant	150
Water	Weight	140
Rock	3/4" minus gravel	818.5
Sand	Weight	579.5
Additives	glenium 30-30	1.53
	daravair	0.2

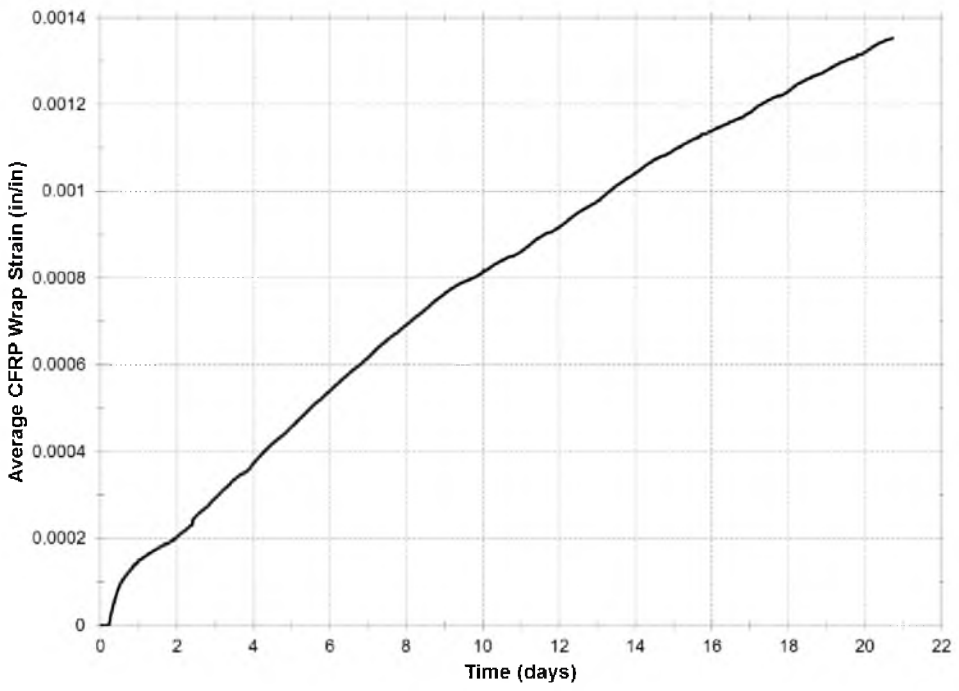

Figure 116. Average CFRP Wrap Strain from Concrete Expansion

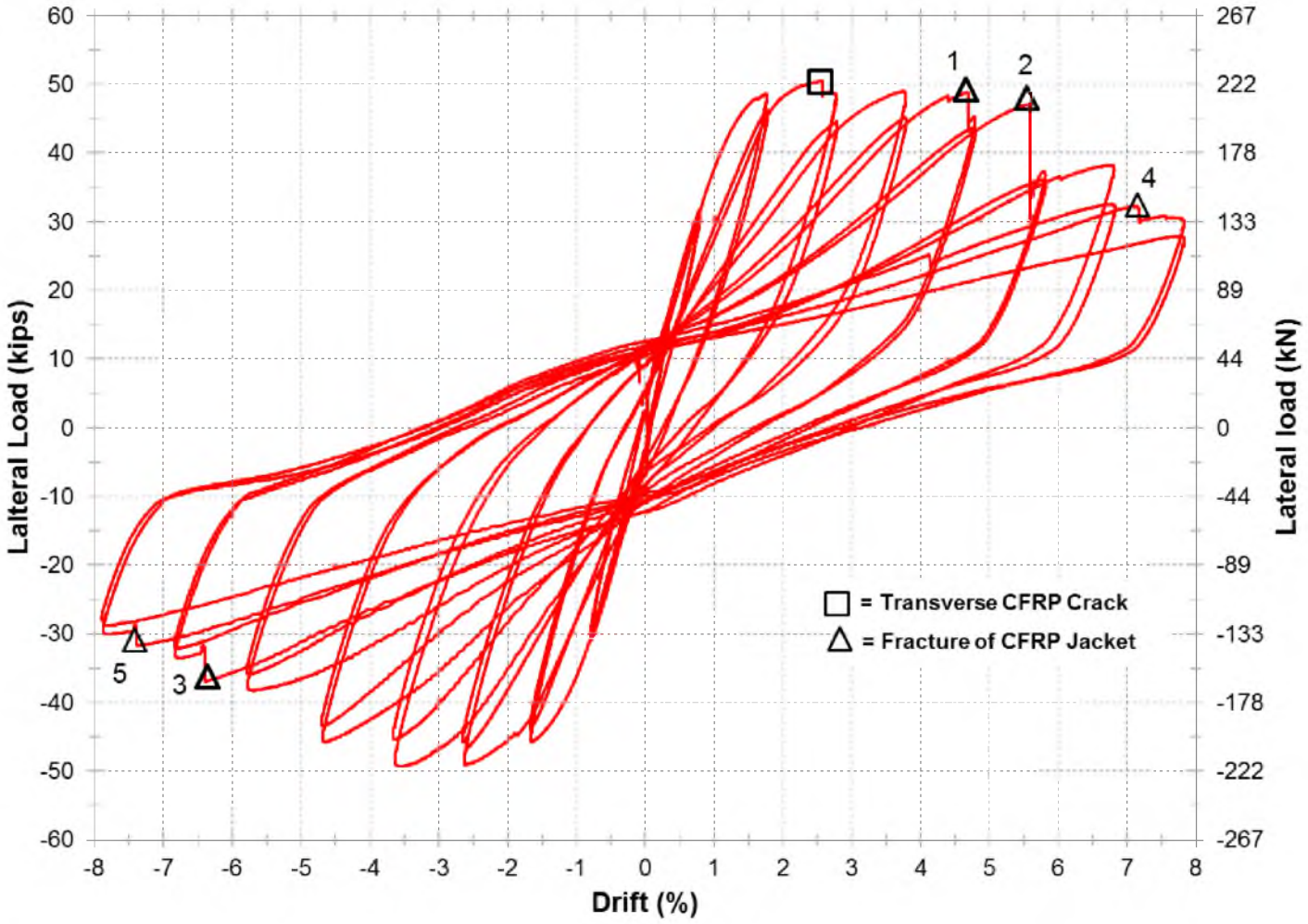

Figure 117. PCLEN-3R Hysteresis

multiple layers of transverse cracking with one crack extending around the entire circumference of the CFRP jacket. The cracking of the CFRP jacket is shown in Figure 118. The transverse crack is thought to have occurred on both sides of the column in this test, because both extreme longitudinal bars had pulled out in the original test causing additional demand on both sides of the column.

Before the plastic hinge was moved to the top of the repair, a 3 in. wide portion of the CFRP jacket broke on the east side of the column, as shown in Figure 119. The point at which this strip broke is denoted by triangle 1 on the hysteresis, which is at a drift of 4.5 percent. Once this small strip broke, there was a small decrease in load capacity, which was not significant. On the first push of the 6 percent drift cycle, however, a major portion of the CFRP jacket broke, as shown in Figure 120, which is denoted as triangle 2 on the hysteresis. The second break in the CFRP jacket caused the lateral load capacity of PCLEN-3R to drop below 20 percent of the maximum lateral load capacity. This drop of greater than 20 percent of the maximum lateral load is taken as the point of failure for PCLEN-3R, but to observe what would happen to the repair, the test was continued. Since tensile fracture of the CFRP jacket affected the lateral load so drastically, the importance of the tie L-M in the STM for PCLEN-2R is shown.

As the test continued, the jacket fractured three additional times, with each fracture moving towards the pier cap. The final damage state of PCLEN-3R is shown in Figure 121. In this figure, it can be seen that by the end of the test all but a 4 in. band of CFRP at the top of the repair and a 5 in. band of CFRP at the bottom of the repair is all that remains of the CFRP jacket, which is intact and bonded to the expansive concrete. The rest of the jacket in the middle of the repair has fractured.

It can also be seen in Figure 121 that the column section which was visible remained relatively undamaged. There was one major structural crack which occurred right above the repair and is traced in blue. This crack was 0.03 in. wide and extended all the way around the column cross-section. In this figure, only a small portion of this crack can be seen, because once the initial transverse crack extended the entire circumference of the repair, the small band above the crack began to behave independently from the rest of the repair. As the drift level was

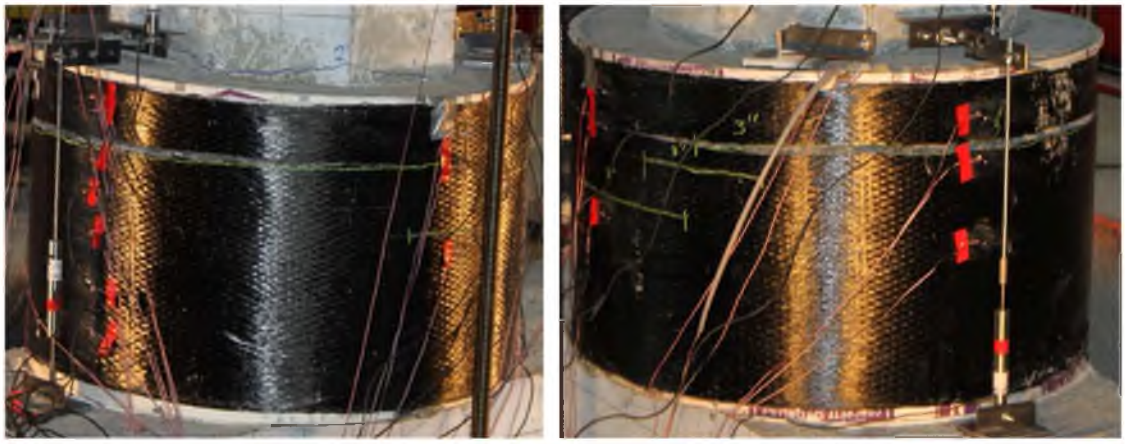

(a) (b)

Figure 118. Transverse CFRP Crack: (a) West Side of Jacket; (b) East Side of Jacket

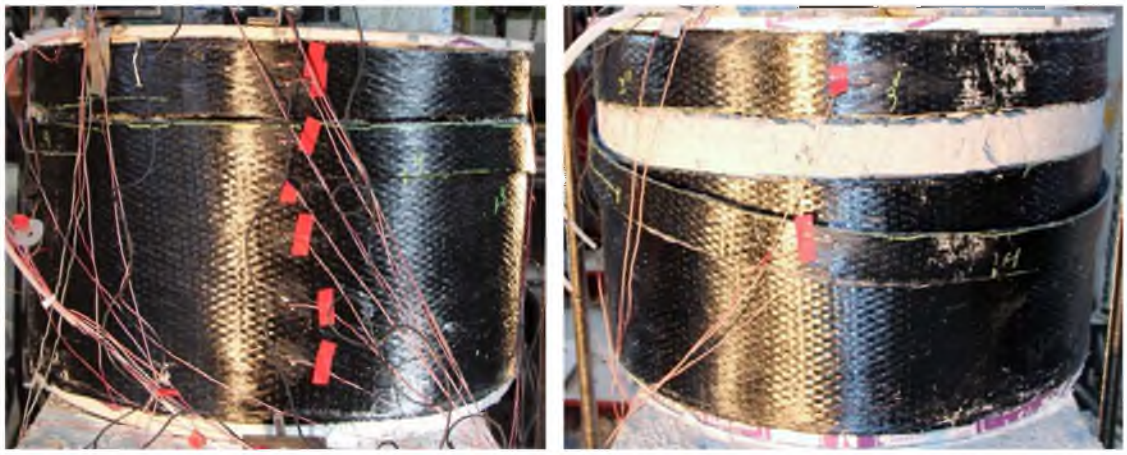

(a) (b)

Figure 119. PCLEN-3R First Jacket Fracture: (a) West Side of Jacket;(b) East Side of Jacket

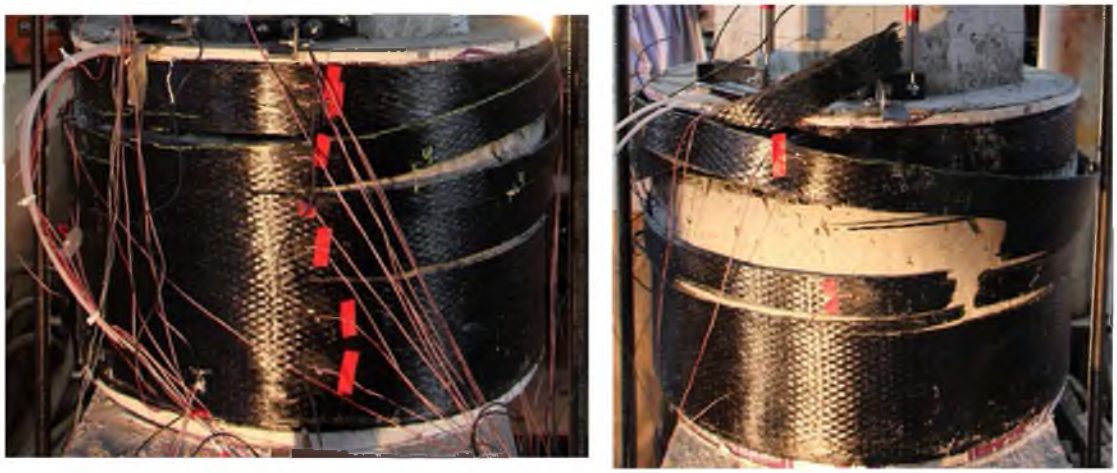

(a) (b)

Figure 120. PCLEN-3R Second Jacked Fracture: (a) West Side of Jacket;(b) East Side of Jacket

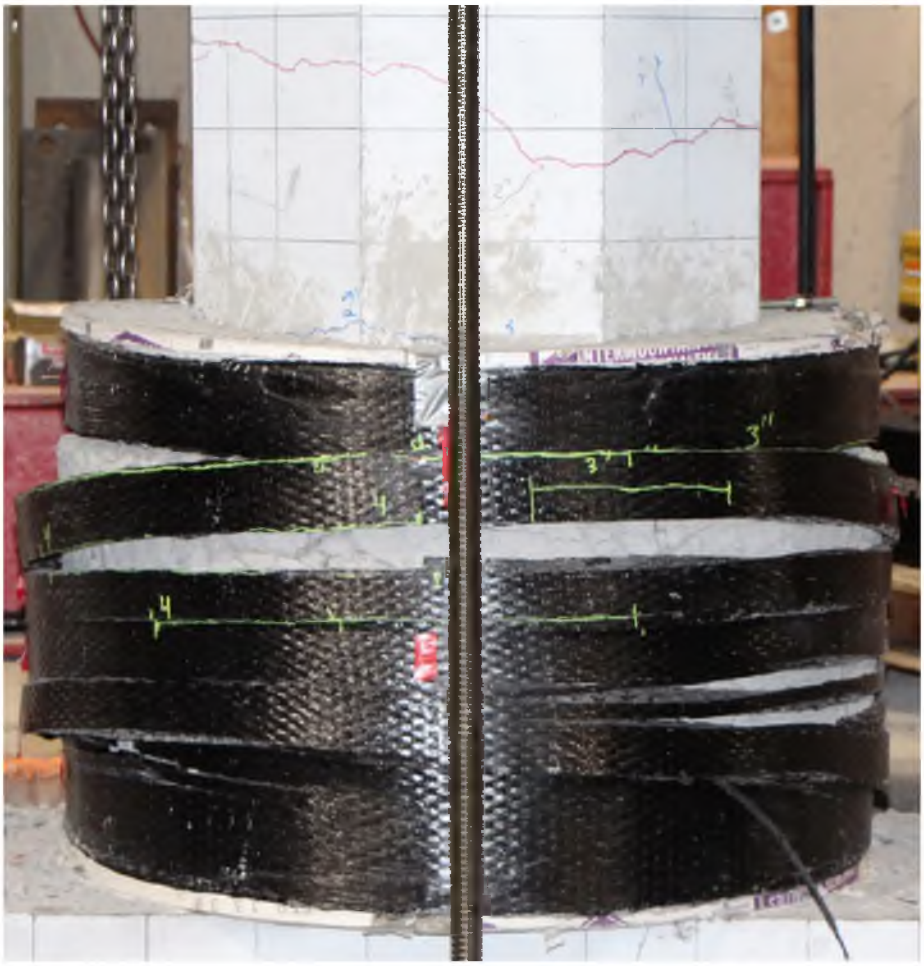

Figure 121. PCLEN-3R Final Damage

increased, this band began to slide up the column eventually covering up the crack.

Although the failure mode of PCLEN-3R was not intended and the plastic hinge was not relocated entirely above the repaired region, the specimen still showed a good performance. Figure 122 shows the backbone curve for PCLEN-3R with the idealized elastoplastic curves superimposed. Failure of PCLEN-3R was considered when the lateral load dropped below 20 percent of the maximum lateral load which occurred at a drift of 5.6 percent in the push direction and a drift of 4.6 percent in the pull direction. Using the equal area method to estimate the idealized elastoplastic curve, the yield drifts were computed as 1.3 percent and 1.0 percent for the push and pull direction, respectively. This results in a displacement ductility of 4.2 in the push direction and 4.6 in the pull direction. Considering that Caltrans limits the displacement ductility of

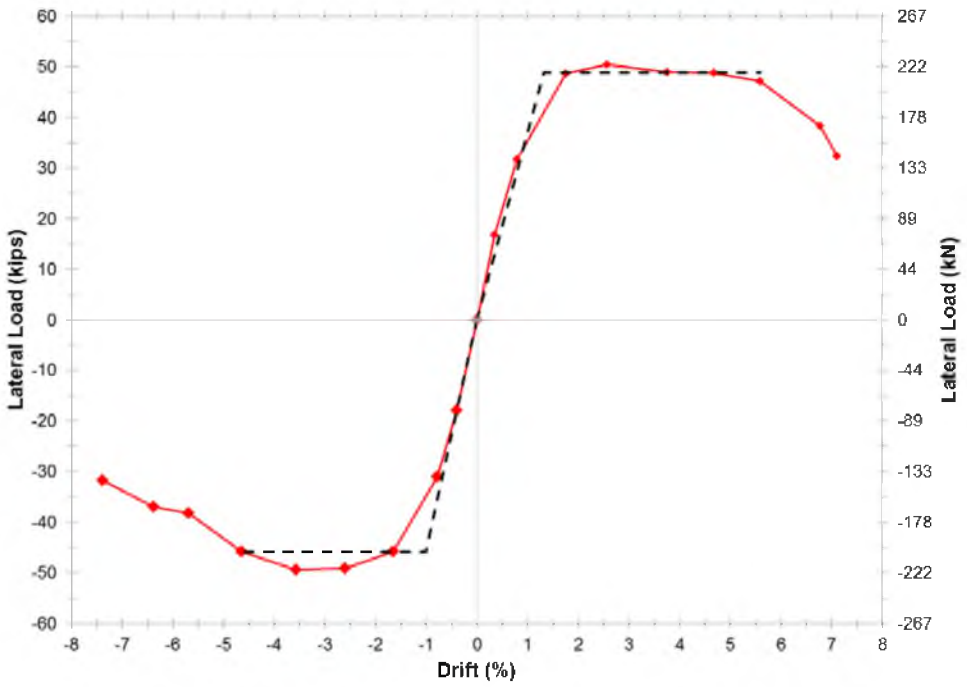

Figure 122. PCLEN-3R Backbone Curve

bridge columns between 4.0 and 5.0, PCLEN-3R still exhibited a satisfactory ductile performance.

The repair of PCLEN-3R was successful in re-establishing the lateral load capacity of the column and allowing the joint to fail in a ductile fashion. The repair did not move the plastic hinge entirely above the repaired region before failure of the CFRP jacket. However, the plastic hinge was relocated above the originally damaged section of the column even though it was not above the surface of the enlarged cross-section, as shown in Figure 123. There are certain reasons for this: the first is that Lenton splice sleeves in the column were shorter; as such the plastic hinge in PCLEN-3 is much shorter than when the sleeves were located in the pier cap as in PCLEN-2. With a shorter plastic hinge, damage does not spread up the column, meaning the repair could have been shorter thus reducing the required flexural demand in the repaired region. The second reason is that with a stronger concrete in the column than expected, and a column cross-section at the top of the repair with very minor damage, the required moment to move the plastic hinge above the repair was higher than expected, thus causing the failure to occur in the repair. Both of these reasons relate back to the original damage state of the column. Therefore, the importance

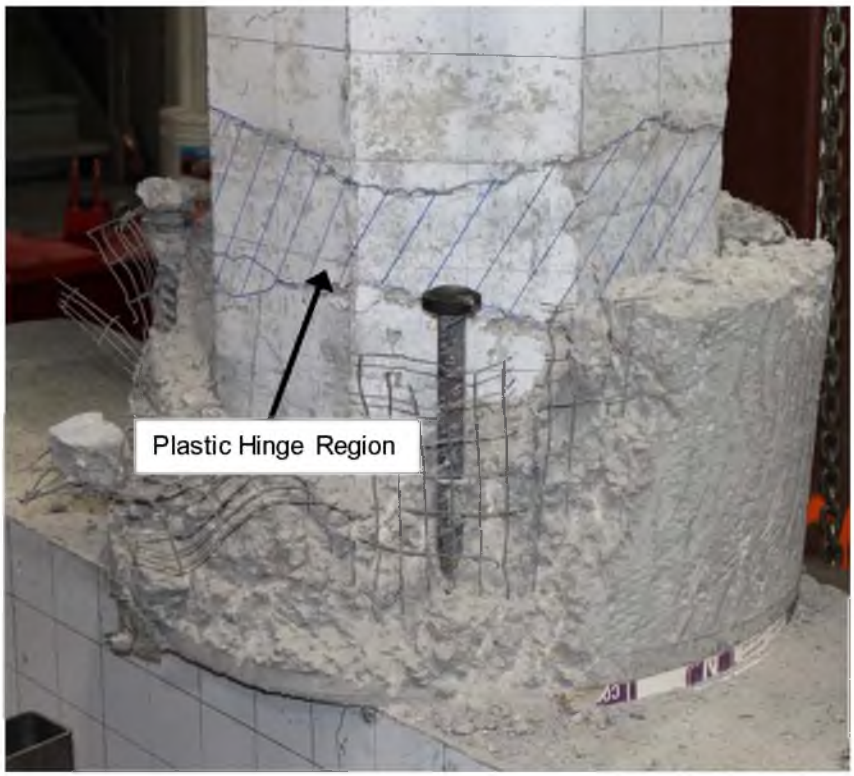

Figure 123. PCLEN-3R Plastic Hinge Relocation

of having a good assessment of the damaged column strength is paramount.

4.2 Repair of Precast Columns Summary

A repair technique was successfully developed that utilizes CFRP shells and plastic hinge relocation to repair damaged precast bridge column to pier cap grouted splice sleeve connections. Two original precast specimens were tested with the splice sleeves located either in the pier cap (PCLEN-2) or in the column (PCLEN-3).

The repair of PCLEN-2 utilized nonshrink concrete and successfully moved the plastic hinge above the repaired region. PCLEN-2R, however, was unintentionally pushed monotonically to a drift of 6.9 percent before performing a cyclic test and failed at a drift of 7 percent when a longitudinal bar fractured in the column just above the repair. STMs were developed for both PCLEN-2 and PCLEN-2R. The lateral load computed using the STM for PCLEN-2 was 97 percent of the lateral load from the test results. The lateral load computed using the STM for

PCLEN-2R was 92 percent of the lateral load from the monotonic pushover test. In both cases, the STMs give good estimates of the forces in the test specimens.

The repair of PCLEN-3 was successful in re-establishing the lateral load capacity of the column as well as achieving acceptable ductile behavior. The repair did not move the plastic hinge above the repaired region before fracture of the CFRP jacket. However, the plastic hinge was relocated above the originally damaged section of the column even though it was not completely above the surface of the enlarged cross-section. It is thought that if a more thorough damage assessment of the PCLEN-3 was performed, the design of the repair could have been modified enabling the relocation of the plastic hinge completely above the repaired region.

Overall, the repair technique was successful and even when the CFRP jacket fractured before relocating the plastic hinge entirely above the repair, a ductile performance was still observed. However, in both cases, the damage was moved above the damaged section of the plastic hinge of the column in the original specimens.

CHAPTER 5

CONCLUSIONS

The conclusions of this thesis are grouped in two sections, the repair and the AE monitoring assessment.

5.1 Repair

A repair procedure for postearthquake damage has been developed for severely damaged precast concrete bridge columns connected using grouted splice sleeves. The repair utilizes CFRP shells, headed bars, and plastic hinge relocation to repair the damaged column. Two precast specimens were repaired which had Lenton Interlock grouted splice sleeves located either in the pier cap (PCLEN-2R) or in the column (PCLEN-3R).

PCLEN-2R utilized nonshrink concrete and the plastic hinge was successfully moved above the repaired region. PCLEN-2R, however, was unintentionally pushed monotonically to a drift ratio of 6.9 percent before performing a cyclic test and failed at a drift ratio of 7 percent when a longitudinal bar fractured in the column just above the repair. Since this repair was initially damaged before performing the cyclic test, it was impractical to directly compare PCLEN-2R and PCLEN-2 in terms of displacement capacity, ductility, and energy dissipation. However, since PCLEN-2R reached the same displacement capacity as PCLEN-2 and increased the maximum lateral load in both the monotonic pushover and cyclic tests, it would be appropriate to conclude that PCLEN-2R performed similarly to PCLEN-2.

Strut and tie models were developed for PCLEN-2 and PCLEN-2R. Both models represent the test specimens at maximum lateral load where crushing of the concrete adjacent to the repair occurred. The lateral load computed using the STM for PCLEN-2 was 97 percent of

the lateral load from the test results. The lateral load computed using the STM for PCLEN-2R was 92 percent of the lateral load from the monotonic pushover test. In all cases, the STMs give good estimates of the forces in the test specimens making the models acceptable for design purposes

PCLEN-3R utilized expansive concrete to pretension the CFRP jacket and was successful in re-establishing the lateral load capacity of the column. The repair, however, did not move the plastic hinge above the repaired region before fracture of the CFRP jacket. It is thought that if a more thorough damage assessment of the PCLEN-3 were performed, the design of the repair could have been modified, enabling the relocation of the plastic hinge above the repaired region. However, the plastic hinge was relocated above the originally damaged section of the column even though it was not completely above the surface of the enlarged cross-section. Although the CFRP jacket fractured before moving the plastic hinge above the repaired region, the repaired column still had a displacement ductility greater than 4.0 and therefore still exhibited a ductile performance. Overall, the repair technique was successful by restoring the lateral load capacity of the column while still being ductile even when the CFRP jacket fractured.

For a repair design to have a desirable failure mode of relocating the plastic hinge above the repair a careful examination of the damaged column must be performed. From this examination, an accurate estimate of the column's concrete strength and ultimate moment capacity needs to be obtained in order to design the repair appropriately in terms of both length of the CFRP jacket along with the column, number of CFRP layers required, and the compressive strength of the nonshrink or expansive concrete between the original column surface and the CFRP Shell.

5.2 Acoustic Emission Monitoring

An AE monitoring assessment was performed on two different grouted splice sleeve systems when tested in tension to failure. Both splice sleeve types exhibited characteristics which relate to the damage state of the grouted splice sleeve. The AE data for the NMB splice sleeves revealed that as the load plateaued near the maximum load, the rate at which the AE events occurred decreased drastically. This decrease in the rate of AE events could be used to

identify that failure of the bar is imminent. The AE data for the Lenton Interlock splice sleeves revealed that as the bar began to pull out, the rate at which the AE events occurred increased drastically. This increase in the rate of AE events could be used to identify that failure of the sleeve has occurred and the bar is being pulled out.

The AE sensors located on the column concrete surface provided good information for the column to pier cap joint cyclic tests. FCNMB-1 and PCLEN-1, the AE event history and cumulative AE energy showed that the majority of the damage to the column cross-section came early on in the test. The reason damage did not accumulate in the column at the end of the tests is because the damage was localized at the column to footing or pier cap interface. Once damage became localized at the column footing or pier cap interface, damage no longer accumulated in the column; instead, the damage was forced just below the column to the field dowel.

The normalized cumulative AE energy was compared to the normalized hysteretic strain energy for both specimens. Previous research has shown that there is a strong correlation between these two in monolithic beam column joints. In the cases where the grouted splice sleeves were located in the column (FCNMB-1 and PCLEN-1), there was not a strong correlation. This is mainly due to the fact that the column was not the critical section allowing plastic deformations to form and spread. Instead, the damage was localized between the column and footing or pier cap.

From an AE monitoring assessment of PCLEN-2R, the location and time during the test of a transverse crack in the CFRP jacket was determined. This transverse CFRP crack went unnoticed during the test; therefore, without the AE monitoring system, it would not have been found. From the AE history, it is difficult to assess how much damage is being done to the CFRP jacket with each push, but it does give a good indication of the presence and accumulation of the damage.

5.3 Future Considerations

For both repaired specimens, transverse cracking of the CFRP jacket occurred. In PCLEN3-R, measures such as increasing the length of the headed bars in the repair region and

using expansive cement concrete were used in an attempt to negate this crack. These attempts were unsuccessful since the displacement demand at the top of the repair was still larger than the capacity. For future work, the capacity of the CFRP jacket in bending could be increased by incorporating fibers oriented in the vertical direction. Including fibers oriented in the vertical direction would increase the importance of the bond between the concrete and the CFRP jacket, which would be difficult to achieve due to the prefabricated CFRP shells. A combination of prefabrication of CFRP jackets and wet layup of CFRP jackets might be beneficial. Alternatively, a bidirectional CFRP shell could be used where fibers are oriented in the vertical and circumferential direction of the column axis.

For both PCLEN-1 and FCNMB-1, the AE sensors that were located on the splice sleeve failed to work during the tests. From the tension test, there were some strong correlations between AE data and when failure of the splice occurred. For future work, a method to embed the sensors on the splice sleeves could be explored in order to determine if the characteristics seen in the tension tests relate to the large-scale tests.

APPENDIX

A.1 Ceramic AE Sensors

The ceramic sensors used for the air tests and on the exterior of the concrete were Digital Wave B-1025 sensors. These sensors are 0.25 in. in diameter and 0.25 in. tall and are considered a very versatile sensor (*26*). The frequency bandwidth for this sensor is 1 kHz to 1.5 MHz. With this type of sensor, a couplant is needed in order to transmit the mechanical wave in the material to the sensor. For these tests, a high viscosity couplant called High Z was used and is manufactured by Sonotech. This couplant has an operating temperature range of -18°C to 93°C and has the ability to reduce surface noise on curved, rough, pitted, or heavily corroded surface including concrete.

A.2 Film AE Sensors

The film sensors that were embedded on the concrete and located on the grouted splice sleeves were Measurement Specialties SDT film sensors, shown in Figure 124. The film element has a length of 1.18 in., a width of 0.51 in., and a thickness of 0.005 in. which makes it a low profile sensor. This sensor has low cost and can be applied to the material surface using double sided adhesives, epoxy, or super glue and does not require a couplant. This sensor has a frequency bandwidth of 1 Hz to 60 kHz and operates under temperatures ranging from 0°C to 70°C.

A.3 AE Monitoring System Components and Settings

The AE system used to monitor the tests was provided by ATK and developed by Digital Wave Corporation. This system consisted of a portable computer, signal conditioning board, pre-amplifiers, AE sensors, and coaxial cables. When an AE event occurs, an elastic wave is initiated

Figure 124. Measurement Specialties SDT Film Sensor

and is picked up by the sensor where the sensor converts the mechanical wave into a digital signal. That signal is then amplified by preamplifiers, in this case PA-20's, before the signal reaches the signal conditioning board (FM). The FM conditions the signal by filtering out unwanted frequencies, setting trigger levels to increase or decrease sensor sensitivity to events, and then amplifying the signal before sending it to the computer (*26*). Digital Wave Explorer software is then used to analyze and display the signals. A schematic of the AE system as well as a photo of the AE system computer and signal conditioning board is shown in Figures 125 and 126, respectively.

The FM is used to condition the signal from the AE sensor and there are settings that can be changed on the box to fine tune the signal. The filtering and amplification capabilities of the FM are given in Table 24 (*26*). A list of the FM settings for the splice sleeve tension tests, the AE monitoring assessment of precast RC bridge columns, and the repair of PCLEN-2 are shown below.

FM Settings for the splice sleeve tension tests:

- Pre Amplifier Gain = 1 x6 dB
- Signal Gain Switch = 0 dB
- Signal HP Filter = 20 kHz

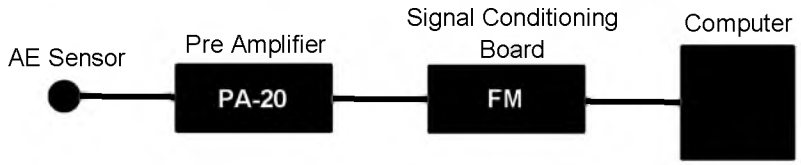

Figure 125. AE System Schematic

Figure 126. AE System Computer and Signal Conditioning Board

Table 24. FM Filtering and Amplification Capabilities

Parameter	Gain (dB)	High Pass Filter (kHz)	Low Pass Filter (kHz)
Preamplifier	0-42 (6 dB Increments)	---	---
Acquisition Signal Conditioning	0, 12, 24	20, 50, 100	---
Trigger Signal Conditioning	0-42 (6 dB Increments)	50, 100, 300	750, 1500, 5000

- Trigger Gain = 1 x3 dB
- Trigger Gain Switch = 0 dB
- Trigger High Pass Filter = 50 kHz
- Trigger Low Pass Filter = 0.75 MHz

FM Settings for the AE monitoring assessment of precast RC bridge columns:

- Pre Amplifier Gain = 1 x6 dB
- Signal Gain Switch = 12 dB
- Signal HP Filter = 20 kHz
- Trigger Gain = 2 x3 dB
- Trigger Gain Switch = 0 dB
- Trigger High Pass Filter = 50 kHz
- Trigger Low Pass Filter = 0.75 MHz

FM Settings for the repair of PCLEN-2:

- Pre Amplifier Gain = 1 x6 dB
- Signal Gain Switch = 24 dB
- Signal HP Filter = 20 kHz
- Trigger Gain = 2 x3 dB
- Trigger Gain Switch = 0 dB
- Trigger High Pass Filter = 50 kHz
- Trigger Low Pass Filter = 5 MHz

REFERENCES

(*1*) Seible, F.; Priestley, M.J.; Hegemier, G. Seismic Retrofit of RC Columns with Continuous Carbon Fiber Jackets*. J. Compos. Constr*. **1997**, 1, 52-62.

(*2*) Chai, Y.; Priestley, M.J.; Seible, F. Seismic Retrofit of Circular Bridge Columns for Enhanced Flexural Performance. *ACI Structural Journal*. **1991**,88, 572-584.

(*3*) Lehman, D.; Gookin, S.; Nacamuli, A.; Moehle, J. Repair of Earthquake-Damaged Bridge Columns*. ACI Structural Journal*. **2001**, 98, 233-242.

(*4*) Rutledge, S.; Kowalsky, M.;Seracino, R.; Nau, N. *Repair of Damaged Circular Reinforced Concrete Columns by Plastic Hinge Relocation*, Proceedings of the 15 WCEE, Lisbo, 2012.

(*5*) Haber, Z.; Saiidi, M.; Sanders, D. *Precast Column-Footing Connections for Accelerated Bridge Construction in Seismic Zones*; Final Report No. CA13-2290;Nevada, 2013.

(6) Ameli, M.J. Seismic Design of Grouted Splice Sleeve Connections for Bridge Piers used in Accelerated Bridge Construction. Ph.D. Dissertation, University of Utah, SLC, UT, to be submitted for publication.

(*7*) Nair, A.; Cai, C.S. Acoustic Emission Monitoring of Bridges: Review and Case Studies. *Engineering structures*, **2010**, 32, 1704-1714.

(*8*) Sandberg, J.; Hendy, C*. Replacement of the Stays on Major Cable-Stayed Bridge*, Proceeding of the institution of Civil Engineers, 2010.

(*9*) Hose, Y.D; Seible, F; Priestley, M.J. Strategic relocation of plastic hinges in Bridge columns, SSPR 97-05.

(*10*) Joh, O.; Goto, Y.; Shibata, T. *Influence of* Transverse Joint and Beam Reinforcement and Relocation of Plastic hinge region on Beam Column Joint Stiffness Deterioration; SP 123-8, 187-223

(*11*) Hong, S.G.; Chun, S.C.; Lee, S.H.; Oh, B. Strut and Tie Model for Development of Headed Bars in Exterior Beam Column Joint. *ACI Structural Journal*, **2007**, 590-600.

(*12*) Lehman, D.E.; Gookin, S.E.; Nacamuli, A.M.; Moehle, J.P. Repair of Earthquake-Damaged Bridge Columns. *ACI Structural Journal,* **2001**, 233-242.

(*13*) Xiao, Y.; Priestley, M.J.; Seible, F. Seismic Assessment and Retrofit of Bridge Column Footing. *ACI Structural Journal,* **1996**, 79-94.

(*14*) Mirmiran, A.; Philip, S. Comparison of Acoustic Emission Activity in Steel-Reeinforced and FRP-Reinforced Concrete Beams. *Construction and Building Materials,* **2000**, 14, 299-310.

(*15*) Mirmiran, A.; Shahawy, M.; Echary, H. Acoustic Emission Monitoring of Hybrid FRP-Concrete Columns. J.Eng. Mech. **1999**, 125, 899-905

(*16*) Benavent-Climent, A.; Castro, E.; Gallego, A. AE Monitoring for Damage Assessment of RC Exterior Beam-Column Subasssembleges Subjected to Cyclic Loading. *Structural Health Monitoring*, **2009**, 8, 175- 189.

(17) ASTM Standard A370, 2012, " Methods for Testing Steel Reinforcing Bars," ASTM International, West Conshocken, PA, 2012, DOI 10.1520/C0109_C0109M, www.astm.org.

(18) ASTM Standard A109, 2012, "Standard Test Method for Compressive Strength of Hydraulic Cement Mortars (Using 2-in. Cube Specimens," ASTM International, West Conshocken, PA, 2012, DOI 10.1520/A0307-12, www.astm.org.

(19) American Association of State Highway and Transportation Officials (AASHTO). AASHTO LRFD Bridge Design Specifications. AASHTO: Washington, D. C. 2012.

(20) American Association of State Highway and Transportation Officials (AASHTO). AASHTO Guide Specifications for LRFD Seismic Bridge Design. AASHTO: Washington, D. C. 2011.

(21) American Concrete Institute. ACI 318-11 Building Code Requirements for Structural Concrete; Farmington Hills, MI, 2011.

(22) American Concrete Institute. ACI 550.1R-09 Guide to Emulating Cast-in-Place Detailing for Seismic Design of Precast Concrete Structures; Farmington Hills, MI, 2009.

(23) American Concrete Institute. ACI 374.2-13 Guide for Testing Reinforced Concrete Structural Elements under Slowly Applied Simulated Seismic Loads; Farmington Hills, MI, 2013.

(24) ASTM Standard C39, 2012, "Standard Test Method for Compressive Strength of Cylindrical Concrete Specimens," ASTM International, West Conshocken, PA, 2012, DOI 10.1520/C0039_C0039M-12A, www.astm.org

(25) Moran, D.; Pantelides, C. Elliptical and circular FRP-Confined concrete sections: A Mohr-Coulomb analytical model. Int. J. Solids and Struct, 2012, 49, 881-898.

(26) Papulak, T.S. An Inverse Acoustical Phase Array Technique for Impact Detection and Location. Masters Thesis, University of Utah, Salt Lake City, Utah, 2012